TECHNISCHE UNIVERSITÄT WIEN

D I P L O M A R B E I T

Reconstruction of Attractors as new Method for Quantification of Arterial Pulse Wave Morphology

ausgeführt am

Institut für

Analysis und Scientific Computing

TU Wien

unter der Anleitung von

Ao.Univ.Prof. Dipl.-Ing. Dr.techn. Felix Breitenecker

und

Univ.Lektor Dipl.-Ing. Dr.techn. Christopher Mayer

durch

Carina Hörandtner

Matrikelnummer: 01326701

Westbahnstraße 60/7

1070 Wien

Wien, 5. Februar 2021

Eidesstattliche Erklärung

Ich erkläre an Eides statt, dass ich die vorliegende Diplomarbeit selbstständig und ohne fremde Hilfe verfasst, andere als die angegebenen Quellen und Hilfsmittel nicht benutzt bzw. die wörtlich oder sinngemäß entnommenen Stellen als solche kenntlich gemacht habe.

Wien, 5. Februar 2021

_____
Carina Hörandtner

Abstract

Cardiovascular diseases (CVDs) are one of the leading causes of death worldwide. Therefore, early detection and prevention by means of non-invasive, quick and cost-effective methods are of crucial importance. One approach is to analyse non-invasively recorded pulse waveforms. Many methods focus only on averaged numerical values, such as heart rate or systolic and diastolic blood pressure (minimum and maximum of pressure wave) in a short time-frame, and neglect a majority of other data points, which, however, influence morphology and variability of a waveform. Thus, considering all data might provide a deeper understanding of physiological or pathological changes within the cardiovascular system.

Therefore, this thesis presents a new way to quantify arterial pulse wave morphology based on the reconstruction of attractors. To that end, an existing attractor reconstruction method using Takens' delay coordinates has been used and further developed. Attractor reconstruction enables an easy representation of pulse waveforms and, especially, their variability.

The first step of the procedure is to preprocess the pulse wave data and generate the attractor. Afterwards, a median filter edits the reconstructed attractor to remove remaining artefacts. In order to quantify the attractor, the author beforehand developed and implemented a feature extraction technique based on image processing and subsequently linked the extracted parameters to pulse waveform features.

Lastly, the thesis presents the application of the algorithm to pulse wave data acquired through photoplethysmography (PPG) at the fingertip of 30 patients with treated arterial hypertension. During the first 10 minutes, the subjects exercised device-guided breathing, followed by an unguided cooling phase of 5 minutes. The aim was to examine how the attractors or, respectively, the pulse wave morphology change over time.

Analyses of the evolution plots showed a significant decline in the average height of the attractors ($p = 0.001$) during the entire recording which can be linked to a decrease in pulse pressure. In addition, the ratio of the average width of the attractor arms to the average height of the attractors, as a measure of the waveforms' variability, showed a borderline significant increase ($p = 0.077$) during the cooling down phase. This suggested that the variability of the pulse waveform was higher during the unguided phase than during the guided breathing.

Visual examinations of 90 attractors evaluated the performance of the feature extraction technique. Although the developed method correctly quantified a majority of the generated attractors, it was discovered that remaining outliers or metrological discrepancies had a negative impact on the results. Additionally, the introduced approach did not work well on attractors with overlapping arms.

Apart from already established correlations, it was discovered that shape and orientation of the attractors mostly depend on the curvature of the pulse waves' downstroke and on the ratio of the crest time to the average heart rate. It can be assumed that the position of the dicrotic notch and the dicrotic wave amplitude influence the shape of the attractors. However, it needs further investigations to specify these correlations.

The results presented in this thesis are promising and encourage further studies on attractor reconstruction as a new way to quantify cardiovascular waveforms.

Kurzfassung

Kardiovaskuläre Erkrankungen sind einer der häufigsten Todesursachen weltweit. Früherkennung und Prävention mit Hilfe von nicht-invasiven, schnellen und kosteneffizienten Methoden sind daher von größter Bedeutung. Eine Vorgehensweise ist, nicht-invasiv aufgenommene Pulswellen zu analysieren. Sehr viele Methoden betrachten nur gemittelte Daten, wie z.B. die Herzrate oder den systolischen und diastolischen Blutdruck (Maximum bzw. Minimum der Druckwelle) in einem kurzen Zeitfenster. Dabei werden jedoch viele Werte, die für die Form der Pulswelle bzw. deren Veränderung eine wichtige Rolle spielen, nicht berücksichtigt. Miteinbeziehung dieser Datenpunkte könnte jedoch helfen, physiologische und pathologische Veränderungen innerhalb des kardiovaskulären Systems besser zu verstehen.

In dieser Arbeit wird eine neue Methode zur Quantifizierung der arteriellen Pulswellenmorphologie vorgestellt. Zu diesem Zweck, wurde die bereits bestehende Attraktorrekonstruktionsmethode, die sich Takens "delay coordinates" zunutze macht, verwendet und weiterentwickelt. Diese Technik erlaubt eine einfache Darstellung der Pulswellenform und vor allem deren Variabilität. Der erste Schritt des Prozesses beinhaltet die Vorverarbeitung der Pulswellendaten und die Generierung des Attraktors. Anschließend wird der Attraktor mittels Medianfilter bearbeitet, um verbleibende Artefakte zu beseitigen. Um nun die Attraktoren zu quantifizieren, entwickelte und implementierte die Autorin eine Technik zur Merkmalsgewinnung basierend auf einem Bildverarbeitungsverfahren und brachte die gewonnenen Parameter mit Eigenschaften der Pulswelle in Verbindung.

Zu guter Letzt stellt diese Arbeit die Anwendung des Algorithmus auf Pulswellendaten von 30 Patienten, die gegen arteriellen Bluthochdruck behandelt wurden, vor. Die Messungen wurden mittels Photoplethysmographie (PPG) an der Fingerspitze durchgeführt. Während der ersten 10 Minuten mussten die Probanden eine geleitete Atemübung durchführen, wohingegen sie in den letzten 5 Minuten der Aufnahme frei atmen durften. Ziel war es, zu untersuchen, wie sich die Attraktoren bzw. die Pulswellenmorphologie über die Zeit verändern.

Auswertungen zeigten eine signifikante Verkleinerung der durchschnittlichen Höhe der Attraktoren ($p = 0.001$) während der gesamten Aufzeichnung. Dies kann mit einer Abnahme des Pulsdrucks in Verbindung gebracht werden. Außerdem ließ sich ein grenzwertig signifikanter Anstieg ($p = 0.077$) des Verhältnisses zwischen durchschnittlicher Attraktorarmbreite zu durchschnittlicher Höhe der Attraktoren in den letzten 5 Minuten feststellen. Das lässt vermuten, dass die Variabilität der Pulswellen in der ungeleiteten Phase höher war als während der geleiteten Atemübung.

Um die Performance der entwickelten Methode zu beurteilen, wurden 90 Attraktoren visuell

untersucht. Obwohl die Mehrheit der Attraktoren korrekt quantifiziert wurde, konnte man dennoch feststellen, dass sich verbleibende Ausreißer bzw. messtechnische Probleme während der Aufnahme negativ auf die Resultate auswirkten. Außerdem lieferte die vorgestellte Methode bei Attraktoren mit sich überlappenden Armen wenig zufriedenstellende Ergebnisse.

Neben bereits bekannten Zusammenhängen konnte man feststellen, dass Form und Ausrichtung der Attraktoren hauptsächlich von der Krümmung des "Downstrokes" der Pulswelle und vom Verhältnis zwischen "crest time" und der durchschnittlichen Herzrate abhängig sind. Es kann angenommen werden, dass sich die Position der dikrotischen Erhebung sowie deren Amplitude auf die Form der Attraktoren auswirken. Allerdings bedarf es weiterer Untersuchung, um den genauen Zusammenhang zu ermitteln.

Die in dieser Arbeit vorgestellten Resultate sind durchaus vielversprechend und rechtfertigen weitere Untersuchungen im Bereich der Attraktorrekonstruktion zur Quantifizierung kardiovaskulärer Wellenformen.

Danksagung

Zunächst möchte ich mich bei Christopher Mayer vom AIT Austrian Institute of Technology für die hervorragende Betreuung dieser Diplomarbeit bedanken. Danke, dass du mich auf dieses Thema aufmerksam gemacht hast und du dir Zeit genommen hast, all meine Fragen ausführlich zu beantworten.

Außerdem gilt mein Dank Herrn Professor Felix Breitenecker und seiner Arbeitsgruppe. Die von ihnen organisierten Lehrveranstaltungen weckten mein Interesse an mathematischer Modellbildung und machten mich erst auf das AIT aufmerksam. Dadurch konnte ich erstmals in den Bereich der kardiovaskulären Forschung hineinschnuppern und somit mein medizinisches Interesse mit meiner Studienwahl verknüpfen.

Besonderer Dank gebührt auch meinen Kolleginnen und Kollegen vom AIT, insbesondere Martin Bachler. Ihre konstruktiven Denkanstöße haben maßgeblich zu dieser Arbeit beigetragen und mir geholfen, neue Ansätze zu finden und zu verwirklichen.

Meine Studienkolleginnen und Studienkollegen haben mir in den letzten Jahren gezeigt, was man als Team alles schaffen kann. Vielen Dank für eure Unterstützung und die lustige Zeit sowohl auf der Uni als auch bei diversen außeruniversitären Veranstaltungen.

Mein allergrößter Dank gilt aber meiner Familie, im Speziellen meinen Eltern Martha und Norbert. Vielen Dank, dass ihr mich nicht nur finanziell unterstützt habt, sondern mich auch stets in meinen Entscheidungen bestärkt und mir den nötigen Rückhalt geboten habt. Ich kann mich immer auf euch verlassen und dafür bin ich euch zutiefst dankbar.

Contents

1. Introduction

1.1. Motivation

According to the "European Society of Cardiology", cardiovascular diseases (CVDs) were the most common cause of death across Europe in 2019, accounting for 2.2 million deaths in females (47% of all deaths) and 1.9 million deaths in males (39% of all deaths) [42]. Early detection of crucial risk factors can help to prevent CVDs. Thus, several methods to gather information captured within cardiovascular waveforms have been developed and investigated for many decades [5]. Over the years, it became easy to collect large quantities of data rather quickly and the main task was to derive useful information from it. Currently, pulse waveform analysis provides only averaged numerical values, such as heart rate or systolic and diastolic blood pressure (central or peripheral). These methods consider only a few data points and ignore changes of the pulse waveform morphology over time, which nevertheless might provide valuable insight into the cardiovascular system as well. Therefore, new ways to quantify pulse wave morphology are needed.

One of the most important risk factors for CVDs is high blood pressure [15]. Studies have shown that beyond medications and diets, relaxation techniques, like breathing exercises, prove to be beneficial to lower blood pressure [7]. Hence, a topic of interest would be the impact of breathing techniques on pulse waveform features in general and how the morphology of pulse waves changes over time.

1.2. Aim of the Thesis

The aim of this thesis is to develop and implement an algorithm for the automatic quantification of arterial pulse wave morphology in MATLAB®. For this purpose, an existing method of reconstructing attractors from pulse waveform data is used and further developed. In the process, the attractors are quantified, attractor features extracted and linked to pulse waveform features. Afterwards, the algorithm is applied to pulse wave signals from 30 subjects suffering from hypertension. The goal is to examine how 10 minutes of device-guided breathing followed by 5 minutes of unguided breathing affect the size and shape of the attractors. To that end, the means of the extracted features across all subjects are calculated and plotted as functions over time.

1

1.3. Thesis Outline

The thesis consists of 7 chapters. The first one states motivation and aim of the thesis. Chapter 2 starts with a description of the physiological background of the cardiovascular system and summarizes current methods of pulse waveform analysis together with possible downsides. Afterwards, the new attractor reconstruction method is presented. The chapter concludes with an overview of already established correlations between attractor features and pulse waveform features. In chapter 3, the used data is specified and the used statistical methods are presented. Methodology and implementation are described in chapter 4 starting with preprocessing of the data sets. Thereafter, the implementation of the attractor reconstruction method and a filtering procedure are presented, followed by a thorough description of the feature extraction technique. Chapter 5 provides an evaluation of the developed algorithm and summarizes the results of the feature extraction method applied to the given data sets. Chapter 6 focuses on the interpretation of the extracted attractor features and discusses the results of the breathing exercise provided in the previous chapter. The thesis concludes with an outlook on possible further improvements.

2. Background

In the fist section of this chapter, a short overview of the physiology of the heart, its impact on the circulatory system and basic knowledge on arterial blood pressure is provided. So far, various methods to analyse and quantify pulse waves have been established; however, they sometimes do not function smoothly. Attractor reconstruction is a new approach to quantify pulse waveform data and serves as a way to overcome these issues. The chapter is closed by a comparison of attractor features with pulse waveform features.

2.1. Physiological Background

The following section is based on the textbooks of Guyton and Hall [16] and Pape, Kurtz and Silbernagel [32], if not further specified.

2.1.1. Anatomy and Physiology of the Heart

The heart plays a key role in the circulatory system by pumping blood through the body and thus providing tissues and organs with oxygen and nutrients. It consists of two separate pumps: on the one hand, the right heart pumps blood through the lungs and on the other hand, the left heart pumps blood through the peripheral organs. Each of these two halves is again divided into two chambers: the atrium, which is a weak primer pump, and the ventricle, which supplies the main pumping force. The right ventricle accelerate the blood through the pulmonary circulation and the left ventricle propels it into the peripheral circulation. The atrioventricular valves (tricuspid and mitral valve) prevent backflow from the ventricles into the atria and the semilunar valves (aortic and pulmonary artery valves) prevent backflow from the aorta and pulmonary arteries into the ventricles. Furthermore, the pressure gradients in the heart control the opening and closing of the valves. Figure 2.1 illustrates the structure of the heart and the course of blood flow through the cardiovascular system.

The cardiac cycle represents the complete sequence of events in the heart that occur between two consecutive heartbeats. In general, the heart cycle is divided into a period of relaxation called *diastole*, where the heart is filled with blood, followed by a period of contraction called *systole*.
Like any other muscle contraction in the body, the contraction of the heart is induced by electrical impulses. The sinosatrial (SA) node is the primary pacemaker of the heart and is

located in the right atrium, usually causing about 60-80 rhythmical contractions per minute. Its fibres contain almost no contractile muscle filaments but connect directly with the atrial muscle fibres, which leads to an immediate spreading of action potentials. Each impulse travels from the SA node to the atrioventricular (AV) node, where the impulse from the atria is delayed before it is passed through the AV bundle to the ventricles. The left and right bundle branches of Purkinje fibers conduct the cardiac impulse to all parts of the ventricles.

The AV valves open when the atrial pressure exceeds the ventricular pressure, which allows blood to flow rapidly into the ventricles. The action potential initiated in the SA node stimulates both atria to contract and the ventricles fill with more blood. During this time, the semilunar valves are closed. Systole starts with the closure of the AV valves. The contraction of the ventricles leads to an increase in ventricular pressure and when this pressure exceeds the pressure of the aorta, the semilunar valves open. As a consequence, blood is pressed from the heart into the arteries. When the ventricles begin to relax, the semilunar valves close, the ventricular pressure decreases and diastole begins.
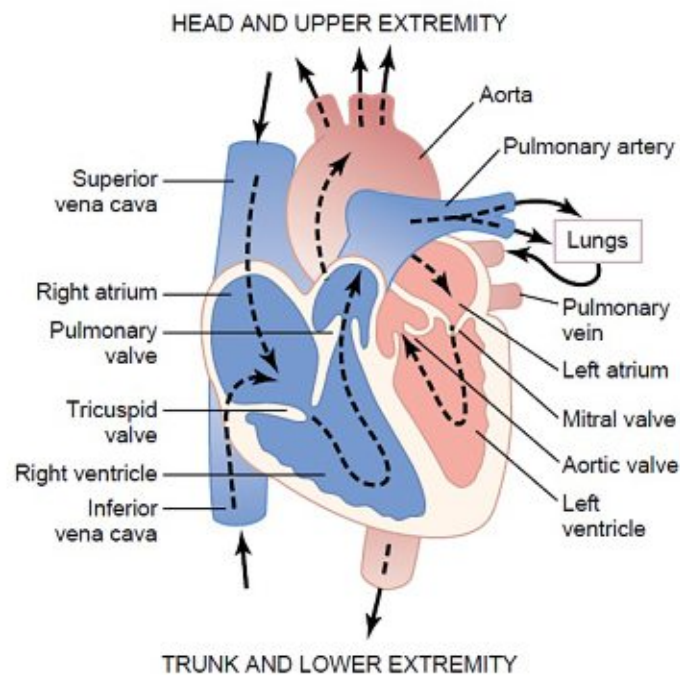

Figure 2.1.: Structure of the heart, and course of blood flow through the heart chambers and heart valves. Adapted from [16].

2.1.2. The Circulatory System

The main function of the circulatory system is to serve the needs of the somatic cells by transporting nutrients and oxygen to the tissues and organs, transporting waste products away and by conducting hormones from one part of the body to another. The circulatory system itself is divided into the systemic circulation and the pulmonary circulation. Oxygenated blood is

4

ejected into the systematic circulation by the left ventricle. The first part of the arterial system is the aorta, an artery with a thick and elastic wall. Thereafter, the blood flows under high pressure through the arteries into the arterioles, which control the release of blood into the capillaries. At the capillaries, oxygen and nutrients diffuse into the surrounding tissues. The venules collect the blood from the capillaries and gradually merge into larger veins, which transport the blood back to the heart. The deoxygenated blood flows through the right atrium into the right ventricle, where it is pumped into the pulmonary circulation and, consequently, into the lungs. After oxygenation, the blood travels back to the left atrium and ventricle and the circle recommences.

When a person is at rest, 4 to 6 litres of blood are transported through the body each minute. During exercise, the heart can pump up to 7 times this amount.

2.1.3. Arterial Blood Pressure

The heart pumps blood into the arteries against the total peripheral resistance into the arteries. The narrower the arteries, the higher the force that is needed to keep the blood flowing. Blood pressure is defined as the amount of force exerted by the blood against the vessel walls and is measured in millimetres of mercury (mmHg) [20]. When the heart contracts, blood is released into the aorta in form of a pulse wave. This entry of blood causes the vessel walls to stretch and increases the pressure. Among healthy young adults, the pressure at the peak of each pulse wave, called the *systolic pressure*, is about 120 mmHg. As the aortic valve closes, a so-called *incisura* or *dicrotic notch* occurs. This is caused by a short period of backward flow of blood into the heart just before closure of the valve. As the heart relaxes, the pressure in the aorta drops to its lowest value, called the *diastolic pressure*, which is about 80 mmHg among healthy individuals. The difference between the systolic and diastolic pressure is called the *pulse pressure*, which is affected by two main factors: the stroke volume, i.e., the output of the heart, and the compliance of the arterial tress. The higher the stroke volume, the higher the amount of blood that is pumped into the arterial tree. As a consequence, the increase and reduction in pressure are more distinct during systole and diastole phases which thus causes a higher pulse pressure. On the contrary, the less the compliance of the arterial tree, the greater the increase in pressure for a given stroke volume of blood ejected into the vessels.

As the blood travels through the arteries towards the periphery, blood pressure as well as the pulse wave's shape change (figure 2.2). Pulse waves recorded at the root of the aorta display a sharp cut in the waveform followed by a small pressure increase. The trough between two pressure peaks, the incisura or dicrotic notch, relates to the closure of the aortic valve (as described before). The peripheral arterial pressure waveform might have a later, smoother dicrotic notch that rather reflects peripheral vascular resistance and arises due to reflected pressure waves [26].
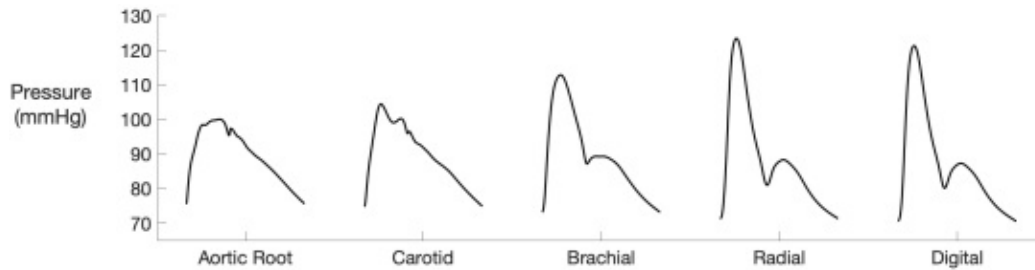
Figure 2.2.: Pulse waves at different anatomical sites. Adapted from [33].

The medical term for high blood pressure is *Hypertension* and is defined as a systolic blood pressure of greater than 140 mmHg and/or a diastolic blood pressure of greater than 90 mmHg [20].

2.2. Current Pulse Waveform Analysis

The measurement and quantification of the pulse dates back to 500 BC, when Chinese started to measure pulse at wrist by finger and began to use it as a diagnostic tool during examination. In 400 BC, the Greeks started to notice its rhythm, strength, and velocity. Arterial pulse waveform analysis developed further in the mid-19th century, when Etienne-Jules Marey invented a level based sphygmograph to measure the pulse rate. Shortly after that, Frederick Mohamed observed normal radial pressure waves and carotid waves to find the differences and figured out, how high blood pressure affects those waveforms. [12]

Up until now, there have been established various methods to quantify pulse waves. In the following, several techniques are mentioned with no claim to completeness.

One prominent way is to extract specific points of the curve and average those values in the considered time window. The maximum arterial pressure during systole, characterized as the first local peak of a pulse wave, is denoted as the *systolic pressure*. Together with the *diastolic pressure*, defined as the lowest arterial pressure value, and the resulting *pulse pressure*, the systolic pressure provides insights into the cardiovascular system, as illustrated in [21, 30].

Another distinctive point of the pulse wave is the *dicrotic notch* already mentioned in 2.1.3, followed by the *dicrotic wave*. The *dicrotic wave pressure* is defined as the second prominent peak of the arterial pulse wave. The position of the dicrotic notch can be seen as an indicator of vasomotor tone. The descent of the dicrotic notch towards the diastolic pressure baseline is a sign of vasodilatation, which can, for example, be induced by anesthetics but might also be an indicator of severe sepsis [27, 28].

Another valuable measure is the *augmentation index* which aims to quantify the impact of pulse wave reflections on the pressure waveform [44]. In the past, the augmentation index was considered as a direct marker of arterial stiffness; more recently, however, it has been used as an index of arterial wave reflection which can indirectly be linked to arterial stiffness [40] and

increases with age. In the case of stiff arteries, the pulse wave velocity (PWV) rises which shifts the reflected wave towards the systolic pressure that leads to an augmentation of pressure. The inflection point marks the beginning of the reflected wave and can overlap with the systolic pressure (figure 2.3). The pressure difference between the inflection point and the peak systolic pressure is called *augmentation pressure*. The augmentation and pulse pressure's ratio yields then the augmentation index [31, 43, 45].
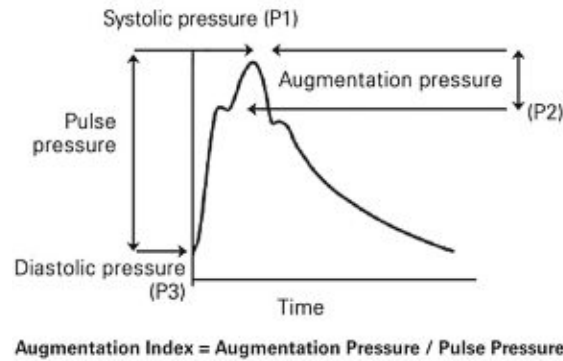

Figure 2.3.: Augmentation index is defined as the ratio of the augmentation pressure and pulse pressure. Adapted from [43].

Additionally, the pulse waveform can also be described by certain time intervals like the *peak to peak interval* which measures the distance between two consecutive systolic peaks and correlates closely with the R-R interval in ECG signals as both represent a completed heart cycle [25]. Another considered time interval is the *crest time* which is defined as the time frame between the pulse wave's nadir and the systolic pressure. It was noticed that a low crest time, which correlates with a steep rise of the pulse wave, is a sign of stiffer arterial walls and proved to be a useful feature to classify cardiovascular diseases [1, 4]. The time between the systolic and diastolic peaks ΔT, or, in the absence of a dicrotic wave, the point of inflection, is related to the time taken for the pressure wave to travel from the heart to the periphery and back; therefore, it is related to the PWV [4, 25]. This path length can be assumed to be proportional to subject height (h). Millasseau et al. [24] formulated a *stiffness index*

$$SI = \frac{h}{\Delta T}$$

that indicates the stiffness of an artery. As arterial stiffness grows with age, the pulse wave velocity increases and the time delay between the systolic and diastolic peaks decreases (figure 2.4). Therefore, the *SI index* increases with age [25].

Another way to quantify the pulse waveform morphology is to analyse the first and second derivative of the signal. The first derivative is a useful tool to directly detect peaks [4, 24, 25]. The second derivative is more commonly applied in research and its specific waveform is used to derive several ratios which provide further information on the considered pressure wave, as stated in [18, 25, 37, 38].
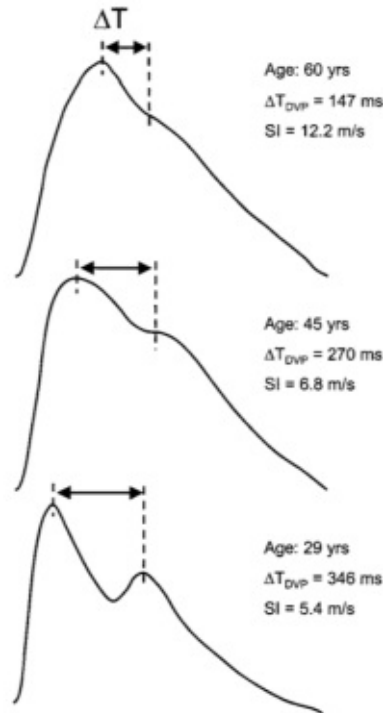
Figure 2.4.: Typical PPG waveforms, showing the characteristics change with age. Adapted from [24].

Although many approaches of current pulse waveform analysis have proven to be useful tools to detect cardiovascular diseases, some weak spots are worth mentioning and will be addressed in the next section.

2.3. Downsides of current Pulse Waveform Analysis

The following issues are presented in Nandi et al. [29] and summarized in the following shortly.

The first issue that has to be mentioned is the fact that current pulse waveform analysis methods do not use all available data. The higher the sampling rate, the more data are generated. A sampling rate of 125 Hz, for example, means that every second 125 data points are collected. Monitoring a patient over a period of 10 seconds leads to a a data set of 1250 points already. A data set this big would be in need of meaningful inspection and interpretation by doctors and nurses. Due to this almost impossible and time-consuming task, only average values like the average maximum peak values of the waves (systolic pressure) or the average height of the waves (pulse pressure) are examined. However, these measurements consider only a small number of data points and ignore thus those providing useful information on the pulse wave's shape. Additionally, pulse waveform data is usually plotted against a time axis and viewed over a long period of time. By doing so, it is difficult to detect any changes in shape and variability of the pulse wave (figure 2.5). Consequently, the waveform shape can only be quantified appropriately

if a short time window is selected which again just focuses on a small number of sampled data. The third issue addressed in [29] is baseline wander and noise. Baseline wander can occur in pulse waves due to respiration and movement during the recording. As this can interfere with the signal and may affect valuable measurements like the systolic, diastolic and or pulse pressure, baseline wander is removed in some studies [13]. However, editing the original signal in this way may exclude important information from the data. Noise, on the other hand, can have a negative impact on shape and variability of the pulse waveform and can therefore interfere with appropriate quantification.

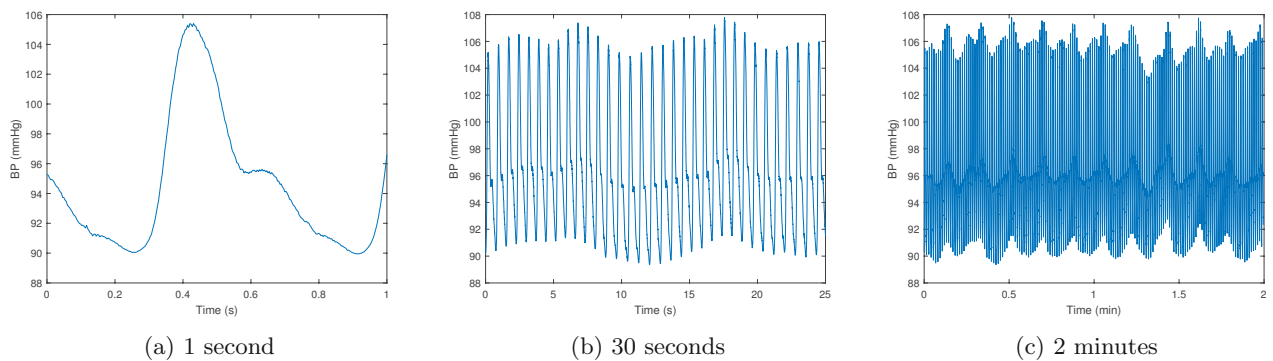|		
(a) 1 second	(b) 30 seconds	(c) 2 minutes

Figure 2.5.: Arterial pulse waveform data stream obtained by a non-invasive finger tip monitor. The detailed morphology of the waveform is not visible when viewed over longer periods of time.

2.4. Attractor Reconstruction Method

To overcome the issues mentioned in 2.3, Aston et al. [5] and Nandi et al. [29] developed a new way to visualize and quantify cardiovascular waveform data. This method generates attractors using Takens' [39] delay coordinates and combines mathematical knowledge with the expertise on cardiovascular physiology. To understand the advantages of attractor reconstruction, a short overview of the main steps is provided.

2.4.1. Attractor reconstruction using delay coordinates

The first step is to visualize the pulse waveform data in a given time window in a meaningful way. As mentioned before, it can be very difficult to see any structure in the signal when it is plotted over a long period of time. One way to overcome this problem is to plot the trajectory in the phase space as the attractor is then contained in a bounded region. However, it seems as if a single signal does not provide enough information to plot the trajectory. In 1981, Takens [39] showed that the issue of deriving information regarding a dynamical system from a single observed variable can be solved by using a vector of delay coordinates. This implies that an attractor can be reconstructed in a n-dimensional phase space from a single signal $x(t)$ by using

the following vector:

$$[x(t), x(t-\tau), x(t-2\tau), \ldots, x(t-(n-1)\tau)],$$

where $\tau > 0$ is a fixed delay and $n \geq 2$ is the embedding dimension [5]. The optimal time delay τ is chosen to be one third of the average cycle length in a given time window, whereby the detailed proof can be found in [5]. In order to visualize and detect dynamic changes in the attractor properly, the dimension is chosen to be $n = 3$. The resulting variables are the given signals $x(t)$, $y(t)$ and $z(t)$, respectively, defined by

$$y(t) = x(t-\tau), \quad z(t) = x(t-2\tau).$$

The data can then be plotted in the three dimensional phase space as $(x(t), y(t), z(t))$ for all t in the given time window, resulting in numerous overlapping loops, the so-called attractor (figure 2.6).
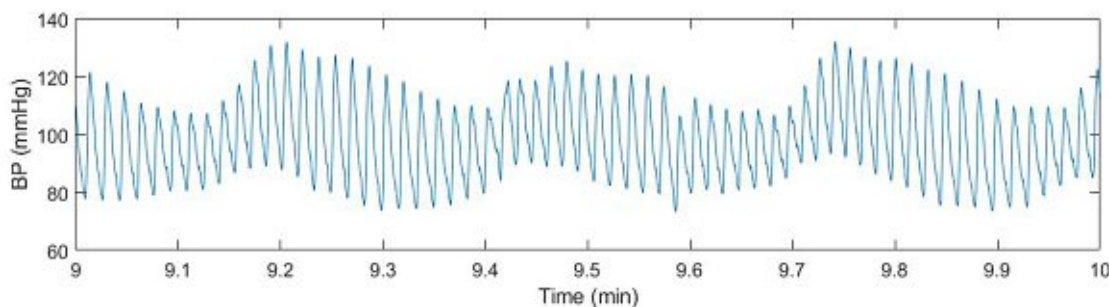
(a)
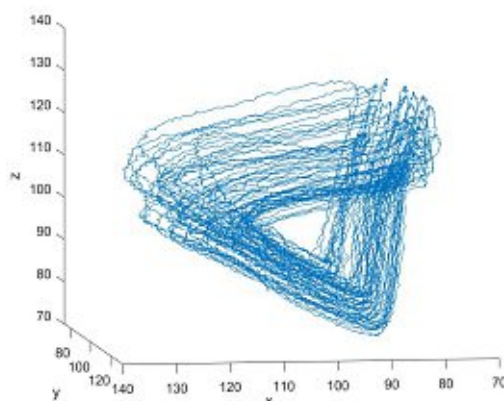
(b)

Figure 2.6.: Attractor reconstruction using delay coordinates: (a) 60 second sample of pulse waveform data, (b) a trajectory in the three-dimensional reconstructed phase space.

2.4.2. Removal of baseline wander

The new variables $y(t)$ and $z(t)$ are derived directly from the recorded signal $x(t)$. Hence, a vertical shift in the signal $x(t)$ by a constant amount $c \in \mathbb{R}$, i.e. $x(t) \rightarrow x(t) + c$, implies $y(t) \rightarrow y(t) + c$ and $z(t) \rightarrow z(t) + c$ as well. In the three dimensional phase space the shift in the signal $x(t)$ leads to $(x(t), y(t), z(t)) \rightarrow (x(t) + c, y(t) + c, z(t) + c) = (x(t), y(t), z(t)) + c(1, 1, 1)$ which corresponds to a shift in the direction of the vector $(1,1,1)$. Thus, in order to remove the effect of vertical translations, the attractor is plotted onto a plane orthogonal to the vector $(1, 1, 1)$, as seen in figure 2.8a. Therefore, the resulting new set of coordinates (u, v, w) is defined as

$$u = \frac{1}{3}(x + y + z), \quad v = \frac{1}{\sqrt{6}}(x + y - 2z), \quad w = \frac{1}{\sqrt{2}}(x - y). \tag{2.1}$$

It can be shown that a vertical variation of the signal $x(t)$ has an impact on the variable $u(t) \rightarrow u(t) + c$, whereas the variables $v(t)$ and $w(t)$ are invariant to translation (figure 2.7). Hence, projecting the attractor onto the (v, w) plane removes the effect of baseline wander.
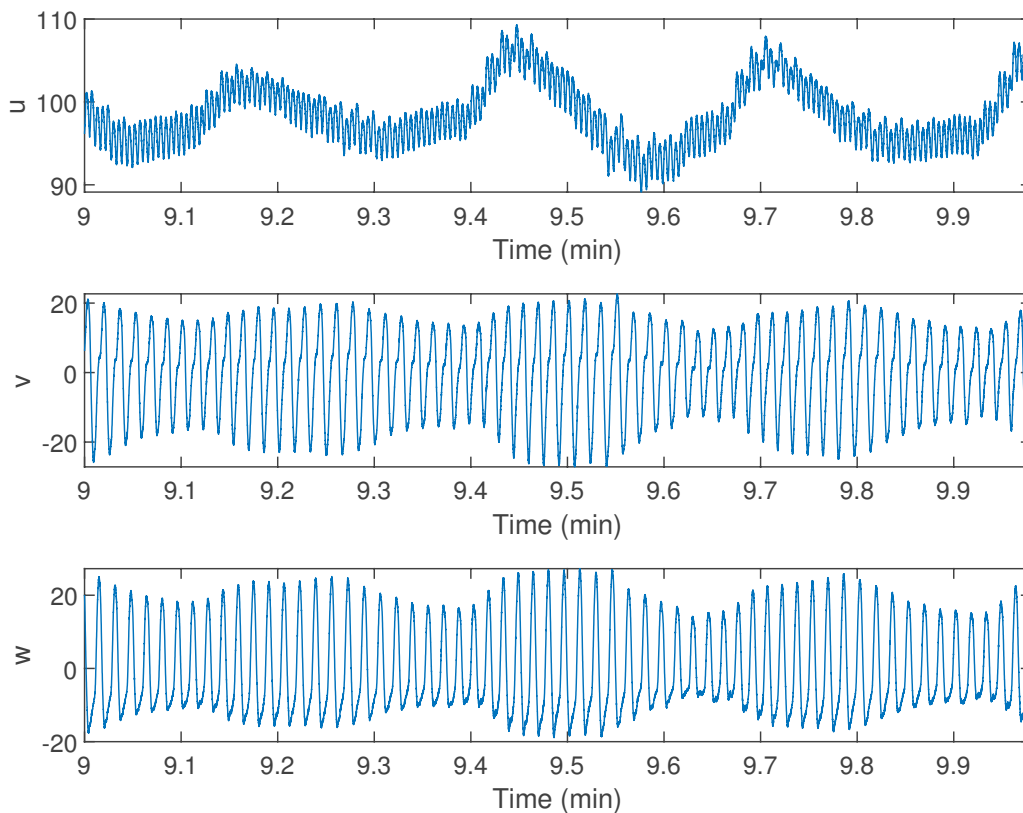

Figure 2.7.: Trajectories derived from the pulse waveform data shown in figure 2.6a. The variable u (top) picked up the trend in the data while the variables v (middle) and w (bottom) show no sign of baseline wander.

11

2.4.3. Construction of the density

The two dimensional attractor in the (v, w) plane consists of many overlapping lines which result in a messy picture with little visible detail. In order to enable the extraction of attractor features and their later comparison to features of the pulse waveform, a density is derived. The density marks regions where the trajectory often returns to, i.e. have a higher density, and other areas that are visited less frequently (figure 2.8b). Afterwards, this density plot needs to be quantified.
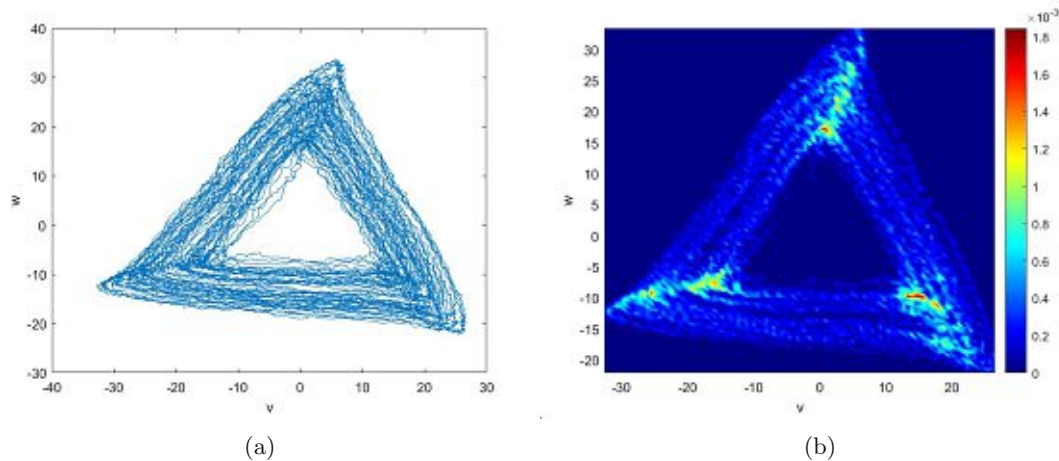

<div align="center">(a)   (b)</div>

Figure 2.8.: Removal of baseline wander and construction of a density: (a) a projection of the trajectory onto the plane orthogonal to the $x = y = z$ axis, (b) the trajectory turned into a density.

2.5. Benefits of Attractor Reconstruction

The advantages of attractor reconstruction are also highlighted in [5] and [29]. One major benefit of the attractor reconstruction method is that every single data point on the entire sampled waveform is used which may provide a deeper understanding of physiological or pathological changes within the cardiovascular system. Focussing only on maxima, minima and interval length alone might lead to missing these kinds of changes. Using all of the waveform data means that the end user hardly needs to edit the raw data before attractor reconstruction which therefore makes it resistant to bias introduction as hardly any pre- or post-processing is required. However, one should always examine the quality of the given data.

When arterial waveform data is plotted over a long period of time all that can be seen is the rise and fall of the average blood pressure, but hardly anything else. However, the change in shape and variability of a signal is also important to consider because it might be an indicator of several diseases [3, 46]. The attractor reconstruction method plots the signal in the three-dimensional phase space which means that all of the data is now constraint within a cube of a fixed size. As a result, it is now possible to observe the waveform's morphology and its change over a long period of time.

Another advantage of the method is that baseline variation has no effect on the pulse waveform data because it ignores movement in the y-axis of the raw signal. Therefore, the removal of baseline wander is not necessary and the possible exclusion of important information from the data does not cause difficulties anymore.

2.6. Attractor features compared to conventional pulse waveform analysis

Nandi et al. described in [29] how attractor features correlate with features of the pulse waveform morphology and how changes of the signal affect them. In the following subsections, different scenarios are presented. The results match the assertions made in [29].

2.6.1. Different heart rate

In the first scenario, different heart rates and the resulting attractors are compared to each other. The cycle length of the original pulse wave signal was therefore artificially cut in half so that the heart rate doubled. Other features, like the amplitude of the signal, stayed the same. As seen in figure 2.9, the generated attractors hardly differ despite the different heart rates. Therefore, changes in the heart rate have hardly any effect on the shape, size or orientation of the attractor.
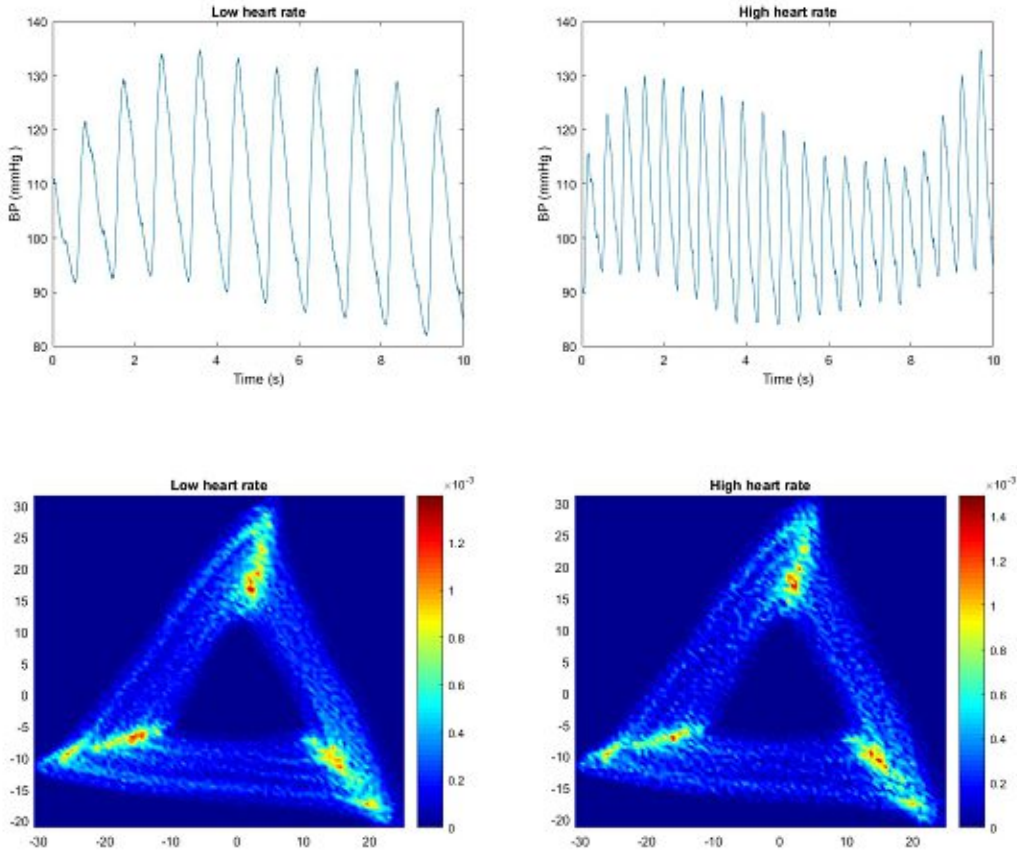
Figure 2.9.: Low heart rate (left) versus high heart rate (right).

2.6.2. Different pulse pressure

In the next scenario, the amplitude of a pulse wave signal is artificially raised which is equivalent to an increase of the overall pulse pressure. The resulting attractors are depicted in figure 2.10 and one can see that the attractor corresponding to the higher pulse pressure (left) is larger than the other one (right). Therefore, an increase in pulse pressure results in an overall increase of the attractor's size.
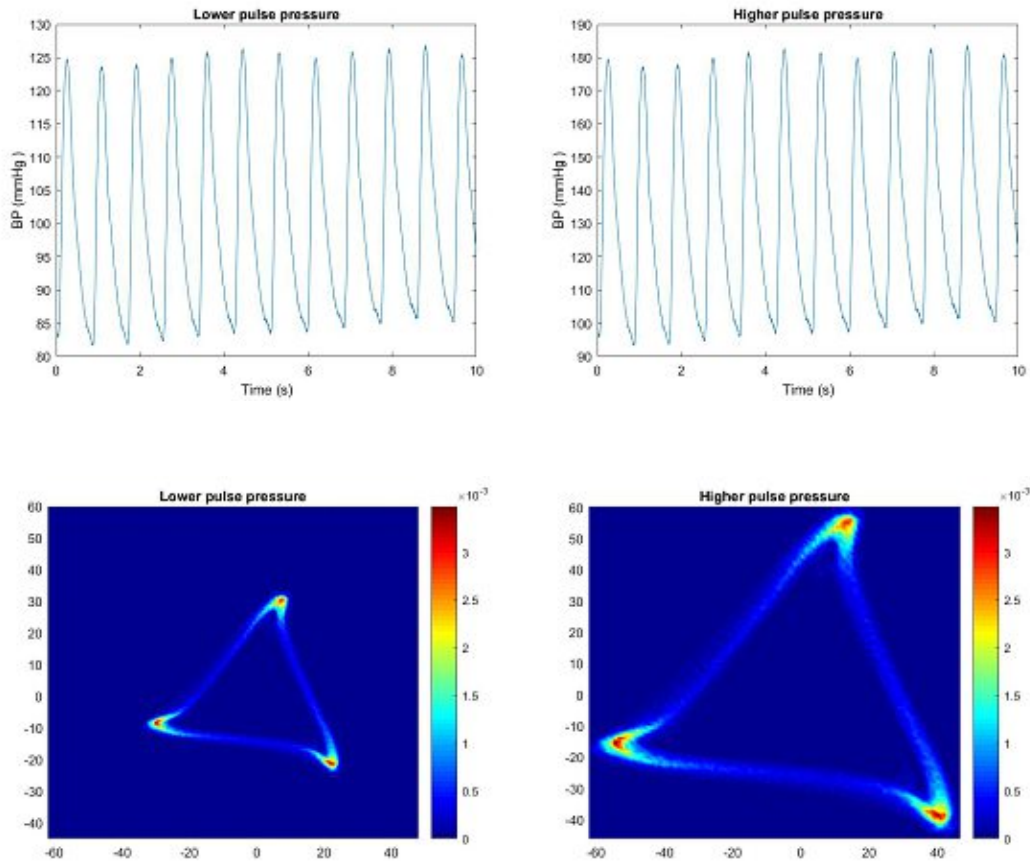
Figure 2.10.: Low pulse pressure (left) versus high pulse pressure (right).

2.6.3. Pulse wave variability

Unlike the heart rate variability (HRV) analysis, which offers beat to beat measures, the attractor reconstruction method can measure the variability of the entire waveform which may provide more information about the entire cardiac and peripheral vascular systems during the transition from health to disease [29].

Nandi et al. discovered that a waveform with high variability leads to a diffuse attractor with blurred sides, while well defined, slim sides arise from a more periodic signal. Figure 2.11 depicts a signal with low (left) and high variability (right) respectively and the corresponding attractors. The signal on the right side was again artificially modified by randomly adding 12 second fragments of other signals with similar amplitude to the original signal.
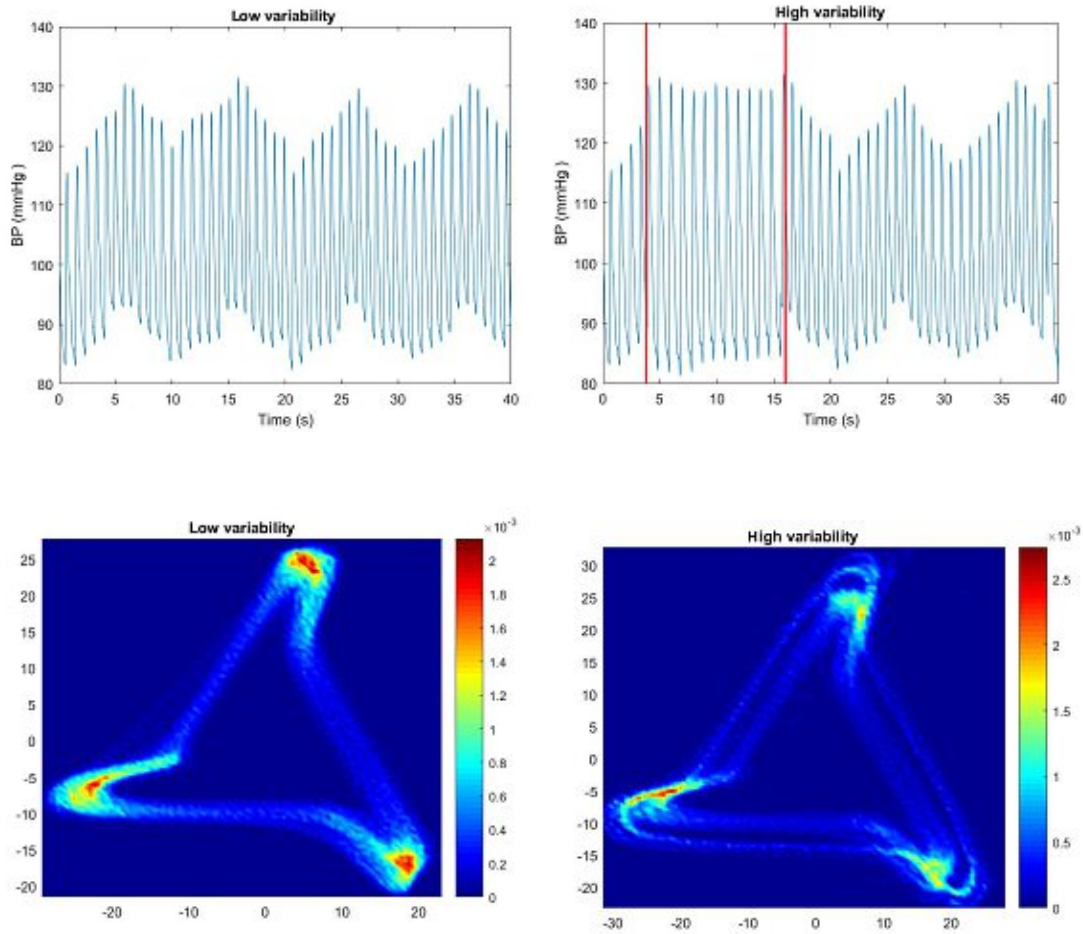
Figure 2.11.: Low variability (left) versus high variability (right). The artificially added fragment is highlighted in red.

2.6.4. Curvature changes in waveform downstroke

The curvature of the downstroke of an arterial pulse wave can correlate with its compliance and resistance. Alastruey et al. discovered in [2] that as resistance and compliance reduce, the downstroke can become more concave in shape. Then again, Nandi et al. linked the curvature of the downstroke of a pulse wave with the rotation of an attractor. They claimed that if the arterial pulse waveform downstroke becomes more concave, the attractor rotates clockwise. Figure 2.12 illustrates this fact. Although two different signals with similar systolic and diastolic blood pressure are used, the generated attractors differ in their orientation.
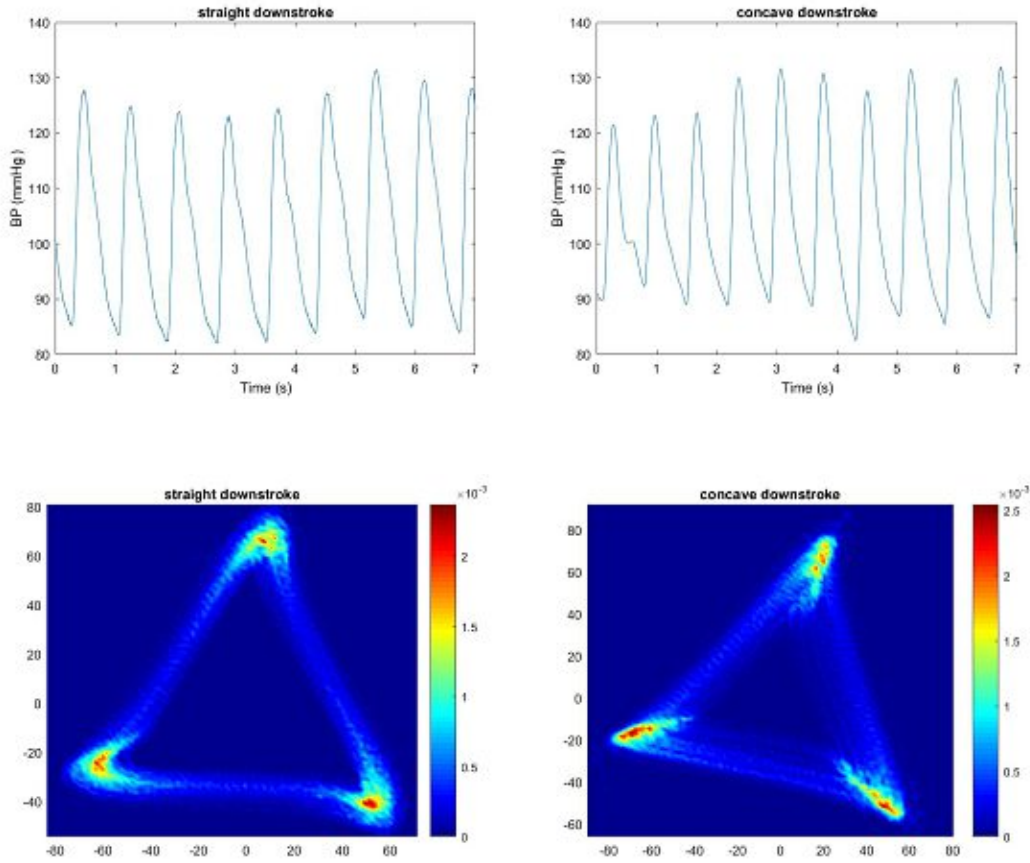
Figure 2.12.: Approximately straight downstroke and upright attractor (left) versus concave downstroke and clockwise rotated attractor (right).

2.6.5. Variation in cardiac contraction

In the next scenario, it is investigated how variability in the upstroke gradient, which likely correlates to beat to beat changes in the nature of cardiac contraction [29], affects the corresponding attractor. For this purpose, an artificial piecewise linear signal with a fixed downstroke gradient and a randomly varied upstroke gradient is generated following the method mentioned in [5]. The attractor reconstruction method revealed that variability in the gradient of the upstroke has a major influence on the movement in the right hand side of the attractor. Figure 2.13 illustrates the artificially generated piecewise linear signal and the corresponding attractor.

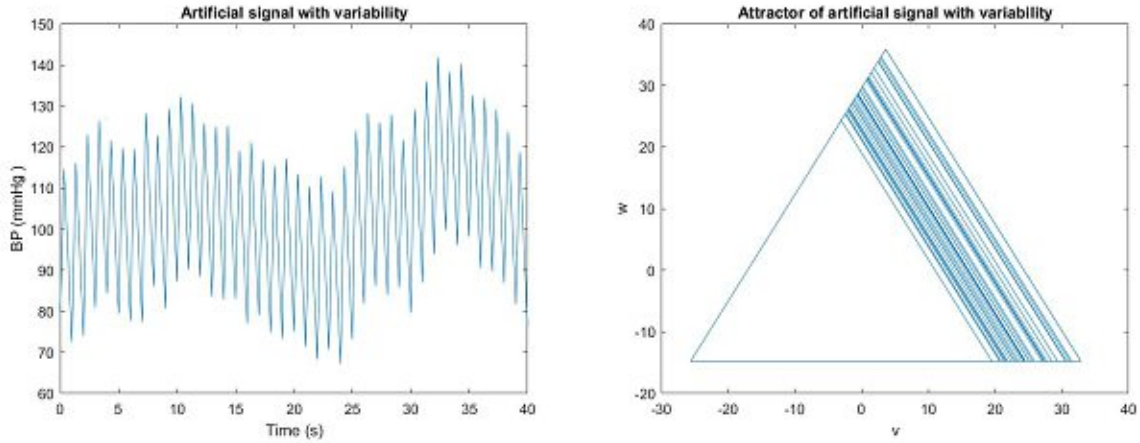Table 2.1 summarizes the results stated in this section.

Figure 2.13.: Artificial signal with fixed downstroke gradient und variable upstroke gradient (left) and corresponding attractor ploted onto the (v, w) plane (right).

Pulse waveform features	Attractor features	Physiological interpretation
Decrease in cycle length	No change in attractor	Increase in heart rate
Increase in amplitude	Attractor size increases	Increase in pulse pressure
Waveform almost periodic	Very thin sides of the attractor	Heart rhythm almost periodic
Varying waveform	Diffuse attractor with blurred sides	Varying heart rhythm
Increased concavity of downstroke	Clockwise rotation of the attractor	Decrease in resistance and compliance
Downstroke variability	Variability in right hand side of attractor	Variability in cardiac contraction

Table 2.1.: Summary of waveform features, corresponding attractor features and physiological interpretation. Adapted from [5].

3. Statistics and Data Description

3.1. Data

All data used in this thesis was originally collected in a pilot study [6] conducted by AIT in conjunction with the Clinical Research Institute in Dortmund, ines mikisek coaching and the Kerckhoff Clinic. Previous studies have shown that respiration and relaxation techniques, like mantra breathing or yoga, have a positive impact on blood pressure [7, 9, 19]. Hence, the pilot study focused on the effect of device-guided slow breathing with immediate biofeedback and examined how the pulse arrival time, which is inversely proportional to the blood pressure, changes over time.

The pulse wave data used in this thesis was acquired through photoplethysmography (PPG) at the fingertip of 30 patients with treated arterial hypertension. Table 3.1 summarizes the baseline characteristics of these subjects.

N (#)	30
Age (years)	62.9 (7.7)
Gender (#, #)	11 females, 19 males
Body height (cm)	174.4 (10.4)
Body weight (kg)	87.6 (18.9)
BMI	28.6 (4.7)
Arterial hypertension since (years)	11.4 (10.2)
Systolic blood pressure (mmHg)	133.0 (17.1)
Diastolic blood pressure (mmHg)	83.8 (10.6)
Spontaneous respiratory rate (bpm)	13.6 (1.9)

Table 3.1.: Baseline characteristics of the subjects. Data expressed as mean (standard deviation) or in absolute numbers. Adapted from [6].

The examination was carried out in a comfortable sitting position that allowed free abdominal breathing. The subjects were guided to the most uniform breathing with the aim to reach an average of ten to twenty breaths per minute in everyday life or a maximum of six to eight breaths per minute during respiratory therapy. A ready-to-use "Biosignal Explorer" system (biosignalsplux, Lisbon, Portugal) was used for recording. The breathing guidance was implemented as a custom-made application for Android smartphones and tablets. During ten minutes

of exercise, a balloon shown on the screen symbolised the individual durations of expiration and inspiration of the users. As the balloon rose, users had to inhale and as it sank, users had to exhale. Holding the breath was indicated by the balloon stopping at the top or bottom of the screen (figure 3.1). The guided breathing phase was followed by a five minute unguided cooling down phase: during this phase the subjects had to continue to breath calmly. For this purpose, the balloon was completely hidden. Afterwards, the recorded data was gathered for further analysis.

Figure 3.1.: Screenshot of the Android App during the slow breathing exercise. Adapted from [6].

3.2. Statistical Methods

Each data set of the 30 subjects was about 15 minutes long. In order to generate a sound attractor and capture its changes over this period of time, the data set was divided into three subsets of 100 seconds according to [29]. The first signal covered the recording's first 100 seconds and represented the baseline. The second subset spanned from second 500 to second 600, representing the end of the guided breathing phase and the last subset was chosen to represent the end of the cooling phase from second 800 to second 900. Each of the three signals generated an attractor with several features. The mean value and the standard deviation of each feature in every subset were calculated and additionally, the results were plotted as boxplots for direct comparison. To analyse the difference between the subsets, a Friedman test was performed. If the Friedman test revealed a (borderline) significant difference between baseline,

end of guided breathing and end of cooling down, the Bonferroni post-hoc test was applied. The resulting corrected p-values indicate the significance of differences between the subsets, where a low corrected p-value corresponds to a high significance. The level of significance α was chosen to be 5%, i.e. the null-hypothesis of the test can be rejected if $p < 0.05$. Furthermore, a sliding window of 100 seconds was applied in order to illustrate the changes of the attractor features throughout the entire signal. The means across all subjects along with the 95% confidence interval were calculated and the results were plotted as functions over time as difference from the baseline value.

4. Methodology and Implementation

This chapter represents the main part of the thesis and focuses on the quantification of the reconstructed attractors. In order to detect changes in shape and variability of the pulse waveform over time, it is necessary to determine certain measures and parameters of the attractor.

All implementations were done in MATLAB® version R2019b. In the first step, pulse wave data was scaled to a blood pressure level of about 120/80 mmHg and the three starting points, i.e. baseline, end of guided breathing and end of cooling down, were chosen for the evaluation. As stated in section 3, each of the three selected signals for the attractor reconstruction was 100 seconds long. In order to remove non-physiological artefacts, the pulse wave data was preprocessed (section 4.1). Afterwards, the attractor was generated according to the steps explained in section 2.4 and filtered to remove remaining artefacts (section 4.3). Section 4.4 addresses the quantification of the attractor and its implementation. Figure 4.1 summarizes the processing steps.
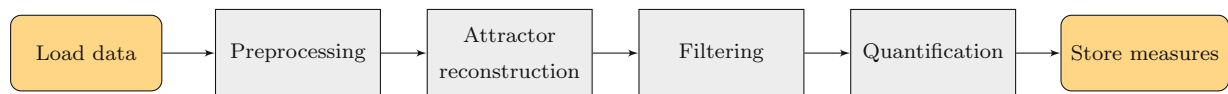

Figure 4.1.: Flowchart representation of the applied algorithm.

4.1. Preprocessing

One of the advantages of attractor reconstruction is that the method uses data in its entirety and does not focus on specific points like the oneset point of a pulse wave or interval lengths. As a result, hardly any data preprocessing is needed which makes the method more resistant to bias introduction [29]. Nevertheless, it is necessary to remove artefacts (e.g. caused by movement) because outliers can possibly lead to a miscalculation of attractor measures (figure 5.3). One way of detecting artefacts, or rather pulse wave fragments with irregular behaviour, is to divide the signal in sections. The length of each section is empirically chosen to be 4 seconds. Figure 4.2a shows artefactual noise at the beginning of the signal, characterized by very high and low extrema. To detect possible artefacts in each of the 25 segments, the minima and the maxima and their differences are calculated and compared to each other. The built-in MATLAB® function *isoutlier* is used to detect outliers in the set of the maximum-to-minimum differences,

whereas an outlier is characterized by an element that is more than three scaled MAD (Median Absolute Deviation) from the median. The scaled MAD is defined as

$$\text{MAD} = -\frac{1}{\sqrt{2} \cdot \text{erfcinv}(\frac{3}{2})} \cdot \text{median}(|x - \text{median}(x)|),$$

where x denotes the vector of the maximum-to-minimum differences and *erfcinv* is the inverse complementary error function. Thereafter, segments containing artefacts are removed and the previous and following sections are linked together at the peak of the last or first pulse wave, respectively. In order to get a signal that is again 100 seconds long, the missing pieces are added at the beginning or at the end of the signal.
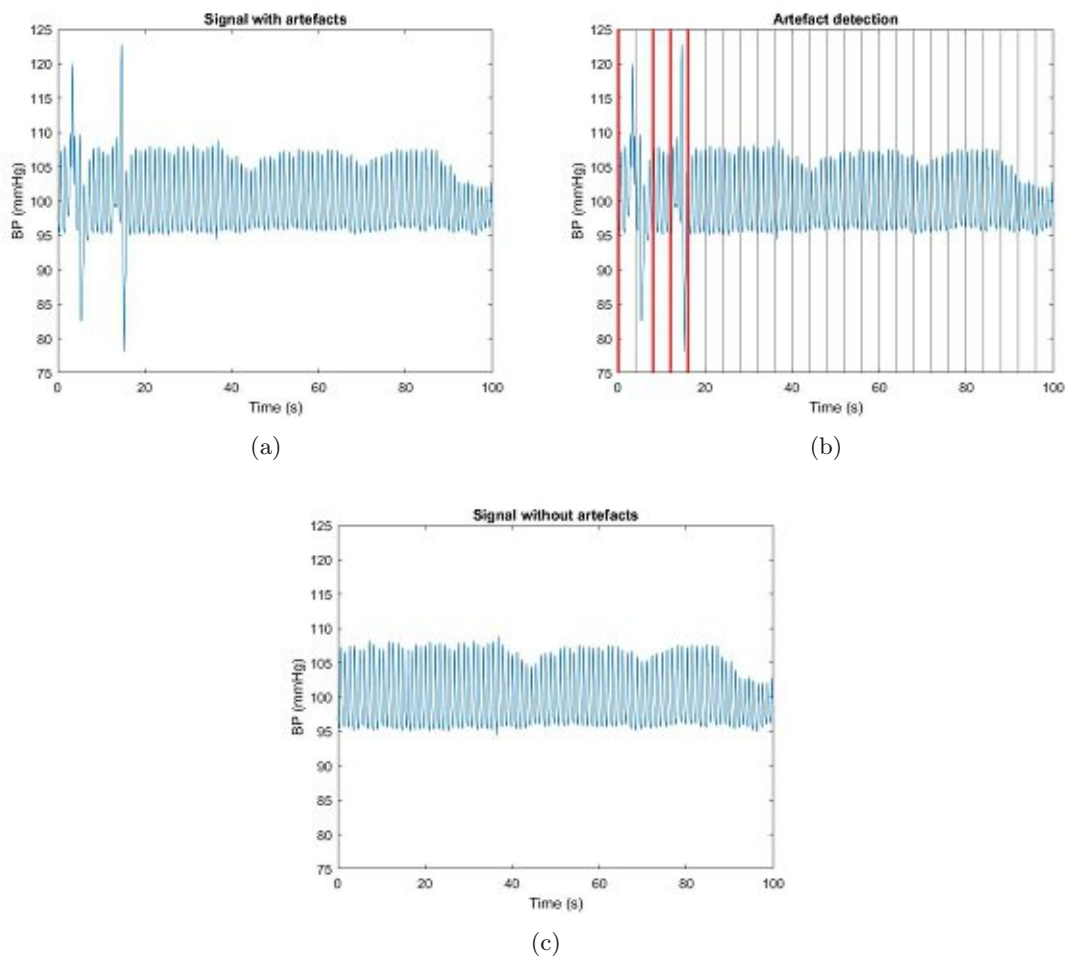

Figure 4.2.: Steps of signal preprocessing: (a) Signal of 100 seconds with artefacts at the beginning, (b) the signal is divided in 25 section of 4 seconds. The red lines mark sections containing outliers (here segment 1,2 and 4), (c) signal after removing sections with outliers and adding missing fragments.

4.2. Attractor Reconstruction

After removing outliers from the signal, the attractor is generated. Each of the considered signal fragments has a duration of 100 seconds and a sampling rate of 256 Hz. In the first step, the time delay τ is calculated as explained in 2.4

$$\tau = \frac{\text{average heart rate}}{3}.$$

In order to determine the average heart rate, autocorrelation is used. Figure 4.3 represents this process: the highest positive correlation is given exemplarily at a delay of 247 indices, i.e. the average heart rate is about 62 beats per minute (bpm).
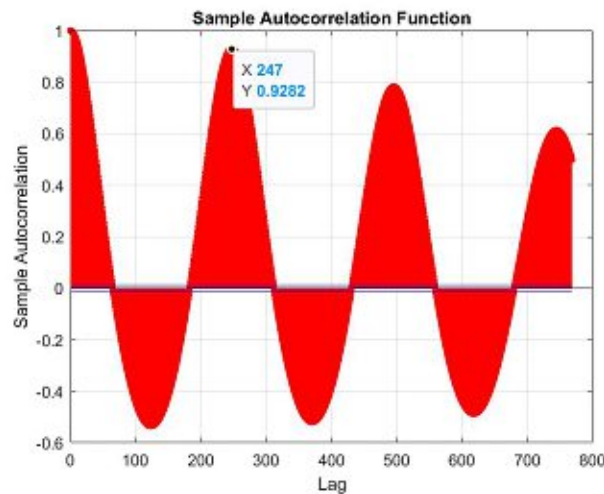

Figure 4.3.: Autocorrelation of a signal.

Afterwards, an initial point is chosen and is denoted as the first x-coordinate. The coordinates y, z are defined as τ and 2τ indices before x, respectively. The resulting triplet, consisting of three independent values of the data signal, is plotted in the three dimensional phase space (figure 4.4a). Passing through the signal results in numerous overlapping loops and the so called three dimensional attractor is created. According to formula (2.1), new coordinates (u, v, w) are calculated and the attractor is plotted onto the (v, w) plane (figure 4.4b). The density of the two dimensional attractor is constructed with the MATLAB® function `densityplot.m`, available on the MathWorks® file exchange server[1]. This function uses a square grid of 100×100 boxes and the volume is normalized to be one, generating a 100×100 density matrix N (figure 4.4c).

---

[1] *https://de.mathworks.com/matlabcentral/fileexchange/65166-densityplot-x-y-varargin*
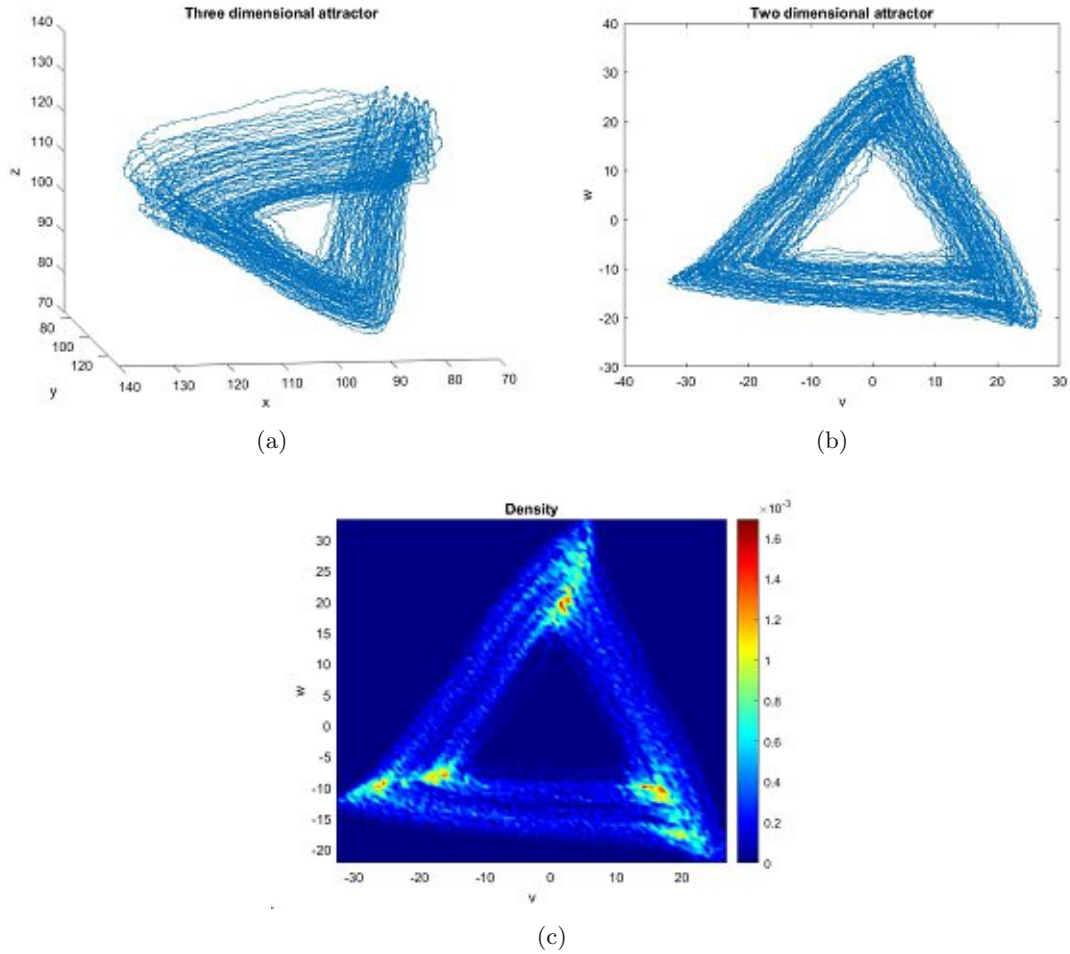
(a)

(b)

(c)

Figure 4.4.: Attractor reconstruction steps: (a) Three dimensional attractor, (b) attractor plotted onto the (v, w) plane, (c) construction of a density.

4.3. Median Filter

In addition to the method explained in 4.1, a two dimensional median filter is applied to the density plot of the attractor in order to remove the remaining noise. Figure 4.5a shows an attractor with rather chaotic structure which might distort its later calculated measurements, as highlighted in the red ellipse.

Median filtering is a common nonlinear method for noise elimination in images. For each pixel in the image a $m \times n$ neighborhood ω is selected and the median value of the pixels within this kernel frame is computed. The pixel located at the coordinates of the kernel center is set to the median value

$$N'(x, y) = \text{median}(N(x + i, y + i), (i, j) \in \omega).$$

Entries that are smaller than half the size of the median filter kernel are removed by the filter

25

and it does not affect large discontinuities such as edges and large changes in image intensity in terms of gray-level intensity, although their position may be shifted by a few pixels. [34]

The median filter is applied to the 100×100 density matrix N that has been converted into a grayscale image and a 3×3 neighborhood is chosen which proved to be suitable for the data used in this thesis. In order to remove artefacts but still preserve the basic structure of the attractor, all values of N, that the median filter has not removed, stay the same and the others are set to 0:

$$N(x,y) = \begin{cases} 0, & if\ N'(x,y) = 0, \\ N(x,y), & if\ N'(x,y) \neq 0. \end{cases}$$

Figure 4.5b shows an attractor after applying the median filter.
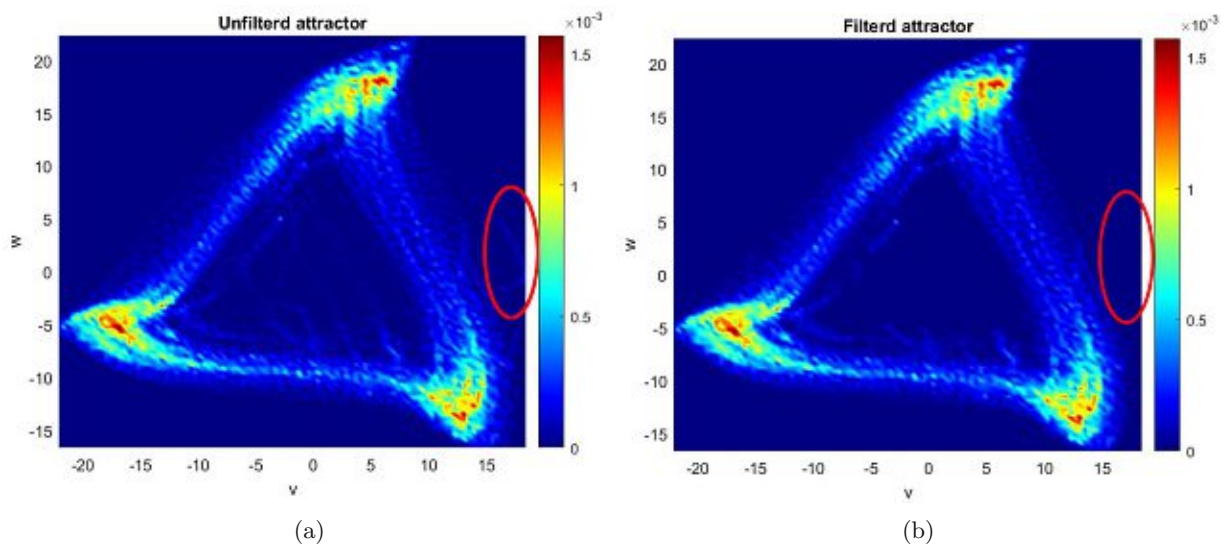

(a)

(b)

Figure 4.5.: Applying a median filter on a density plot of an attractor: (a) Unfiltered attractor with artefacts characterized by chaotic lines in the middle and on the right side of the attractor (exemplarily circled in red), (b) attractor after applying a two dimensional median filter with a 3×3 neighborhood.

4.4. Quantification of the Attractor

In [5], Aston et al. suggested a few ways to quantify some attractor features. However, only a few ideas turned out to be suitable because in contrast to the piecewise signal applied in [5], the signal used in this study tends to have more curvature changes. The most promising approach to gather information on attractor features was image processing combined with the usage of the 100×100 density matrix. The calculations were done by means of the MATLAB® Image Processing Toolbox [23]. Figure 4.8 summarizes the feature extraction procedure, introduced in the following subsections. In the first step, the generated attractor is rotated anticlockwise by θ so that its lower band becomes horizontal (figure 4.12). Due to different ratios of the crest time to τ, some of the attractors look like triangles, others have bends at each side (figure 4.15). So in the next step, the angle between the fragments of the attractor arms are calculated. Based on the result, the attractor is divided into two different shapes and depending on its structure, lengths and heights are determined. Finally, the band widths of the attractor arms are calculated.
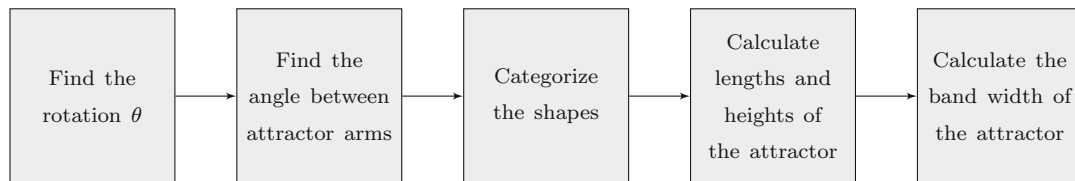
Find the rotation θ	Find the angle between attractor arms	Categorize the shapes	Calculate lengths and heights of the attractor	Calculate the band width of the attractor

Figure 4.6.: Procedure of feature extraction

4.4.1. Rotation of the Attractor

In the first step, the attractor has to be rotated. On the one hand, this provides information on the downstroke of the attractor and, on the other hand, makes further calculations easier.

In a first attempt, the attractor was rotated in an anticlockwise direction by θ and the density vector d was determined by calculating the row sum of the 100×100 density matrix. Aston et al. suggested in [5] that the density vector d would have the greatest maximum, if the bottom edge of the attractor was horizontal. Thus,

$$\hat{\theta} = \operatorname*{argmax}_{\theta}(\max_{i} d_\theta(i)), \tag{4.1}$$

should yield the optimal angle of rotation $\hat{\theta}$. However, this method proved to be unsatisfactory for the more complex data used in this thesis (see figure 4.7).
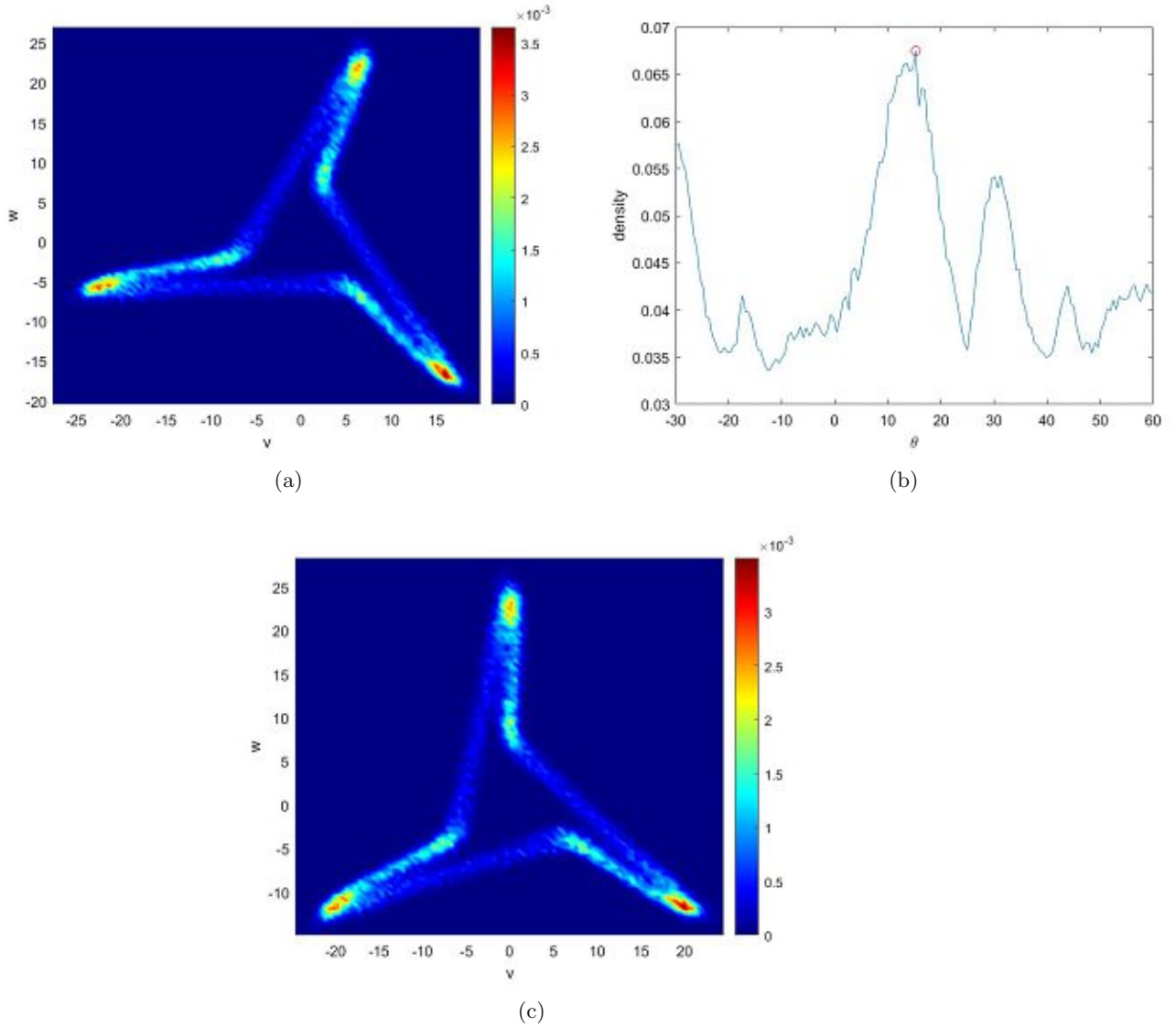
(a)

(b)

(c)

Figure 4.7.: Wrong calculation of the angle of rotation according to (4.1): (a) Original attractor that has to be rotated, (b) angle of rotation and corresponding density values, (c) rotated attractor.

Consequently, a new approach had to be found and image processing turned out to be the most promising one. The steps of the following algorithm that determine the angle of rotation are depicted in figure 4.8.
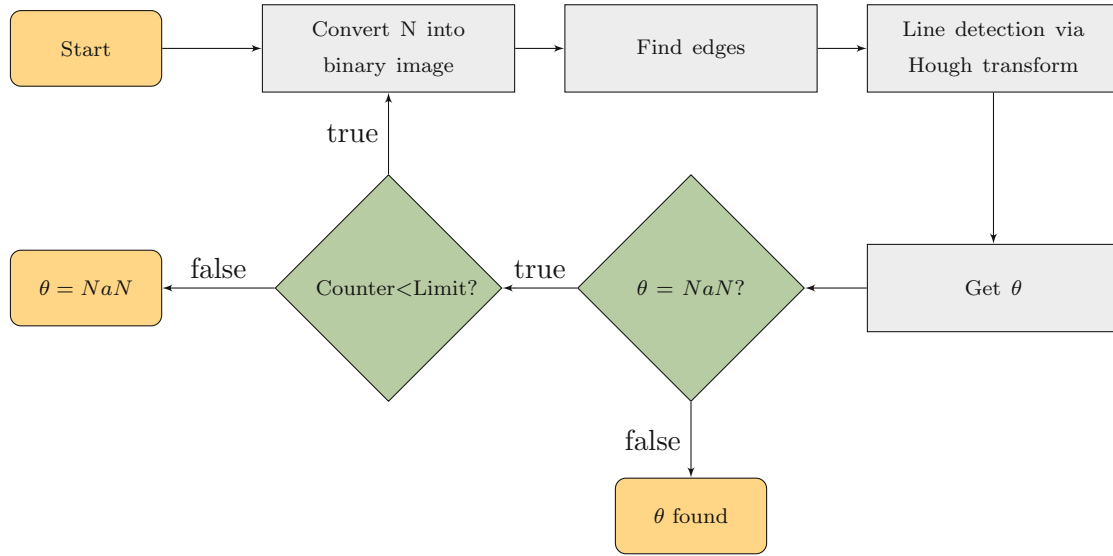
Figure 4.8.: Flowchart representation of the determination of the rotation θ.

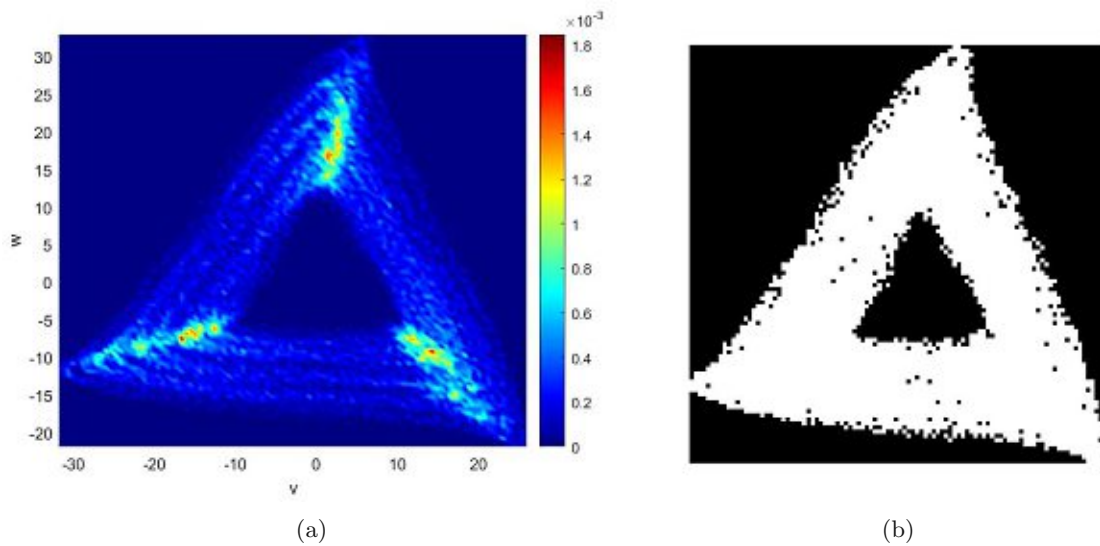(a)   (b)

Figure 4.9.: Conversion into a binary image: (a) Density plot of an attractor, (b) corresponding binary image where only entries greater than or equal to 1% of the maximum value are considered.

Figure 4.9a shows an attractor in its original form with blurred edges. In order to properly detect edges and eventually straight lines, the density matrix N has to be converted into a binary image (figure 4.9b). In the following, the whole procedure is described:

- In order to neglect remaining outliers, find all entries of the density matrix N that are greater than empirically chosen 1% of its maximum entry and set them to 1; all other entries are set to 0. Convert the matrix with the function $I = mat2gray(N)$ into a 100×100 grayscale image I.

29

- Use the MATLAB$^{\circledR}$ function $BW = edge(I,'Prewitt','horizontal')$ to find edges in the binary image that are approximately horizontal (figure 4.11a).

- Detect lines by means of the Hough transform and return their position and angle (figure 4.11b):

  - The function $[H,t,r] = hough(BW)$ is designed to detect lines in a binary image BW. The parametric representation of a line: $\rho = x\cos(\theta) + y\sin(\theta)$ is used. The function returns ρ, the perpendicular distance from the origin to the line, and θ, the angle between the x-axis and this perpendicular vector (figure 4.10), as well as the Standard Hough Transform (SHT) H, a parameter space matrix, whose rows and columns correspond to ρ and θ values, respectively. Any point within the image is mapped to a sinusoidal curve in the Hough space. If two points are located on the same line segment, the two generated curves in the Hough space overlap at a location that corresponds with this line in the image space [11, 23].
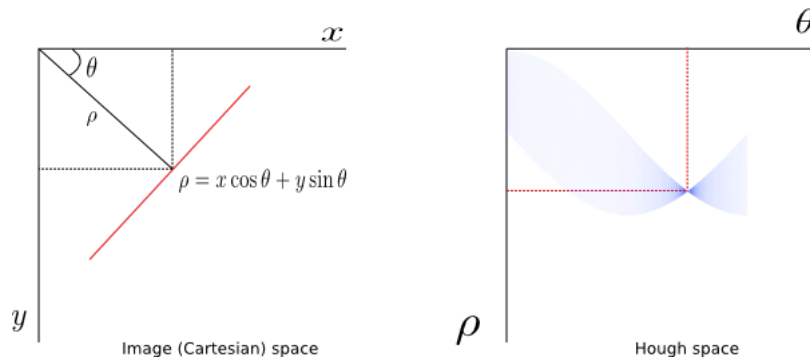

Figure 4.10.: Representation of a line in Cartesian (left) and Hough (right) coordinates. Adapted from [36].

  - After computing the Hough transform the function
    $P = houghpeaks(H, 2,'threshold', ceil(0.3 * max(H(:))))$ locates peaks (overlapping sinusoidal curves) in the Hough transform matrix H and returns the row and column coordinates of the peaks. In this thesis, maximal 2 peaks or rather maximal 2 lines in the image space are considered. The minimum value that is recognized as a peak is 30% of the maximum value of H and has been empirically chosen.

  - The function $lines = houghlines(BW, t, r, P,'FillGap', 15,'MinLength', len)$ uses the previously obtained information and extracts line segments in the image BW and returns their angle and position. In order to ensure that only the dominant lower edge of the attractor is considered, the minimum length of a line is set to $len = 30$ pixels.

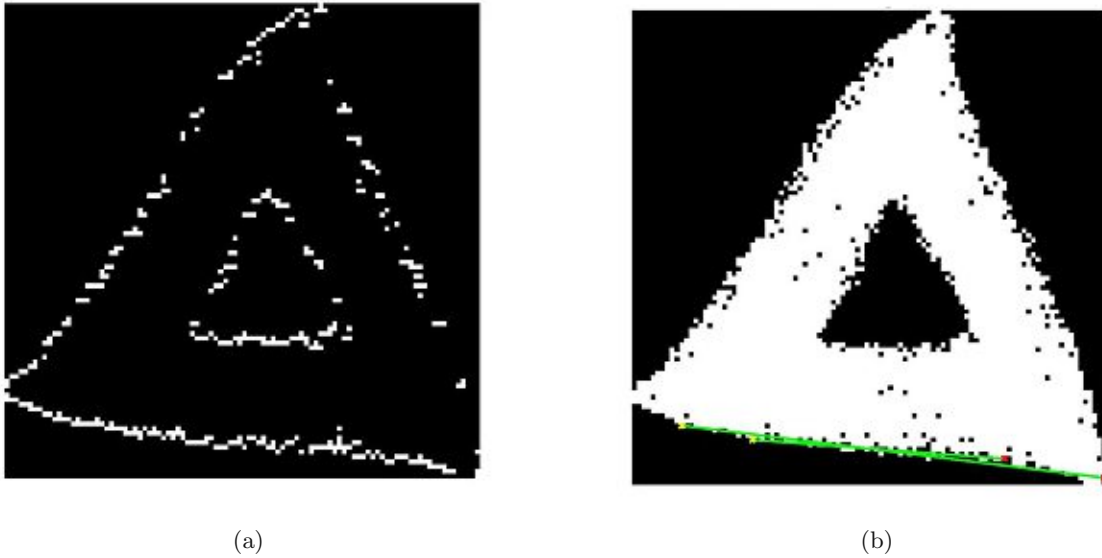<div align="center">(a)   (b)</div>

Figure 4.11.: Detection of a line: (a) Edge detection in binary image, (b) Line detection via Hough transform.

The variable *lines* contains 0,1 or 2 detected lines or more specifically their position and angle (see figure 4.11b). In the next step, the function $get\_angle(lines, threshold)$ calculates the mean angle of rotation θ:

- In order to ensure that only lines representing the lower edge of the attractor arm are considered, make the following assumption based on the given data: the angle of a line is considered to be suitable if it is within a threshold of 15 degrees above or below the horizontal line. If no detected line meets this condition, set θ to NaN, otherwise take the mean value of the feasible angles. Return θ.

- If $\theta \neq NaN$: The angle of rotation is found.

- If $\theta = NaN$:
    - If counter<5: start at the beginning but this time find all entries of the density matrix N that are greater than $(1 + \text{counter})\%$ and reduce the minimum length of a line to $len = 15$; increase counter by 1.
    - If counter=5: θ equals NaN and all other parameters are set to NaN as well. Stop the feature extraction procedure.

If $\theta \neq NaN$, rotate the attractor anticlockwise by θ in the (v, w) plane as seen in figure 4.12:

$$\begin{bmatrix} v_{rot} \\ w_{rot} \end{bmatrix} = \mathrm{R} \cdot \begin{bmatrix} v \\ w \end{bmatrix}, \qquad \mathrm{R} = \begin{bmatrix} \cos(\theta) & -\sin(\theta) \\ \sin(\theta) & \cos(\theta) \end{bmatrix}. \tag{4.2}$$
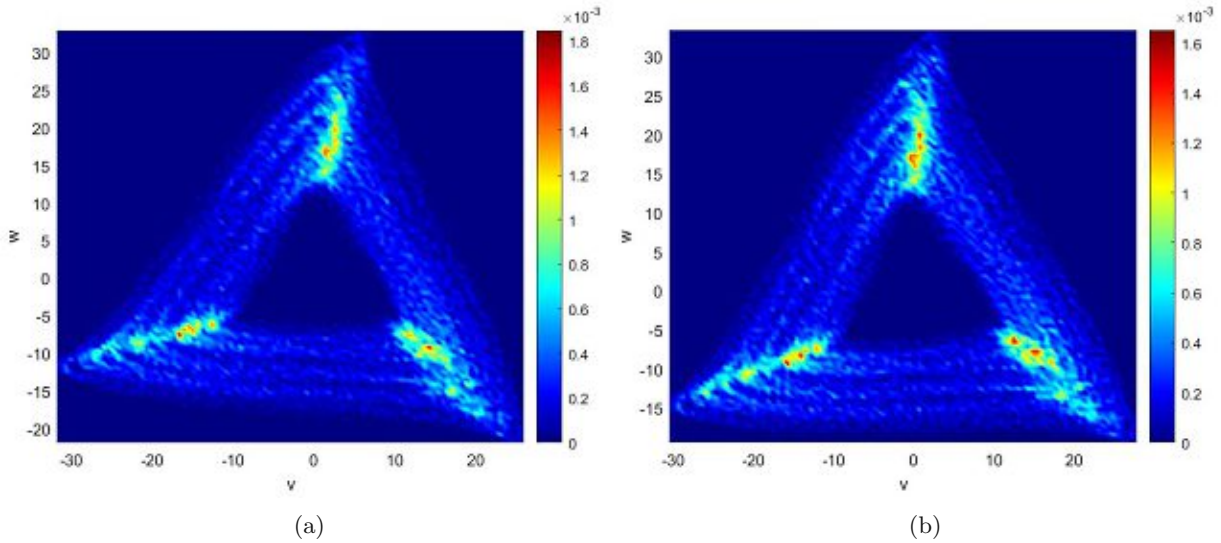
Figure 4.12.: Rotation of the attractor: (a) Original attractor, (b) rotated attractor.

4.4.2. Angle between Attractor Arms

Attractors can vary in shape depending on the used signal. Some attractors look like triangles, others have bent sides. Thus, the next parameters to be calculated are the angles between the attractor arms β and consequently the different shapes. At first, the angle of rotation α has to be found and after that, $\beta = 180° - \alpha$ can be determined (figure 4.13). Figure 4.14 summarizes the following algorithm:
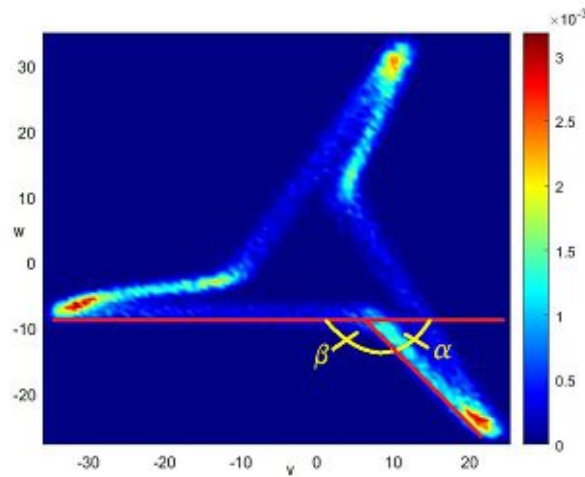

Figure 4.13.: Angle between the parts of the attractor arm.

- Set the interval length and the step size of the angle α; in this study, an angle between 0 and 60 degrees and a step size of about $\frac{\pi}{300}$ degrees are used. Rotate the attractor by the first entry of the vector α in an anticlockwise direction (see formula (4.2)).

32

- Convert the 100×100 density matrix N into a binary matrix because only the shape of the attractor and not the density of different regions is relevant. Use entries that are greater than an 5% of the maximum value: this was empirically chosen according to the given data set; others are set to 0. Adjust the size of the matrix so that the attractor covers the full image by determining the leftmost, rightmost, lowest and topmost non-zero entry.
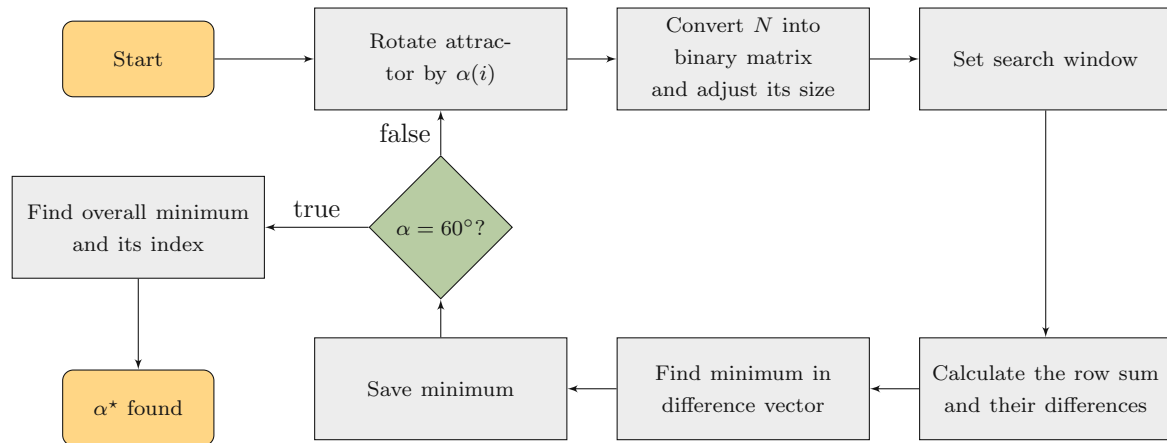

Figure 4.14.: Flowchart representation of the determination of the angle β between the attractor arm fragments.

- The bend of the attractor arm is usually located in the south east quarter of the density matrix. Set the search window on this area.

- Sum up the entries in each row within the search window and calculate the differences between adjacent values of this row sum vector.

- The more horizontal the right fragment of the lower attractor edge becomes, the higher is the negative difference in the row sum vector. Find the minimum in this vector of differences and save it.

- Repeat this procedure until $\alpha = 60°$.

- Find the minimum value in the vector of minima and its index $i^\star$. This implies the sought angle of rotation $\alpha^\star = \alpha(i^\star)$. Return $\alpha^\star$.

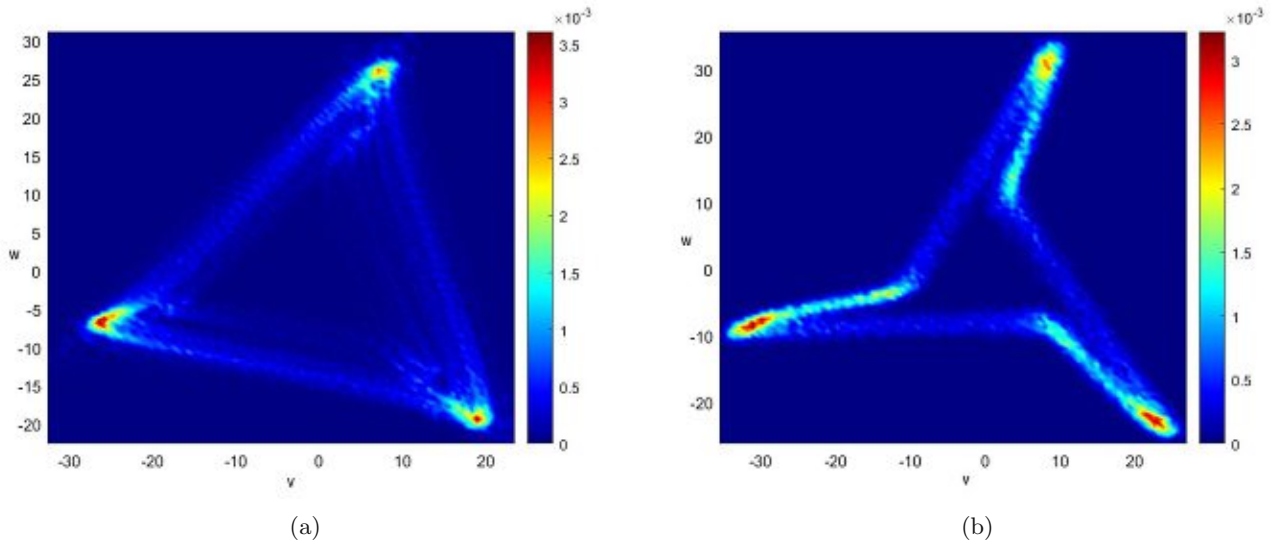(a)   (b)

Figure 4.15.: Different shapes: (a) Triangular attractor, (b) attractor with bent sides.

As mentioned before, the angle β between the fragments of the lower attractor arm is determined by $\beta = 180° - \alpha$. Due to the choice of the time delay τ, the attractor has 3-fold rotational symmetry [5]. So, in order to get the other two angles of the bends of the two remaining sides, the attractor is rotated by 120 and 240 degrees, respectively, and the procedure is repeated, which results in the vector $\beta = (\beta_1, \beta_2, \beta_3)$.

An attractor is said to be triangular in shape, if at least two of the three angles are greater than or equal to 165 degrees. Otherwise, its shape is understood as bent (figure 4.15). This categorization is necessary to prevent falsely calculated measures in the further feature extraction process. A threshold of 165 degrees proved to be appropriate for the given data set.

4.4.3. Lengths and Heights of the Attractor

As the pulse pressure increases, the overall size of the attractor increases as well. Thus, in the next step, lengths and heights of the attractor have to be calculated. As mentioned in the previous section, differences in waveform morphology lead to different attractor shapes and measurements. As opposed to attractors that are nearly triangular in shape, each arm of a bent attractor consists of two parts. In the following, the length of the more horizontal edge is referred to as length a and the other one as length b (figure 4.16). The following algorithm is illustrated in figure 4.17:

- Calculate the column sum of the density matrix N. In order to neglect possible outliers in the density matrix, find all entries of the column sum vector that are greater than or equal to 5% of its maximum value, which again was empirically chosen. The position of the first entry denotes the v-coordinate of the leftmost point, the last entry denotes the v-coordinate of the rightmost point of the attractor.
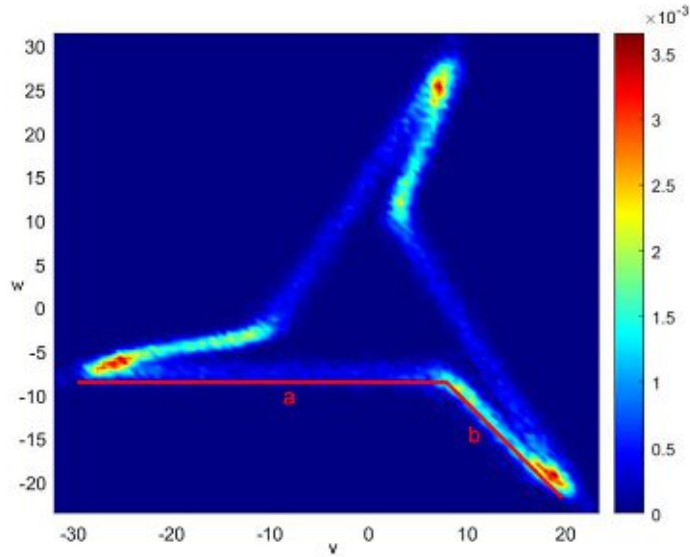
Figure 4.16.: Denotation of the sides of a bent attractor.

- Calculate the row sum of the density matrix N. Again, consider only entries of the row sum vector that are greater than or equal to 5% of its maximum value. The position of the first entry denotes the w-coordinate of the highest point of the attractor. The lowest point of the attractor - bent or not - is usually located in the south east quadrant of the density matrix. Thus, adjust the matrix and consider only the columns that are right of the center. Calculate the row sum of this adjusted matrix and find all entries that are greater than or equal to 5% of the maximum value of the vector. The position of the last entry labels the w-coordinate of the lowest point of the attractor.
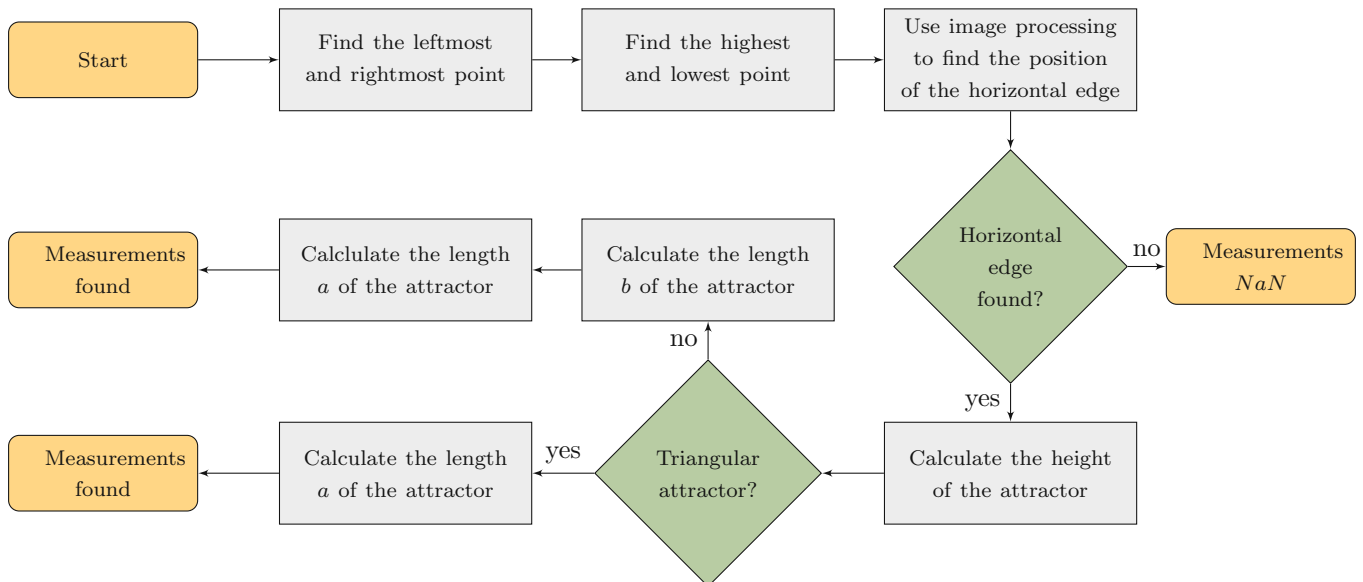

Figure 4.17.: Flowchart representation of the determination of the attractor lengths and heights.

35

- Use the binary matrix and the Hough transform, as described in section 4.4.1, to detect the position of the approximately horizontal edge of the attractor.

  – In order to find a line that represents the horizontal edge of the attractor, consider only the one within a few degrees above or below the horizontal line. Applied to the given data set, 12 degrees proved to be suitable. If two lines fulfil this condition, choose the lower one. If the chosen straight line is not horizontal, calculate the middle point. The horizontal line through the w-coordinate of this point represents the edge of the attractor. If the chosen line is level, the position and representative of the edge is found (figure 4.18).

  – If no suitable line is found, all measurements are set to NaN. Stop the procedure.

- The height h of the attractor is defined as

$$
h = \begin{cases} h\_p_w - l\_p_w, & \text{if } l\_p_w < h\_line, \\ h\_p_w - h\_line, & \text{otherwise,} \end{cases}
$$

where h_p_w and l_p_w denote the w-coordinate of the highest and lowest point, respectively, and h_line denotes the vertical position of the horizontal line.

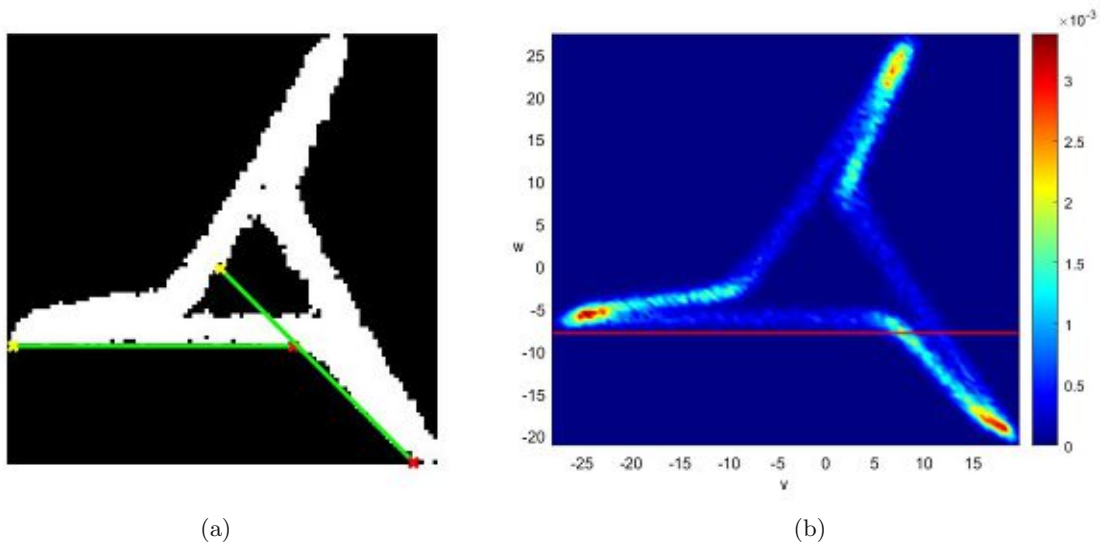(a)   (b)

Figure 4.18.: Determination of the position of the horizontal edge: (a) Line detection via Hough transform, (b) Position of the horizontal line.

- If the considered attractor is a triangle, the length of the lower edge a is defined as

$$
a = rm\_p_v - lm\_p_v,
$$

36

where rm_p_v and lm_p_v denote the rightmost and leftmost point, respectively. The length b is set to 0 (figure 4.19a).

- If the attractor has bent sides, the length b of the arm is determined by

$$b = \frac{|l\_p_w - h\_line|}{\sin(\alpha)}$$

- Find the v-coordinate of the lowest point of the attractor by locating the maximum value in the row of the density matrix corresponding to the w-coordinate of the point. Determine the straight line through this point approximating the edge of the attractor with length b:

$$k = \tan(-\alpha), \qquad d = l\_p_w - l\_p_v \cdot k.$$

Calculate the intersection between the line representing the horizontal edge and the straight line through the lowest point. The length a of the horizontal arm is determined by the difference between the leftmost point and the intersection (figure 4.19b).

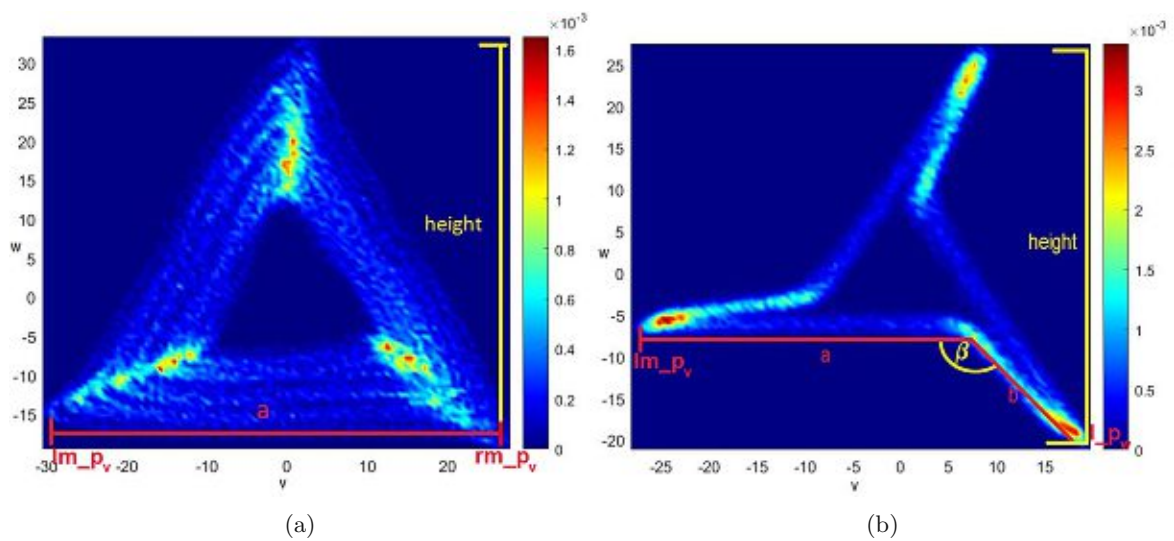<table>
<tr><td>(a)</td><td>(b)</td></tr>
</table>

Figure 4.19.: Lengths and heights of the attractor: (a) Measures of a triangular attractor, (b) measures of a bent attractor.

For better comparison the ratio $\frac{b}{a}$ is built. Clearly, the ratio is 0, if the considered attractor is triangular. Due to the 3-fold symmetry, the calculation can be repeated after rotating the attractor by 120 and 240 degrees, respectively.

4.4.4. Width of the Attractor

The width of the attractor arms is an instructive measure regarding the variability of the waveform shape in each cycle. As mentioned before, slim attractor sides relate to a more periodic signal, whereas broad, blurred arms correspond to a signal with high variability.

In order to calculate the width of one side, a search area, depending on the shape of the attractor, has to be determined. Triangular attractors tend to be approximately symmetrical about the w-axis; therefore, the search window is located in the middle of the lower edge. The window should cover a significant area but should not be too broadly defined because the other two edges of the attractor might affect the calculation. Therefore, the size of the window is chosen to be 10% of length a, which granted the best results for the given data set (figure 4.20a). Because of the bends of a non-triangular attractor, there might be hardly any gap between the arm fragments, especially on the left side. In order to determine a search window that properly detects the width of the attractor arm, the length of the initial window is again set to 10% of length a, where 25% of the interval is left of the center and 75% is right of the center, which proved to be suitable for the given data set (figure 4.20b). The width of the attractor is now determined by a combination of two methods. The first method focuses on the detection of large density differences and the second method uses triangular interpolation similar to the Triangular Interpolation of the NN Interval Histogram (TINN) [41].

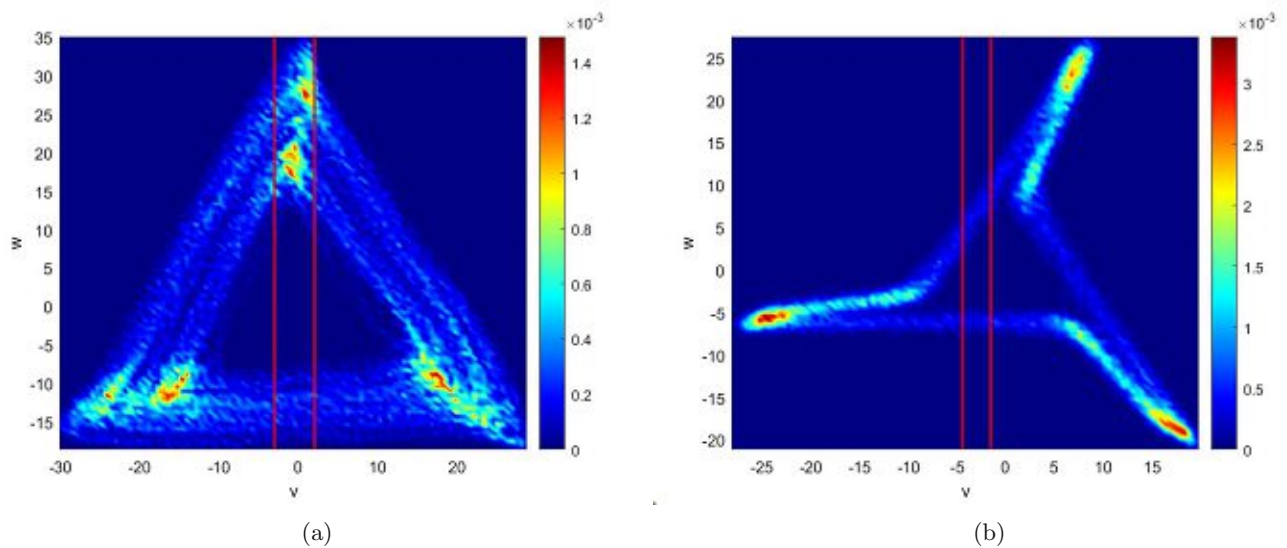<center>(a)   (b)</center>

Figure 4.20.: Different search areas to determine the width of the attractor arm: (a) Triangular attractor with placed search window, (b) bent attractor with placed search window.

1st Method:

Looking at the images in figure 4.20, one might notice the density differences within the search window. The following algorithm, which is depicted in figure 4.21, determines the largest differences and thereby returns the position of the upper and lower limit of the attractor band.
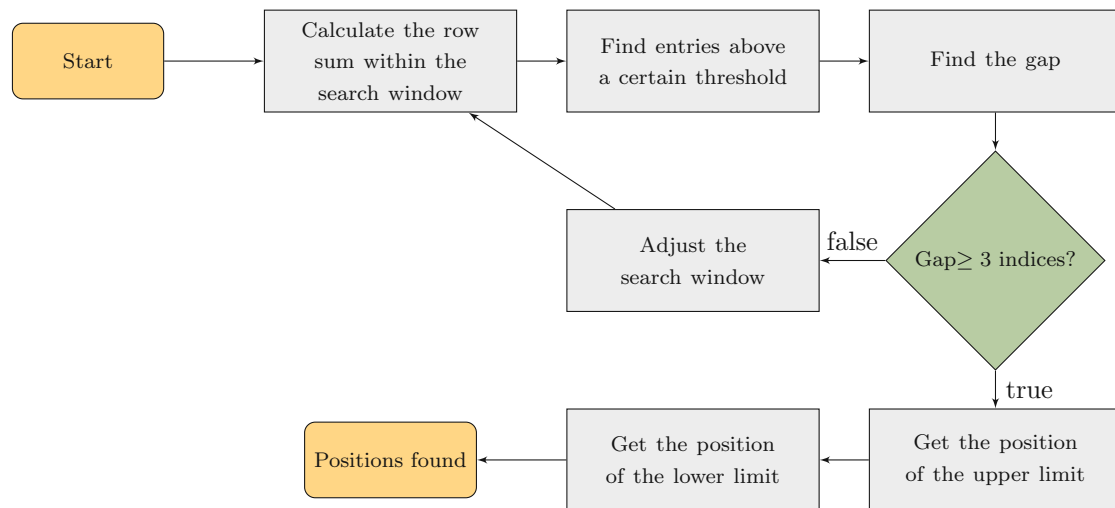

Figure 4.21.: Flowchart representation of the 1. Method to calculate the attractor width.

It is described in the following:

- Calculate the row sum vector of the density matrix within the search area.

- Find all entries and their positions that are greater than or equal to the empirically chosen 1% of their maximum value. Ideally, there should be a gap between the entries marking the beginning, and those marking the ending of an attractor arm.

- Calculate the index differences of the above determined entries and highlight those presenting a significant gap. In this study, a gap of at least 3 indices proved to be suitable.

- If no gap of at least 3 indices is found, the search window might be too far to the left. Shift the window one index to the right and repeat the process.

- The position of the upper limit of the attractor arm is marked by the end of the gap.

- The position of the lower limit of the attractor arm is marked by the position of the last entry of the row sum vector.

This method usually quite well determines the location of the upper and lower limits of the attractor band. However, in some cases, for example if a lot of outliers are detected, it is recommended to apply a second method.

2nd Method

This method uses the ideas introduced in [17, 41] and calculates the upper and lower limit of the attractor arm by fitting a triangle to the density function in a least square sense. Figure 4.22 illustrates the triangular interpolation, where A denotes the lower limit and B denotes the upper limit of the attractor band. $D(i)$ represents the values of the row sum vector of the density matrix limited to the search window. To ensure that just the lower edge of the attractor is considered, the method only focuses on the lower 40% of the attractor, which was again empirically chosen. To calculate the edges of the triangle, a piecewise linear function $t(w)$ is used:

$$
t(w) = \begin{cases} 0, & w \leq A, \\ t_1, & A \leq w \leq D_{max}, \\ t_2, & D_{max} \leq w \leq B, \\ 0, & B \leq w \leq L. \end{cases}
$$

Here D_{max} denotes the position of the highest density value and L marks the limit of the lower 40% of the attractor. To determine the values A and B, the integral over the squared differences $(D(w) - t(w))^2$ has to reach its minimum, i.e.

$$
\int_{-\infty}^{L} (D(w) - t(w))^2 dw \rightarrow 0.
$$

It should be noted that this method might not achieve sufficient accuracy, if the density difference within the attractor arm is high or, in other words, if there are only a few pulse waves that differ from the rest.
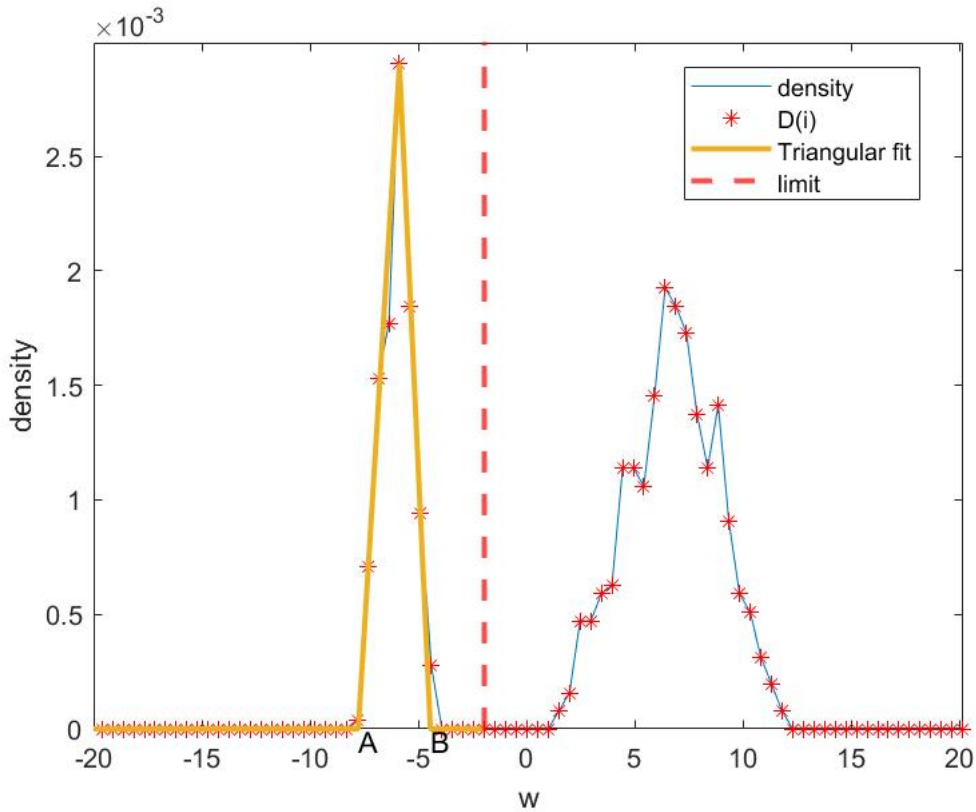
Figure 4.22.: Triangular interpolation of the density function to get the upper limit B and the lower limit A. The width of the attractor arm is defined as $B - A$.

Both methods perform with varying degree of success depending on the given data. In order to ensure a strict calculation of the width of the attractor arm, a combination of the two methods is applied (figure 4.23). As a general rule, the highest upper boundary and the lowest lower boundary are used with a few exceptions:

- If the upper limit of the first method is higher than $B + 1.5 \cdot (B - A)$, where B and A denote the upper and lower boundaries of the second method respectively, use B as the upper limit. This constraint ensures that remaining outliers located in the middle of the attractor do not distort the upper boundary.

- Sometimes the second method determines boundaries too generously. In order to guarantee an upper limit that properly marks the beginning of the lower attractor arm, use the following constraint: If B is higher than the upper limit of the first method but there are no attractor lines between those two values within the search window, use the upper boundary of the first method.

- If the lower limit is lower than $A - 0.8 \cdot (B - A)$, use A as the lower boundary. Again, this constraint ensures that possible outliers have no impact on the lower limit.

- If A is lower than the lower limit of the first method but there are no attractor lines between those two values within the search window, use the lower boundary of the first method to guarantee that the attractor arm is as narrow as possible.

After determining the upper and lower limit, the width wd of the attractor arm is defined as

$$wd = \text{upper\_limit} - \text{lower\_limit}.$$

Due to the 3-fold rotational symmetry of the attractor, the procedure can be repeated after rotating the attractor by 120 and 240 degrees.
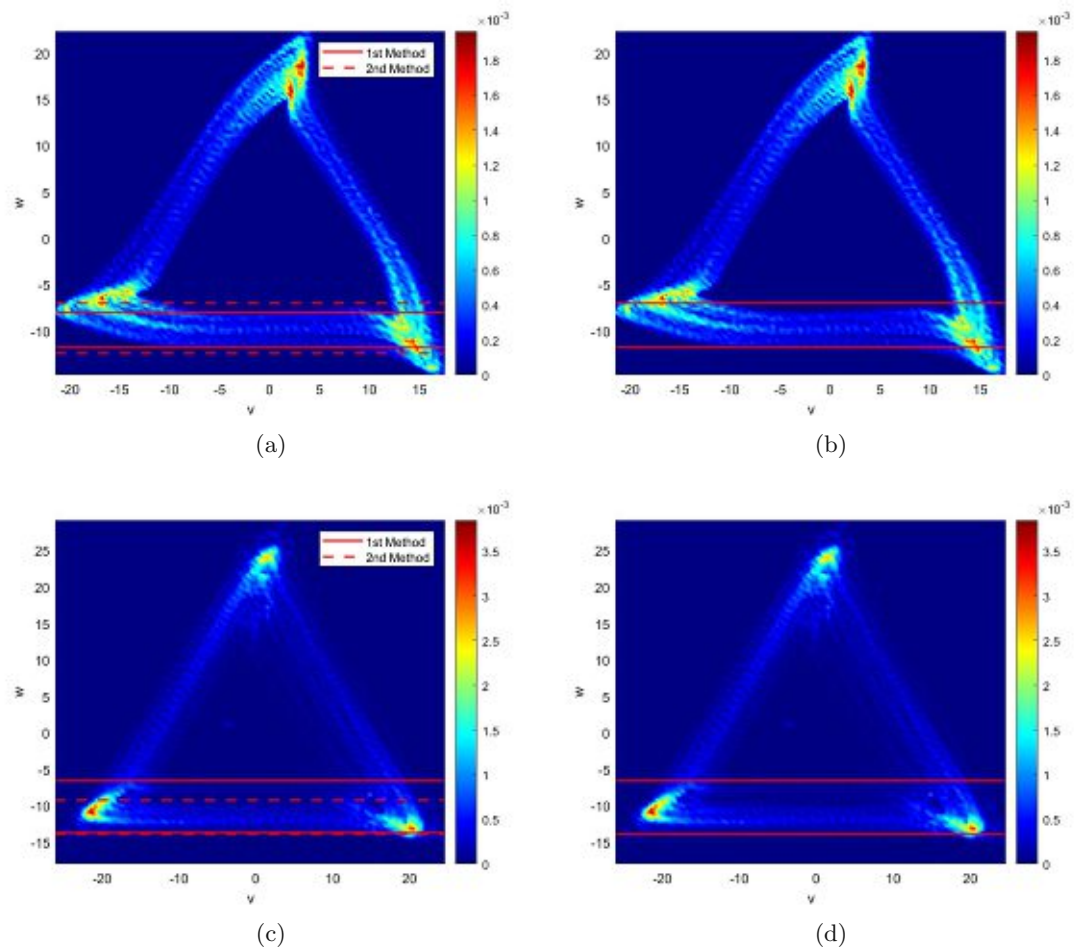

(a)

(b)

(c)

(d)

Figure 4.23.: Width of the attractor arm: (a),(c) Upper and lower limits calculated by both methods; (b),(d) combination of the two methods.

4.4.5. Summary of the Parameters

Before presenting the results in section 5, table 4.1 summarizes the calculated parameters used in this thesis.

Parameters (Unit)	Description
θ (degrees)	Angle of rotation
τ (indices)	Time delay; $\frac{1}{3}$ of the average heart rate
β (degrees)	Angle between attractor arm fragments $\rightarrow$ shape of the attractor
a (a.u.)	Length of a triangular attractor; length of one fragment of an arm of a bent attractor
b (a.u.)	Length of one fragment of an arm of a bent attractor
$\frac{b}{a}$ (a.u.)	Ratio between the two attractor arm fragments
h (a.u.)	Height of the attractor
wd (a.u.)	Width of the attractor
$\frac{wd}{h}$ (a.u.)	Ratio between width and height of the attractor
m (a.u.)	Maximum value of the density matrix

Table 4.1.: Overview of the determined parameters. Except θ, τ and m all measures are parameter vectors with 3 entries.

5. Results

This chapter is divided into two parts. In section 5.1, the feature extraction technique is evaluated based on a visual examination of the quantified attractors. Section 5.2 addresses the evaluation of the data sets and represents the results as boxplots and plots over time.

5.1. Feature Extraction

In order to analyse the algorithm, 90 attractors, i.e. three for each subject (one at baseline, one at the end of guided breathing and one at the end of the cooling down phase), were generated, quantified and the extracted features were saved. On average, about 1.4 sections containing outliers had to be replaced in each signal during preprocessing. The first visually examined measure was the angle of rotation θ of each attractor. The magnitude of the rotations of the attractors revealed a high accuracy. Figure 5.1 (a)–(c) and figure 5.2 (a)–(c) illustrate examples of correct rotations of a triangular and bent attractor, respectively. Remaining outliers had a negative impact on two of the 90 attractors and on the edge and line detection, as depicted in figure 5.3 (a)–(c). Due to the rather chaotic behaviour of these attractors, the lower edge could not be detected properly which led to a wrong calculation of θ.

The correct angle of rotation is important for further calculations, like the angle between the attractor arm fragments and the lengths and the widths of the arms. 14 attractors were characterized as triangles and lengths and widths of the attractor arms were determined accurately, as visualized in figure 5.1 (d)–(e). Most of the bent attractors were correctly measured as well, as depicted in figure 5.2 (d)–(e). However, in 4 cases, especially when a lot of outliers occurred and a wrong angle of rotation was chosen, the angle between the attractor arm fragments β and, consequently, the lengths and widths of the arms, were determined incorrectly, as seen in figure 5.3 (d)–(e).

Furthermore, three attractors tended to be divided into two parts: a small attractor with a high density and a larger attractor consisting of only a few lines (see figure 5.4). This phenomenon occurs when the amplitude of a signal rapidly increases and is thought to be caused by varying pressure of the finger on the used recording device. Even though some features of the two separated attractors, like the angle of rotation and the angle between the arm fragments, seemed to be similar, other extracted measures, like the length of the attractor arms (figure 5.4d) or the width of the arm (figure 5.4e), differed a lot. The lengths and heights of the attractor referred to the larger attractor, whereas the arm widths were extracted from the smaller one with higher density.

44

Additionally, some attractors differed in shape and had overlapping sides, especially one data set generated attractors with distinct loops (see figure 5.5). The applied algorithm did not work satisfactorily on these attractors. The overlapping arms distorted the angle of rotation (figure 5.5 (a)–(c)) and determined an inaccurate angle between the arm fragments (figure 5.5d). The looped attractor arms posed difficulties in calculation of their widths. The method mentioned in 4.4.4 uses the gap in the middle of the attractor to determine the arm width, which was missing in this depicted case and led to a much broader arm width, as seen in figure 5.5e.

(a)   (b)   (c)
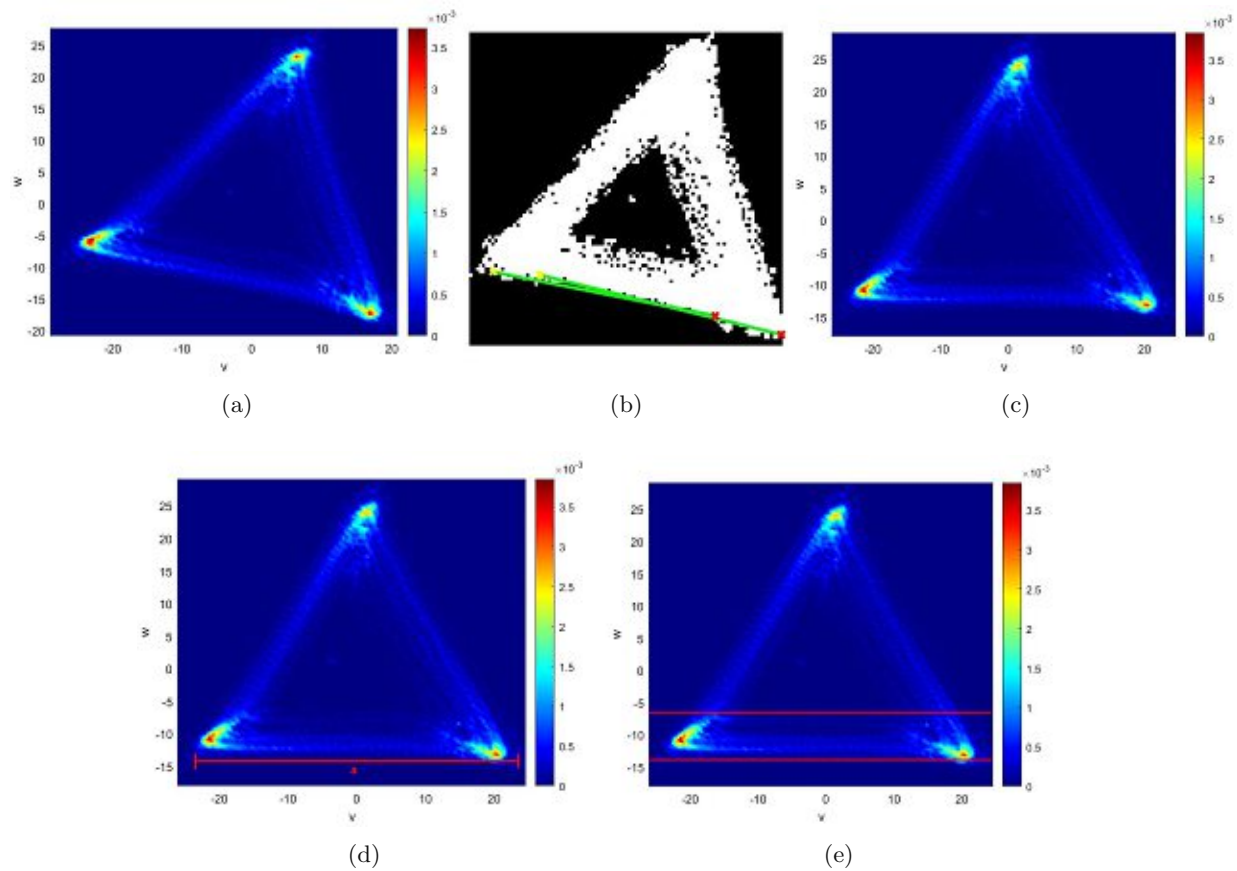
(d)   (e)

Figure 5.1.: Exemplaric triangular attractor with correctly extracted features: (a)–(c) Rotation of the attractor, (d) length of the attractor arm, (e) width of the attractor band.
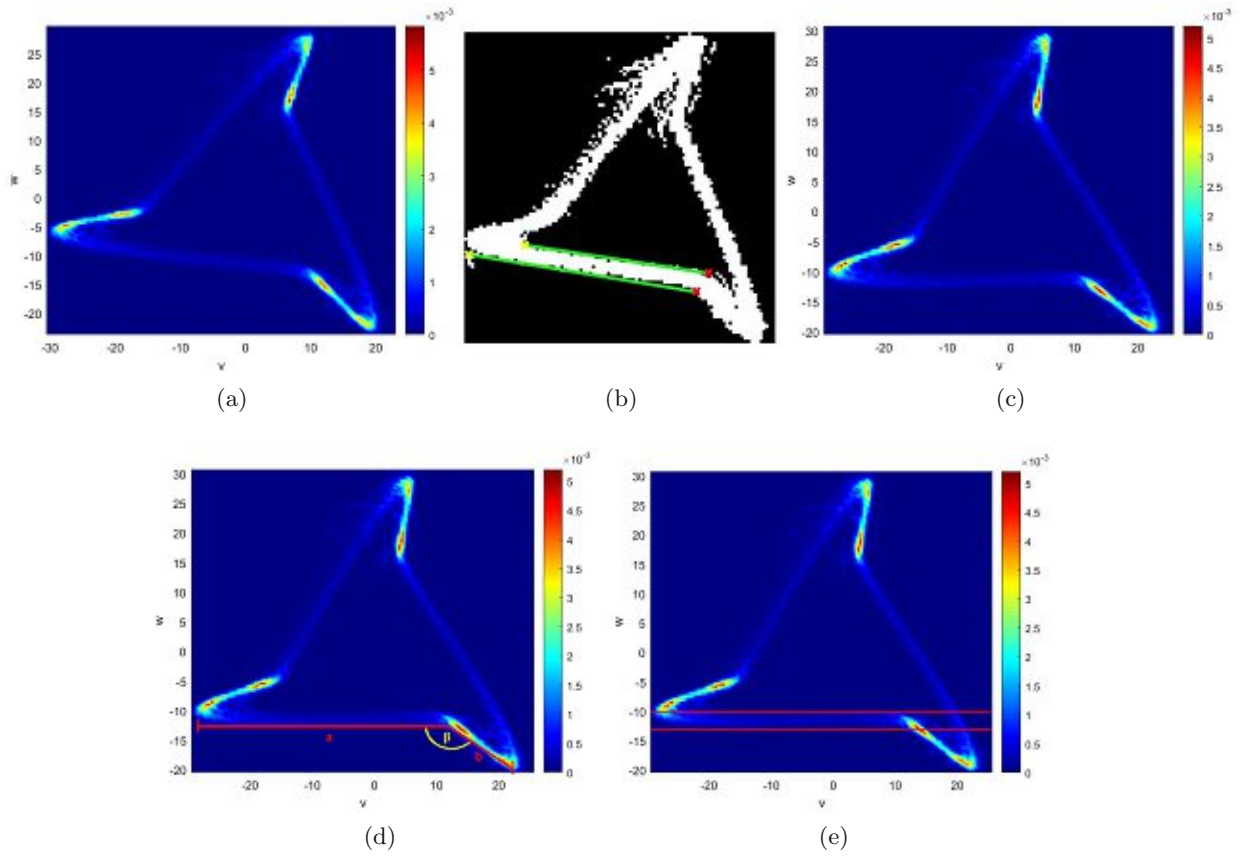
Figure 5.2.: Exemplaric bent attractor with correctly extracted features: (a)–(c) Rotation of the attractor, (d) lengths of the attractor arm, (e) width of the attractor band.
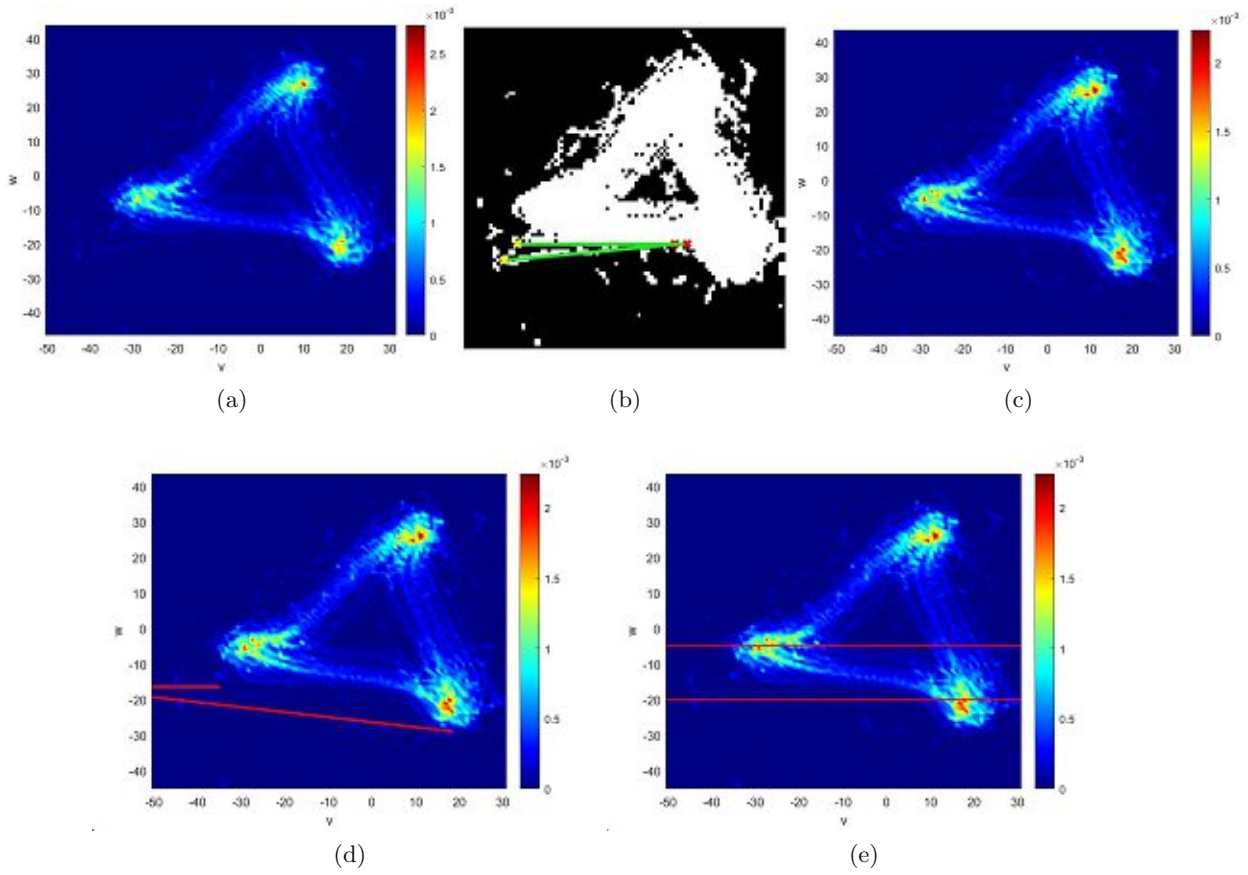
Figure 5.3.: Attractor with a lot of outliers that distort the quantification: (a)–(c) Incorrect determination of the angle of rotation because of the chaotic behaviour of the attractor, (d) incorrect extraction of the attractor arm lengths represented in red, (e) incorrect determination of the attractor band width.
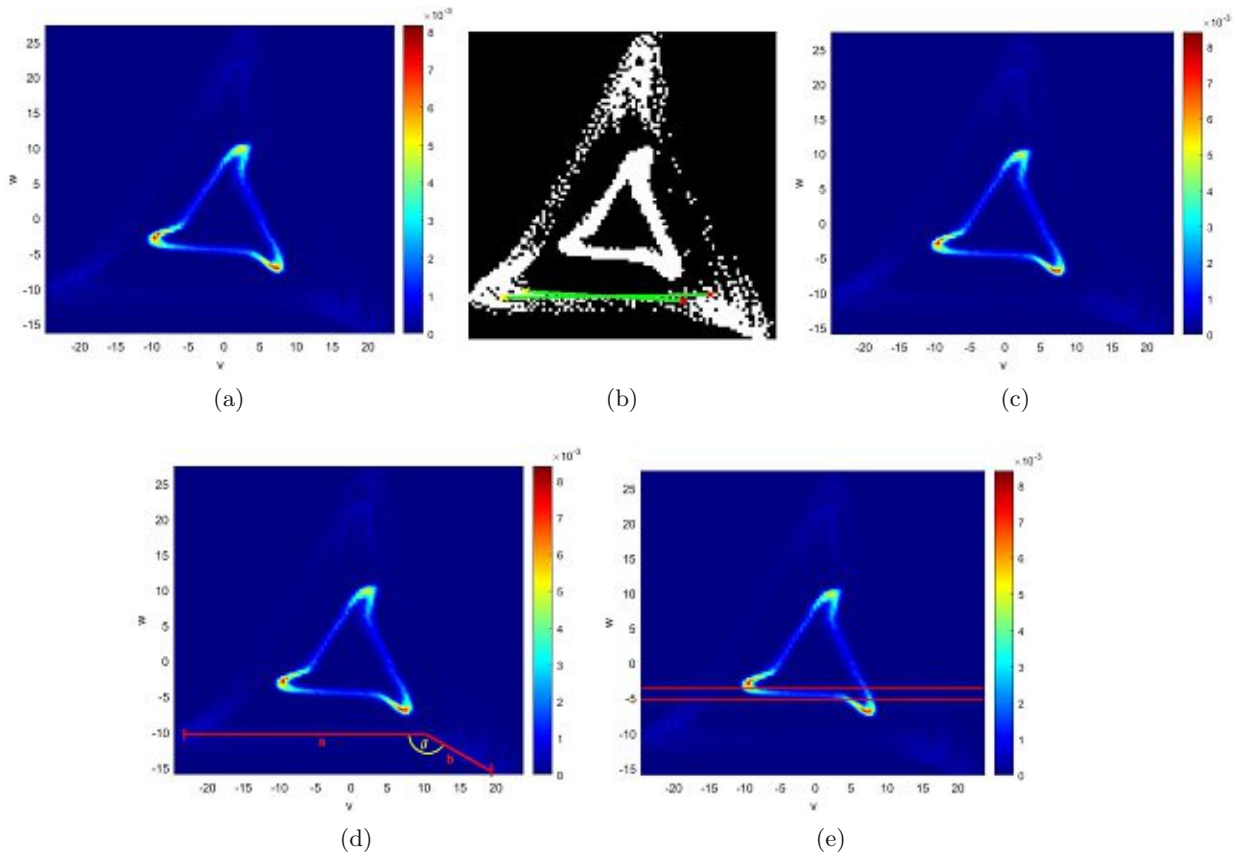
47

Figure 5.4.: Attractor consisting of a small attractor with high density and a large attractor with low density: (a)–(c) Rotation of the attractor, (d) determination of the attractor arm lengths. The applied algorithm focuses on the larger part of the attractor. (e) Calculation of the band width with a focus on the smaller part of the attractor with higher density.

(a)   (b)   (c)
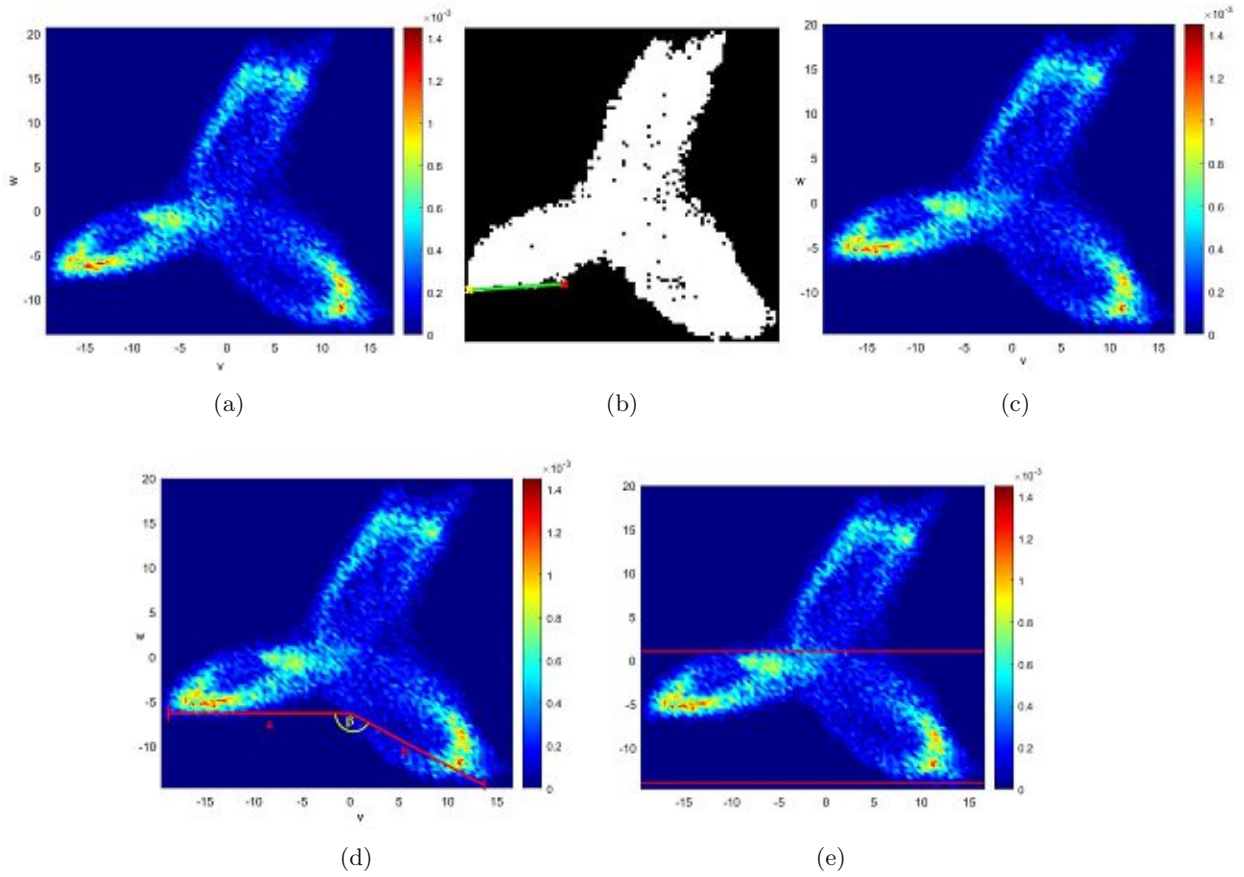
(d)   (e)

Figure 5.5.: Attractor with overlapping sides. This looped attractor cannot be quantified correctly by the applied algorithm: (a)–(c) Incorrect rotation of the attractor, (d) inaccurate extraction of the angle between the attractor arms and the lengths of the attractor, (e) incorrect determination of the attractor band width.

5.2. Development over Time

This section presents the results of the feature extraction method applied to the given data set as explained in section 3.2. Table 5.1 and the boxplots focus on the evaluation of the three subsets and their differences assessed by the corrected p-values resulting from the Bonferroni post-hoc test. The other plots represent the changes of the attractor features over time.

5.2.1. Evolution of the Heart Rate

The time delay τ is not an attractor feature per se, but plays an important role in the construction of the attractor. As stated in section 2.4, τ is directly correlated to the average heart rate hr. The conversion from indices to beats per minute (bpm) yields two mirrored graphs as depicted in figure 5.6. During the guided exercise the average heart rate increases from 67.22 (SD 9.17) to a maximum of 70.42 (SD 10.87) beats per minute and decreases slightly to 69.97 (SD 10.61) beats per minute at the end of the guided breathing. In the last 5 minutes of the recording, during the cooling phase, the average heart rate decreases to 69.25 (SD 10.22) beats per minute. The analysis using a Friedman test, which compared the three time frames, revealed overall significant changes ($p = 0.001$). Post-hoc testing supported the theory by detecting a significant increase during guided breathing ($p = 0.002$). However, the change in heart rate between the end of the guided breathing and the cooling down phase proved to be non significant. The corresponding boxplot is depicted in figure 5.7.

5.2.2. Evolution of the Angles

Figure 5.8 shows the average evolution of the angle of rotation θ and the angle between the attractor arm fragments β. As stated in section 4.4.2, β is a vector with three entries which correspond to rotations by 0, 120 and 240 degrees, respectively. Due to the 3-fold rotational symmetry of the attractors, all three entries should have similar value. Thus, the median of these entries proved to be a suitable representative of the angle between the arms of each attractor and neglects outliers. As seen in figure 5.8, both angles fluctuate within 2–3 degrees at each time step. Because of this fluctuation, hardly any change is visible, although there seems to be a trend: the angle between the attractor arms decreases slightly during the guided breathing exercise and stays at this approximate level until the end of cooling. The application of the Friedman-Test yielded non-significance throughout the different time frames which is also illustrated in the corresponding boxplots in figure 5.9–5.10.

Parameter	Baseline	End of guidance	End of cooling	Friedman	p-value 1-2	p-value 2-3	p-value 1-3	Unit
τ	77.68 (11.56)	74.93 (12.2)	75.62 (12.06)	0.001	0.002	1.000	0.016	indices
hr	67.22 (9.17)	69.97 (10.61)	69.25 (10.22)	0.001	0.002	1.000	0.016	bpm
θ	4.05 (5.15)	4.84 (5.41)	4.16 (4.18)	0.99	-	-	-	degrees
β	152.02 (11.44)	152.34 (9.98)	151.85 (11.32)	0.89	-	-	-	degrees
$\frac{b}{a}$	0.22 (0.17)	0.23 (0.2)	0.18 (0.16)	0.33	-	-	-	AU
h	45.10 (15.74)	39.22 (16.5)	37.09 (17.82)	0.002	0.048	0.71	0.001	AU
wd	7.89 (3.23)	6.35 (3.40)	6.84 (3.85)	0.006	0.005	0.71	0.15	AU
$\frac{wd}{h}$	0.18 (0.05)	0.16 (0.06)	0.19 (0.06)	0.066	0.26	0.077	1.000	AU
m	0.0037 (0.0016)	0.0035 (0.0019)	0.0033 (0.0019)	0.04	0.88	0.45	0.038	AU
Percentage of attractors with a broader right side than the average of the two other sides								
	65.52	51.72	51.72					%

Table 5.1.: Average of extracted features across the given data sets at baseline, at the end of the guided breathing and after the cooling phase. The parameter β represents the average median value, the parameters $\frac{b}{a}, h, wd$ and $\frac{wd}{h}$ the average mean values of the three attractor sides, respectively. The data is expressed as mean (standard deviation). The column Friedman represents the p-value of the Friedman-Test, whereas the numbered corrected p-value columns contain the results of the post-hoc test, where the numbers indicates which time frames were compared. The last row represents the percentage of attractors with a broader right arm than the average of the two other sides.
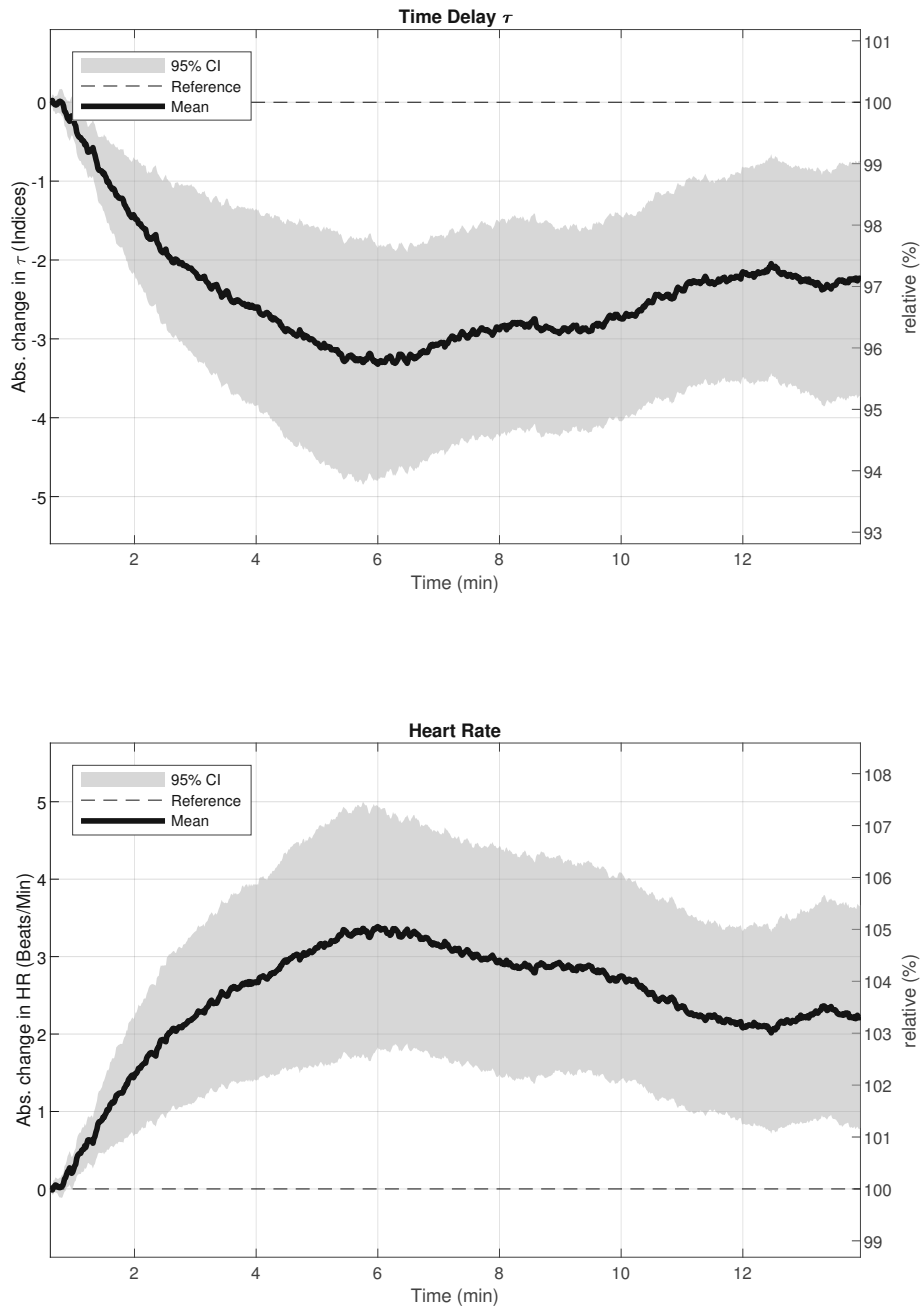
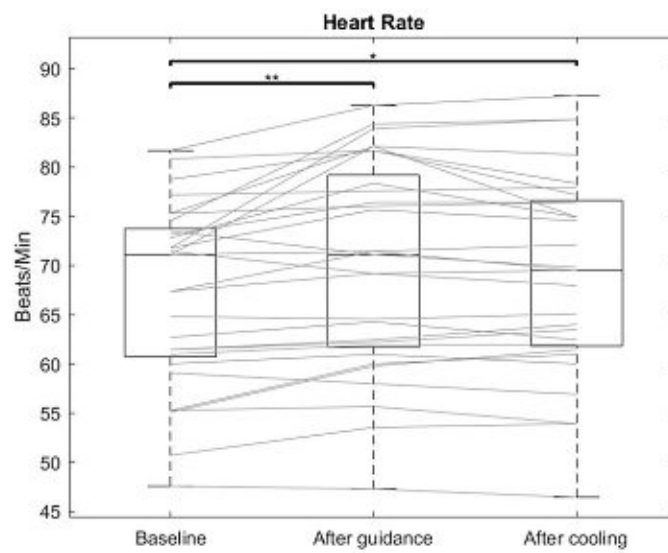Figure 5.6.: Evolution of the time delay τ and the corresponding average heart rate hr.

Figure 5.7.: Boxplot of the hr hr. The stars indicate the level of significance α, where a single star means $p \leq 0.05$ and two stars represent $p \leq 0.01$.
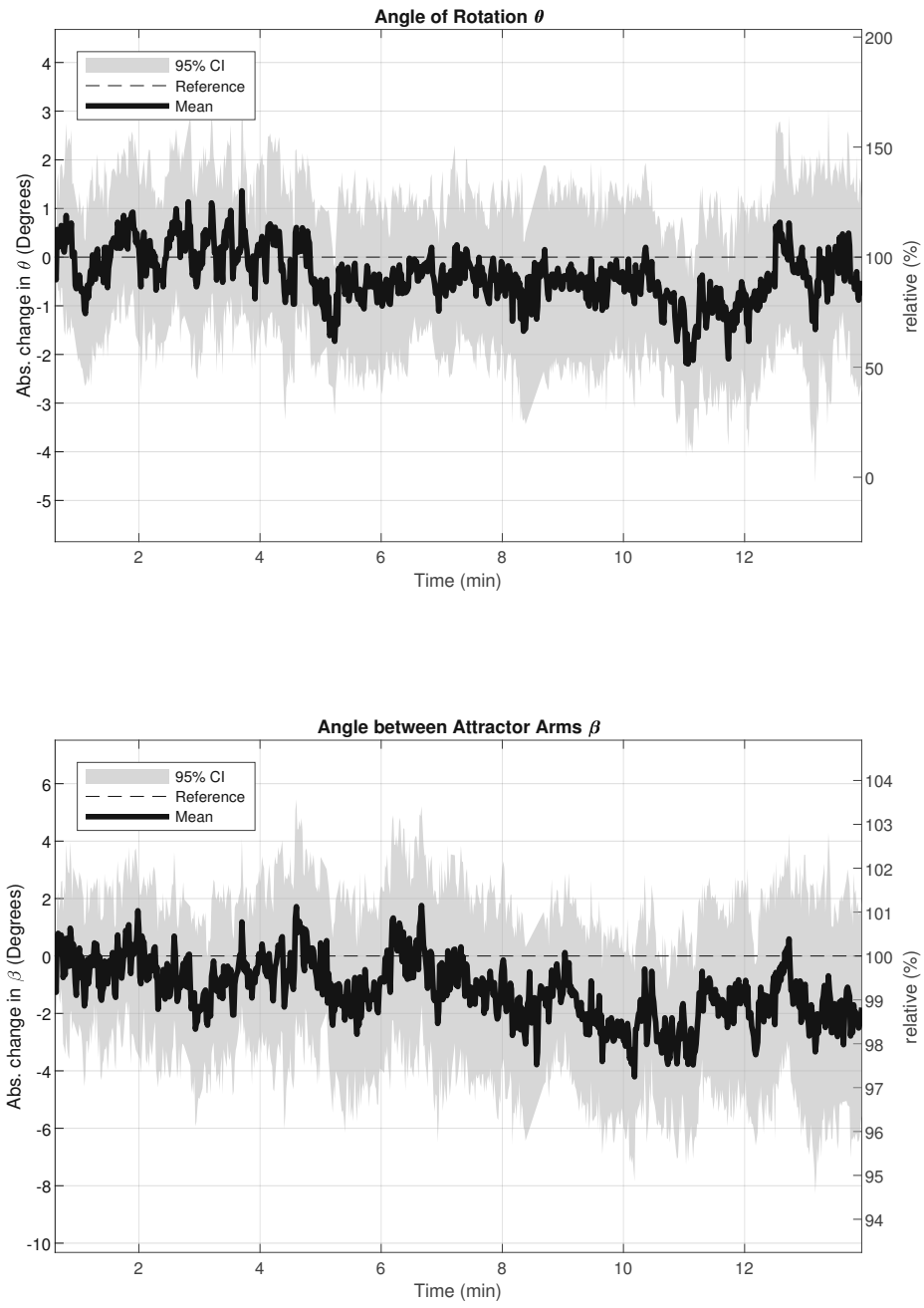
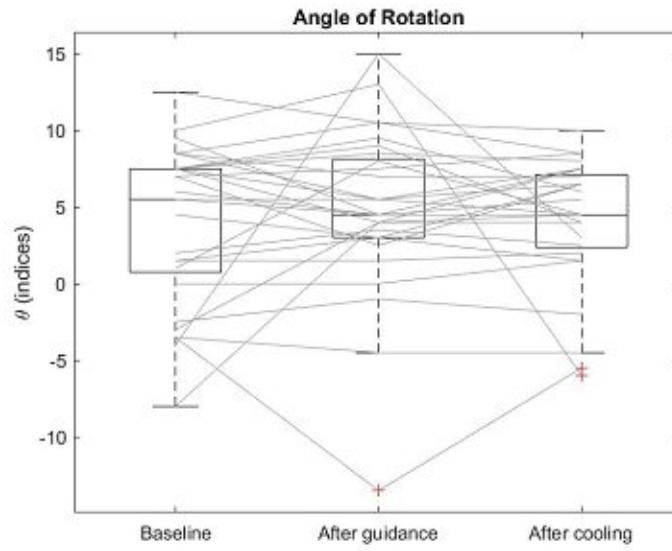Figure 5.8.: Evolution of the angle of rotation θ and the angle between the attractor arm fragments β.

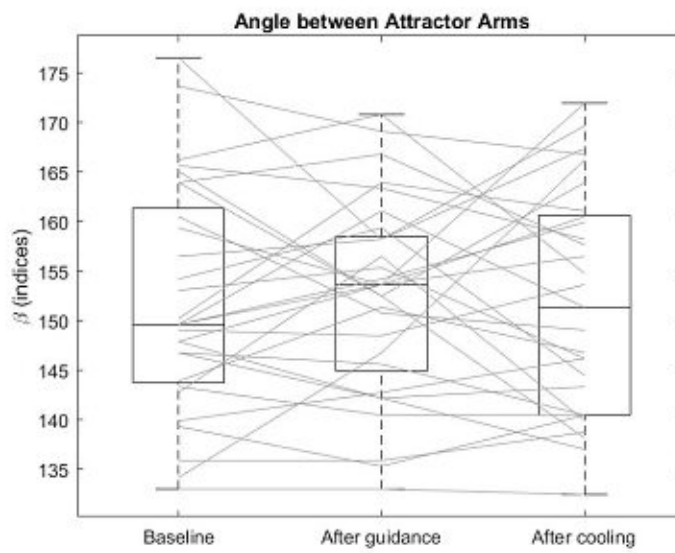Figure 5.9.: Boxplot of the angle of rotation θ.

Figure 5.10.: Boxplot of the angle between the attractor arm fragments β.

5.2.3. Evolution of Height and Width

The evolution of the average height h and average width wd of the attractors is depicted in figure 5.11. After a small increase in the first minute, the average height of the attractors drops during the guided exercise from 45.1 (SD 15.74) AU to 39.22 (SD 16.5) AU and decreases further in the cooling phase to 37.09 (SD 17.82) AU. The Friedman test compared these three time frames and manifested overall significant changes ($p = 0.002$). The post-hoc pairwise comparison revealed a significant drop during the guided breathing phase ($p = 0.048$), as well as between the baseline and the end of cooling phase ($p = 0.001$). In the last 5 minutes, however, the average height of the attractors decreases non-significantly. Even though the average width of the attractors has a higher fluctuation than the average height of the attractors, it also decreases during the first 10 minutes from 7.89 (SD 3.23) AU to 6.35 (SD 3.4) AU. During the unguided cooling phase, the average width increases to 6.84 (SD 3.85) AU. Once again, Friedman test showed a significant difference between the three time frames. The post-hoc test revealed a significant change between the baseline and the end of guided breathing ($p = 0.005$) but showed that the average width increases non significantly in the last 5 minute during cooling down. The corresponding boxplots are shown in figure 5.12–5.13.

5.2.4. Evolution of the Ratios

Figure 5.14 illustrates the evolution of the average ratio of the attractor arm fragments $\frac{b}{a}$ and the average ratio of width to height $\frac{wd}{h}$. The ratio $\frac{b}{a}$ displays a high fluctuation at each time step, however, Friedman test shows that the differences across the three time frames are non-significant. Figure 5.15 illustrates the corresponding boxplot. The average ratio $\frac{wd}{h}$ fluctuates during the guided breathing phase but slightly decreases from 0.18 (SD 0.05) AU to 0.16 (SD 0.06) AU. In the last 5 minutes on the other hand, the ratio $\frac{wd}{h}$ increases from 0.16 (SD 0.06) AU to 0.19 (SD 0.06). Friedman test revealed a borderline significance ($p = 0.066$) and Bonferroni post-hoc test confirmed a borderline significant increase during cooling down phase ($p = 0.077$). The corresponding boxplot is shown in figure 5.16.

5.2.5. Evolution of the maximum Value of the Density Matrix

The evolution of the maximum value of the density matrix is depicted in figure 5.17. During the 15 minutes of recording, the maximum value fluctuates but decreases from 0.0037 (SD0.0016) AU to 0.0033 (SD 0.0019) AU. This, as maintained by Friedman test, yields a significant difference between the three time frames ($p = 0.04$). Post-hoc testing supported the theory and revealed a significant drop between baseline and the end of the cooling phase ($p = 0.038$). This is also underlined by the boxplot in figure 5.18.

5.2.6. Evolution of Variation in Cardiac Contractions

As stated in section 2.6, variability in the upstroke gradient, which is linked to variation in cardiac contractions, leads to variability in the right-hand arm of the attractor. In order to measure the changes in cardiac contractions over time, the rate of attractors with right sides broader than the average of the two other sides was calculated at each time step. Figure 5.19 illustrates the results. It can be seen that the rate fluctuates a lot which makes it hard to identify any trend. At the end of the cooling phase, the rate of attractors with a broader right side tends to decrease but this downward tendency might be too short to rule out the possibility of coincidence.

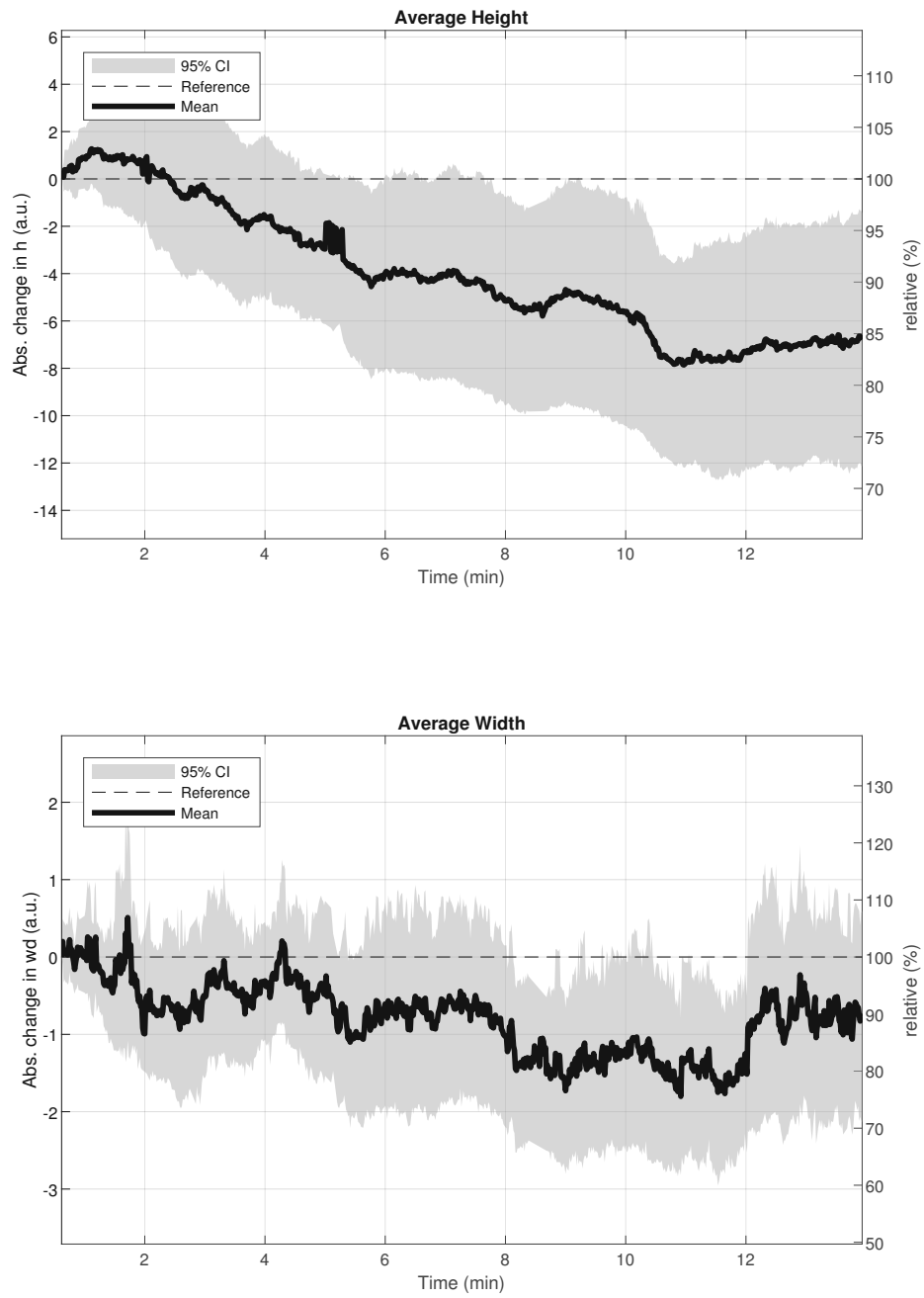The remaining plots and boxplots can be found in the appendix A.

Figure 5.11.: Evolution of the average height h and average width wd of the attractor.
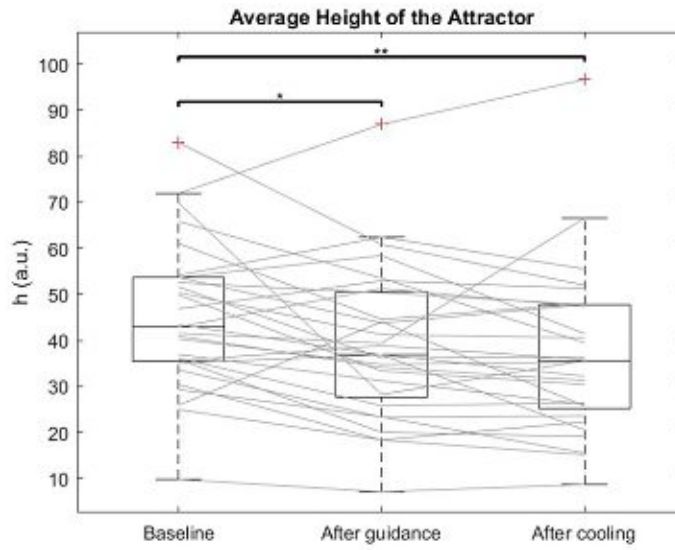
Figure 5.12.: Boxplot of the average height h of the attractor. The stars indicate the level of significance α, where a single star means $p \leq 0.05$ and two stars mean $p \leq 0.01$.
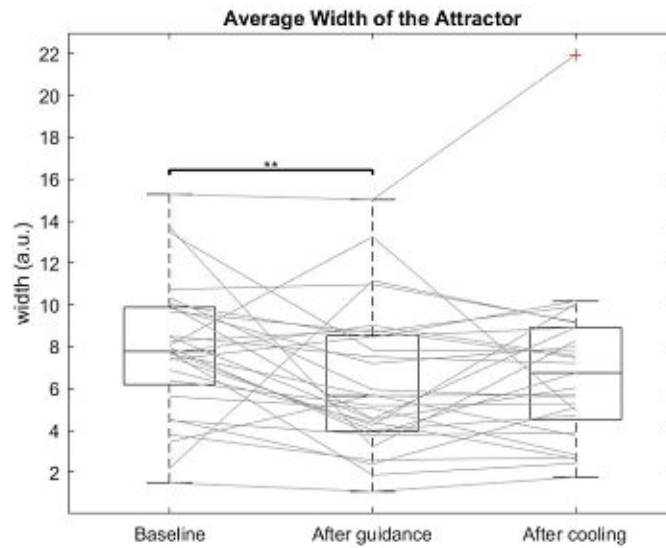

Figure 5.13.: Boxplot of the average width wd of the attractor. The stars indicate the level of significance α, where two stars mean $p \leq 0.01$.
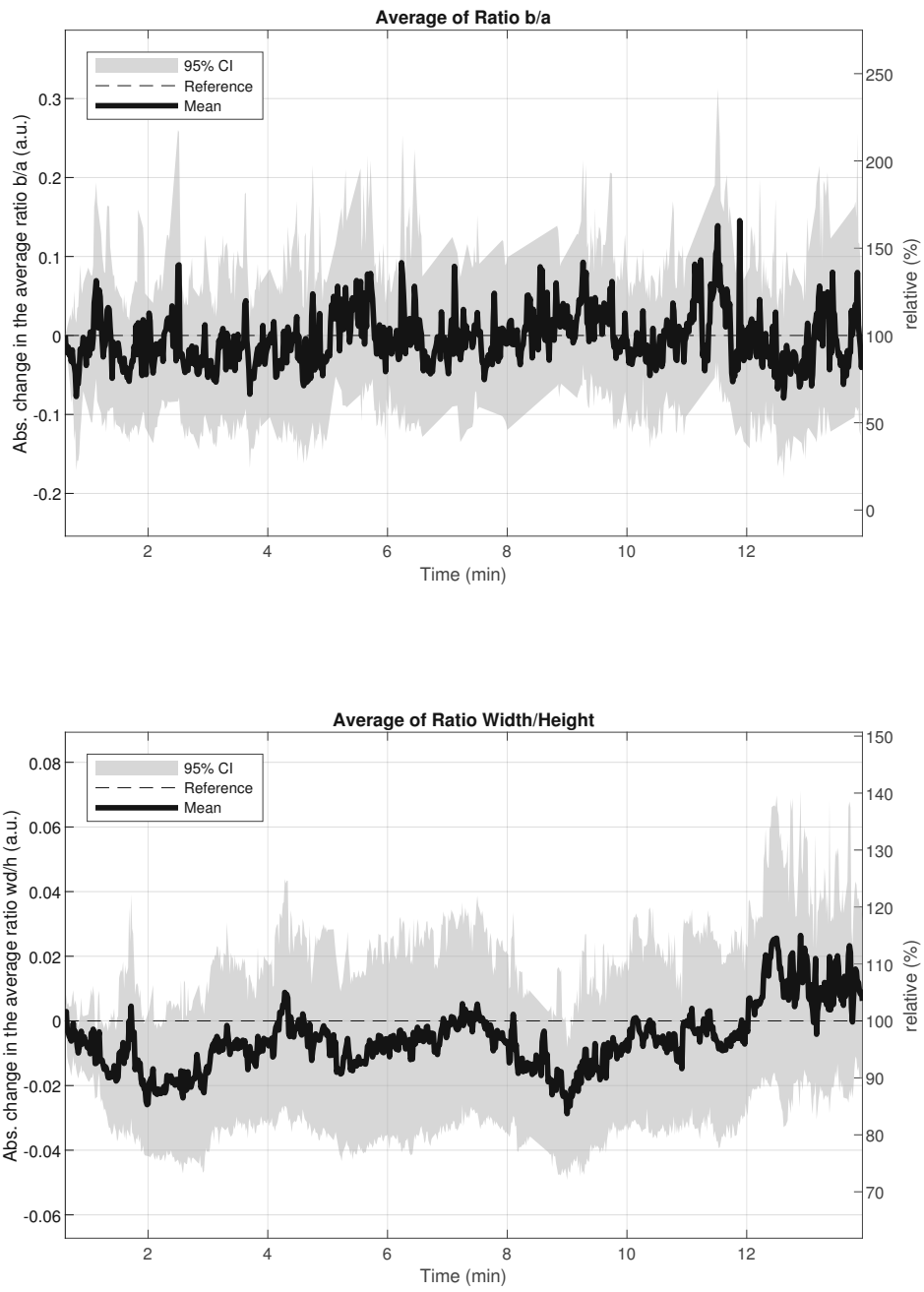
59

Figure 5.14.: Evolution of the average ratio of the two attractor fragments $\frac{b}{a}$ and the average ratio of width to height $\frac{wd}{h}$.
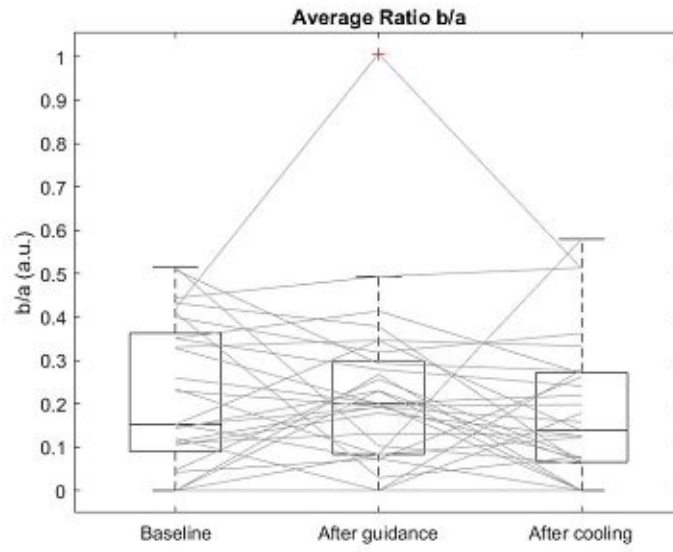
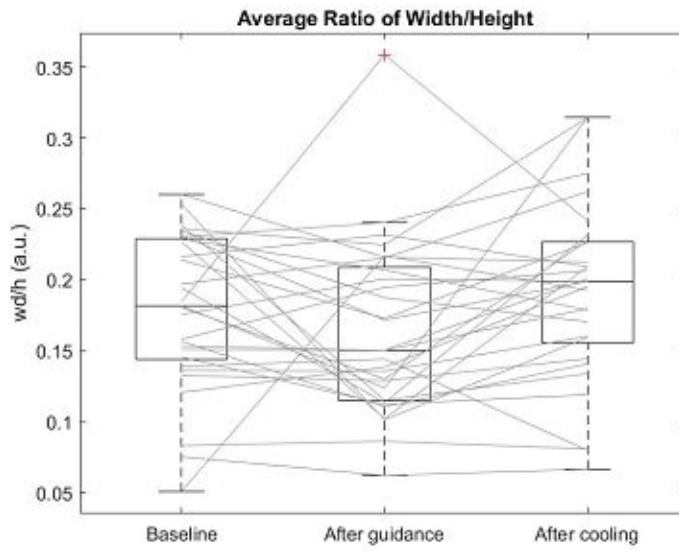Figure 5.15.: Boxplot of the average ratio $\frac{b}{a}$.

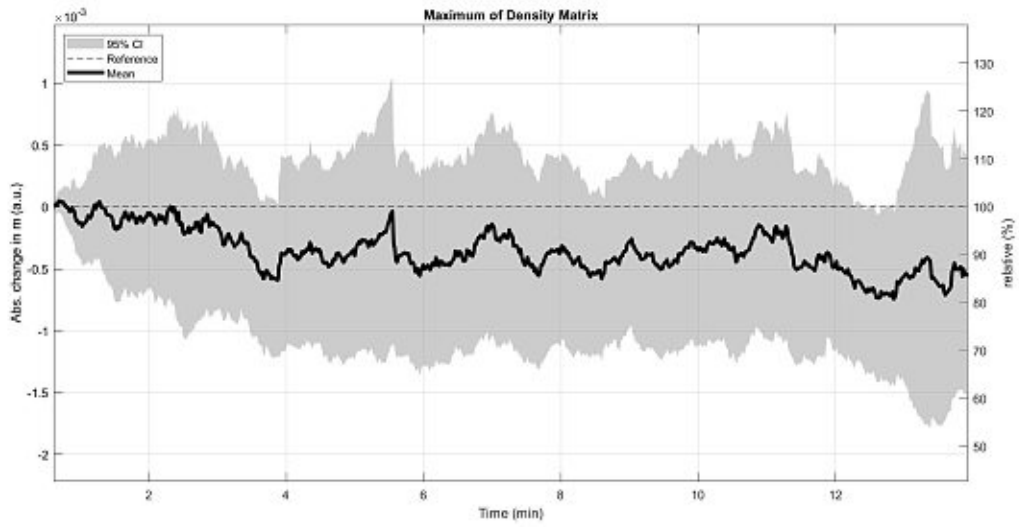Figure 5.16.: Boxplot of the average ratio $\frac{wd}{h}$.

Figure 5.17.: Evolution of the maximum value m of the density matrix.
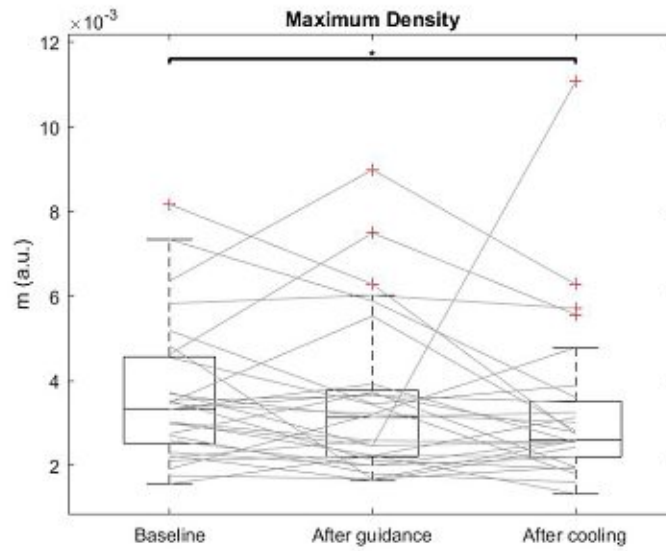

Figure 5.18.: Boxplot of m. The star indicates the level of significance α, where a single star means $p \leq 0.05$.
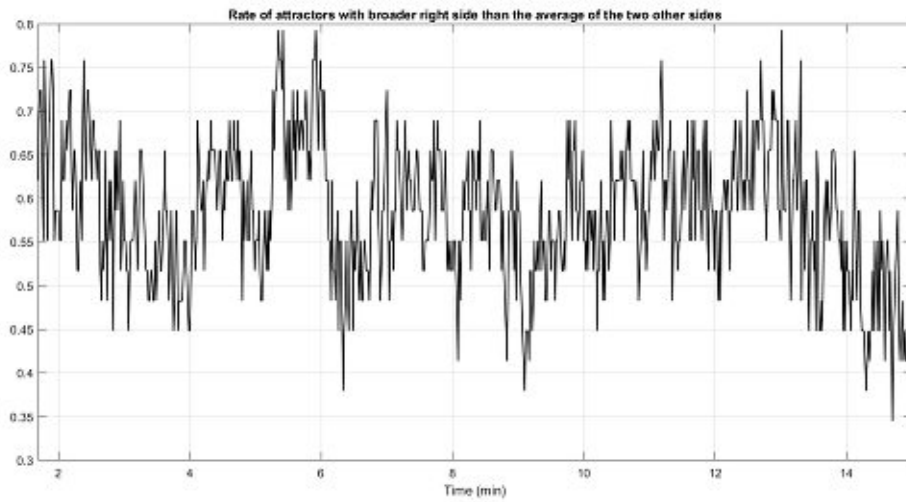
Figure 5.19.: Evolution of rate of attractors with a right side broader than the average of the two other sides.

6. Discussion

In this thesis, a new method to quantify arterial pulse waveform morphology and its evolution over time was implemented. The main task was to develop an algorithm that extracts features from the reconstructed attractors. This chapter focuses on the interpretation of the extracted attractor features and discusses the results of the breathing exercise provided in chapter 5. Finally, some limitations of the thesis are addressed.

6.1. Attractor Features

Accuracy and occurring issues of the implemented feature extraction technique were already discussed in section 5.1. Hence, only a short summary of the most important results is provided in this section and the main focus lies on the interpretation of the extracted parameters and their correlation to pulse waveform features.

The quality of the given data set is crucial for proper quantification of the corresponding attractor. The combination of the preprocessing method explained in section 4.1 together with median filtering of the density image assured the best results. Nevertheless, metrological effects, like varying pressure on the recording device, could not be detected by the preprocessing method or the median filter. The resulting rapid increase in the signal's amplitude led to an attractor divided into two parts which could not be quantified satisfactorily.

A magnitude of the visually examined attractors revealed high rotational accuracy. However, in some cases, especially when a lot of outliers occurred, the image processing technique did not work precisely enough resulting in a wrong angle of rotation. Further calculations of attractor measurements, like the angle between the attractor fragments or the length and width of the attractor arms, were heavily dependent on the exact angle of rotation; thus, the preciser the rotation of the attractor, the more accurate further calculations of attractor features.

The average heart rate hr and, consequently, the time delay τ were the first crucial parameters determined. As stated in section 2.6, changes in heart rate have hardly any influence on the generated attractor and are therefore not quantifiable in the density plot of the trajectory. Nevertheless, a correct determination of the average cycle length in a selected time window is necessary to generate an appropriate attractor that has 3-fold rotational symmetry. Although other methods to find the average heart rate are mentioned in literature [5, 14, 22], autocorrelation proved to be successful and less complex in this context. In addition, when compared to

Bachler et al. [6], who used the same data set but another way to calculate the average heart rate, results were similar.

As already mentioned in section 2.6, changes of the average height of the attractor reflect the increase or decrease in pulse pressure. However, contrary to piecewise linear signals discussed in Aston et al. [5], the height of attractors generated by more complex signals, i.e. signals with curvature changes, cannot be linked to absolute pulse pressure values.

Additionally, the variability of the waveform can be measured by the average width of the attractor arms. In order to draw an appropriate comparison between two different attractors, the average width of each attractor has to be in relation to the average size. Thus, the ratio width to height $\frac{wd}{h}$ was determined, which ranges between 0 and 1. The higher the calculated value, the broader the sides of the considered attractor and the higher the variability in the pulse waveform.

As stated in section 2.6, Aston et al. [5] and Nandi et al. [29] claimed that the curvature of the downstroke of a pulse wave correlated with the rotation of an attractor; more precisely, they stated that a concave downstroke led to a clockwise rotation. When applied to human pulse wave data, acquired through photoplethysmography at the fingertip, with more complex behaviour, i.e. more curvature changes, this trend was also seen. However, other factors influence the shape and orientation of the attractor as well. In this thesis, the attractors were categorized into two different shapes: a triangular attractor and an attractor with bends, depending on the calculated angels β between the attractor arms. Studies of the pulse waveform data have shown that an attractor is most likely to be categorized as triangular, if the curvature of the downstroke is rather simple, i.e. hardly any changes with no dicrotic wave visible, and the ratio of the crest time to the time delay τ is 1 or close to 1. Figure 6.1a illustrates an artificial signal with linear upstroke, concave downstroke and $\frac{\text{crest time}}{\tau} = 1$. Figure 6.1b shows the corresponding triangular attractor on the (v, w) plane. Attractors with bent sides, on the other hand, may result from different reasons. One major factor of influence is again the ratio of crest time to τ. Tests of different pulse waveform signals (data not shown) have proven that the arms of the attractor tend to bend, if $\frac{\text{crest time}}{\tau} < 1$, which leads to a division of the attractor side into two fragments a and b. Furthermore, these experimental studies have shown that the smaller $\frac{\text{crest time}}{\tau}$ the higher $\frac{b}{a}$. Figure 6.1c displays an artificial pulse wave with steeper linear upstroke than in figure 6.1a, a concave downstroke and $\frac{\text{crest time}}{\tau} < 1$. The resulting attractor with bent arms is depicted in figure 6.1d.
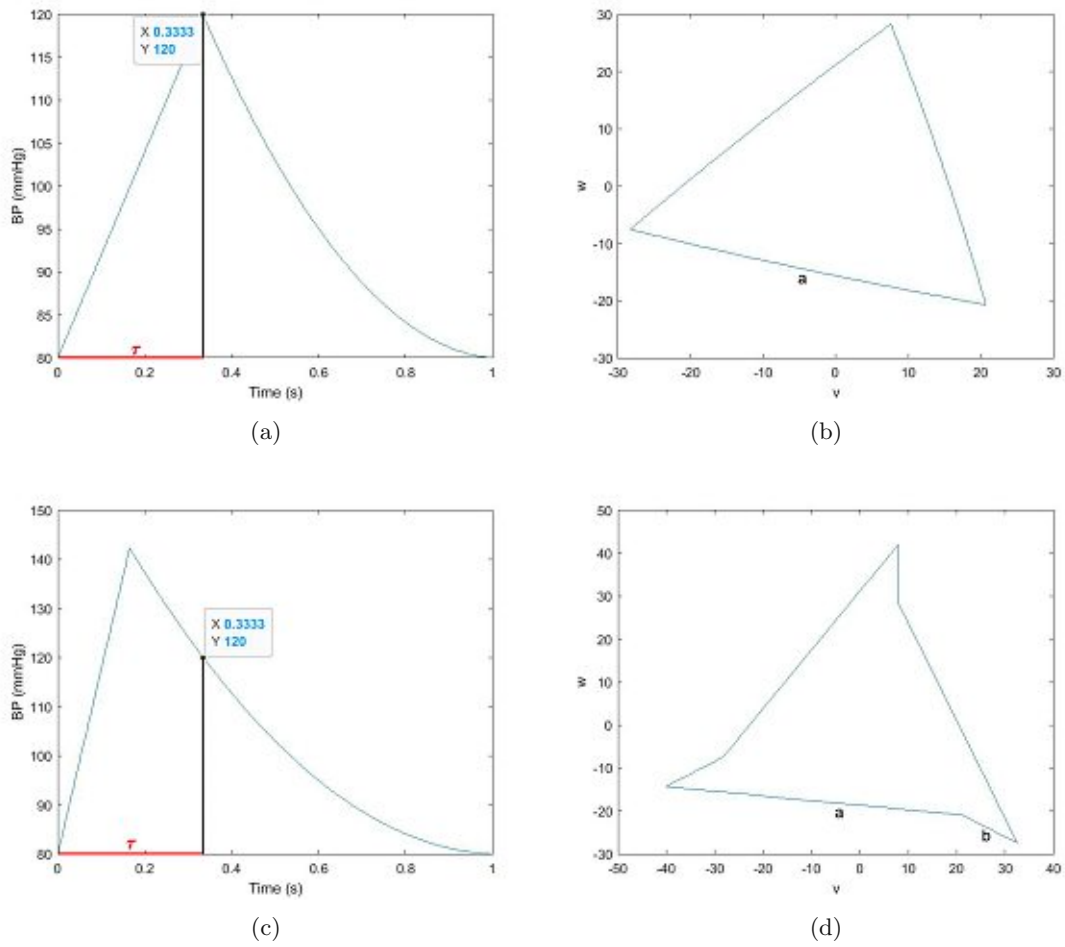
(a)

(b)

(c)

(d)

Figure 6.1.: Artificially generated signals and corresponding attractors to illustrate the influence of $\frac{\text{crest time}}{\tau}$: (a) Signal with $\frac{\text{crest time}}{\tau} = 1$, (b) triangular attractor, (c) signal with $\frac{\text{crest time}}{\tau} < 1$, (d) attractor with bends.

Signals with a more complex structure, i.e. more curvature changes caused by the presence of a dicrotic notch and the following dicrotic wave, were also examined. It was noticed that pulse waves with a visible dicrotic wave and $\frac{\text{crest time}}{\tau} < 1$ tended to be hardly rotated or even rotated in an anticlockwise direction. Figure 6.2 illustrates such a pulse wave and the corresponding trajectory with a slightly negative angle of rotation θ.

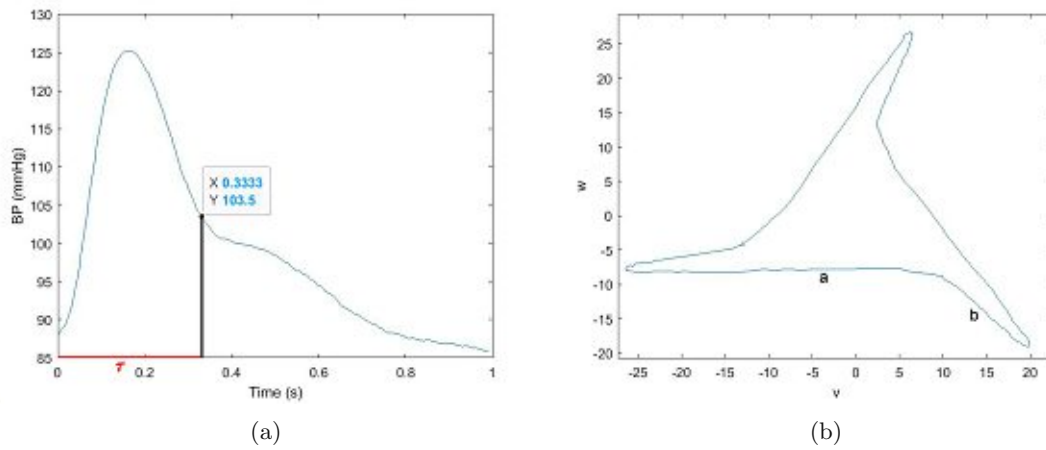(a)   (b)

Figure 6.2.: Pulse wave and corresponding attractor to illustrate the influence of curvature changes: (a) Signal with a small dicrotic wave and $\frac{\text{crest time}}{\tau} < 1$, (b) bent attractor with a slightly negativ angle of rotation θ.

Furthermore, pulse waves with a distinct dicrotic wave and $\frac{\text{crest time}}{\tau}$ close to 1 seemed to generate an attractor with overlapping sides (figure 6.3). This suggests the assumption that the position of the dicrotic notch and the dicrotic wave amplitude have an impact on the shape and orientation of the attractor. However, the specific association is beyond the scope of this thesis and needs further research.

The maximum value m of the density matrix was extracted because it was assumed to be another indicator of the variability of the waveform. A relatively high value might be a sign of a nearly periodic signal whereas a comparatively low value one of a variable signal. However, it requires further research to prove this assumption.

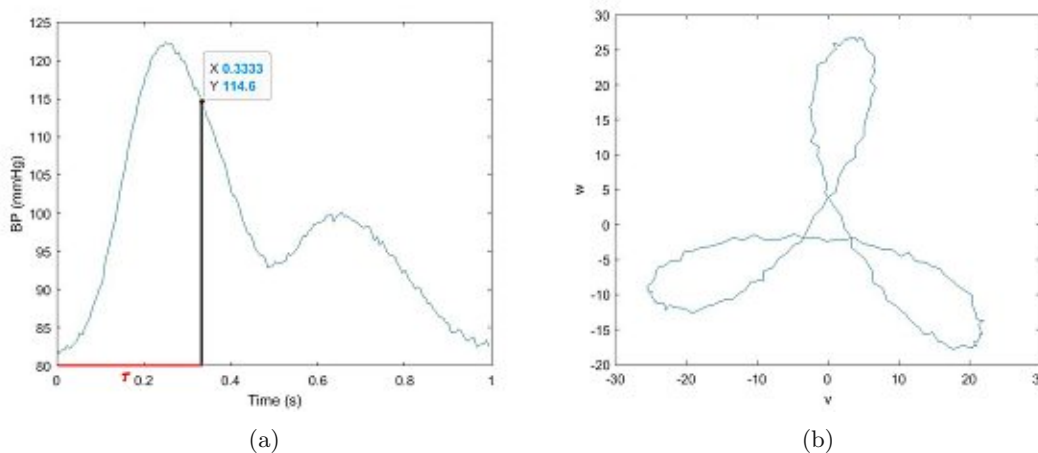(a)   (b)

Figure 6.3.: Pulse wave and corresponding attracor to illustrate the influence of curvature changes: (a) Signal with a distinct dicrotic wave and $\frac{\text{crest time}}{\tau}$ close to 1, (b) attractor with overlapping sides.

In the future, these insights might be used for assessing people's and patient's cardiovascular health status.

6.2. Breathing Exercise

A moving time window of 100 seconds was applied to the given data sets of the 30 subjects and at each time frame an attractor was generated and its features extracted. The first 100 seconds were set as baseline. Afterwards, the extracted features were plotted as functions over time as difference from their baseline values.

The first interesting result is the evolution of the average heart rate. It increases rapidly during the first 6 minutes of guided breathing and slowly declines during the last 4 minutes of guidance and during the unguided cooling phase, approaching, but not reaching, the value at baseline. It is particularly interesting that the relaxation exercise increases the average heart rate instead of lowering it and that the gradient of the heart rate reverses during the guided breathing phase. These findings also match the results stated in Bachler et al. [6].

The evolution plot of the average height of the attractors shows a significant decline during the breathing exercise, which means that this technique has a shrinking effect on the pulse pressure. Previous studies revealed that relaxation techniques could lower blood pressure [8, 9, 10, 35]. Therefore, it seems reasonable to connect the decline in pulse pressure to a decrease in blood pressure. Results from Bachler et al. [6], who used the same data set, support this assumption. The pulse arrival time (PAT) calculated in that study showed a significant increase during the breathing exercise and was linked to a decrease in mean pressure. However, no blood pressure data was recorded during the device-guided breathing study; thus, a definite statement is not possible.

The average width of the attractors also shows a descending trend during the guided breathing, followed by an increase during the unguided cooling phase. As mentioned in the previous section 6.1, the width has to bear relation to the height of the attractors. Therefore, the ratio $\frac{wd}{h}$ is considered. It fluctuates during the exercise, being slightly below the baseline value during the guided phase but indicating no definite trend. In the last 5 minutes, the ratio seems to increase, suggesting the assumption that the variability of the pulse waveform is higher during the cooling down phase than during the guided breathing.

6.3. Limitations

Finally, a few limitations are worth mentioning. The first issue of the developed algorithm concerns the signal preprocessing. While sections containing outliers are denoted quite accurately, the segments, which are added to compensate the missing pieces, are not checked for outliers again. As a consequence, added signal segments might distort the generated attractor and might lead to a wrong calculation of its measurements.

Furthermore, image processing tools play an import role in the extraction of attractor features, e.g. the extraction of the angle of rotation, which, however, might lack in accuracy and thus lead to a high fluctuation depending on the given data set. Stability of the feature extraction process is crucial for ensuring meaningful and comparable results. Therefore, further improvements of the image processing technique would be of advantage.

The implemented method categorizes the attractor into two different shapes. However, some pulse waveform features, like a high dicrotic wave amplitude, lead to attractors with overlapping sides, which cannot be quantified appropriately. Thus, attractors with different contours should also be taken into account.

Although the data used in this thesis was gathered in a comfortable sitting position, some metrological effects, such as varying pressure on the recording device, have negative impact on the generation and quantification of the attractors. It is uncertain, how strong these metrological discrepancies influence the results of the breathing exercise. Moreover, all subjects enrolled in this study suffer from essential hypertension. In order to compare and evaluate the effect of guided breathing, a control group of healthy individuals would be of advantage. Another issue of the guided breathing study is, that pulse waveform data of the subjects were recorded only for 5 minutes past the end of the guided exercise. However, a longer recording period after guidance might reveal further effects of slow breathing on the cardiovascular system.

7. Conclusion and Outlook

The aim of this thesis was to develop an algorithm for automatic quantification of arterial pulse waves and their morphology. For that purpose, an existing attractor reconstruction method was used and extended by measuring the generated attractors. The developed feature extraction technique and its implementation were thoroughly described. The most promising approach turned out to be a combination of image processing together with the usage of the 100×100 density matrix. Although a visual examination of the quantified attractors revealed high accuracy in most cases, some attractors, especially if a lot of outliers occurred or if the recording suffered from metrological discrepancies, were quantified incorrectly. Furthermore, the developed method can only distinguish between triangular attractors or attractors with bent sides and is not able to properly detect attractors with overlapping arms. Thus, further improvements of the feature extraction technique that guarantee a more stable outcome and can classify more attractor shapes would be of advantage.

In addition, the method was only used to analyse a limited set of pulse wave data acquired through photoplethysmography (PPG) at the fingertip. Therefore, it would be interesting to apply the developed algorithm to pulse wave signals recorded with an occlusive cuff, electro-cardiogram (ECG) signals or other almost periodic signals as well. In case attractors generated from those signals display different features than attractors generated from PPG signals, the feature extraction technique would need to be adapted accordingly.

Apart from rapid feature recognition, it is also important to link extracted attractor features to pulse waveform features. In this thesis, correlations already established in [5] and [29] (see table 2.1) were confirmed. Additionally, it was discovered that shape and orientation of the attractor arms mostly depend on the curvature of the pulse waves' downstroke and on the ratio of the crest time to the time delay τ. It was shown that pulse waves with a simple downstroke, i.e. hardly any curvature changes, and $\frac{\text{crest time}}{\tau} = 1$ or close to 1 result in triangular attractors, whereas signals with $\frac{\text{crest time}}{\tau} < 1$ generate bent attractors. Signals with more curvature changes, on the other hand, were not easy to interpret and provided a variety of different attractors. However, it can be assumed that the position of the dicrotic notch and the dicrotic wave amplitude have an impact on the attractors' shape and orientation. In the future, studies should further investigate these correlations because they might provide valuable insights into patients' cardiovascular health status and might enhance clinical decision making.

Applied to pulse wave data of 30 subjects suffering from hypertension, the feature extraction technique revealed a significant decline in the average height of the attractors during the breathing exercise. Future research should focus on the correlation between decreasing pulse pressure

and blood pressure values which were not recorded during the device-guided breathing study. Moreover, further studies should include a control group of healthy individuals to compare and evaluate the effect of guided breathing. Finally, a longer recording period after the exercise might reveal additional effects of deep breathing on the cardiovascular system and should therefore be considered in the future.

Lastly, another interesting approach would be the application of machine learning methods to automate the identification of attractor features and, consequently, distinguish between different cardiovascular phenotypes [29].

A. Appendix

A.1. Table and Plots

This section contains the remaining results of the feature extraction method applied to the given data set which were not presented in chapter 5. Table A.1 contains the absolute values of the width and the ratios of width/height of each attractor arm, where the indices 0, 120 and 240 denote the lower, the left and the right attractor arm, respectively. The evolution of the width of each attractor arm is depicted in figure A.1 and the corresponding boxplots are shown in A.2–A.4. Figure A.5 shows the evolution of the ratios width/height of the three attractor sides and the figures A.6–A.8 illustrate the respective boxplots.

Parameter	Baseline	End of guidance	End of cooling	Friedman	p-value 1-2	p-value 2-3	p-value 1-3	Unit
wd_0	7.09 (3.13)	6.08 (3.43)	6.26 (3.91)	0.013	0.034	1.000	0.026	AU
wd_{120}	7.92 (3.13)	6.41 (3.45)	6.92 (3.42)	0.034	0.062	1.000	0.088	AU
wd_{240}	8.71 (4.14)	6.56 (3.72)	7.41 (4.83)	0.0045	0.003	0.20	0.45	AU
$(\frac{wd}{h})_0$	0.16 (0.06)	0.16 (0.07)	0.17 (0.07)	0.39	-	-	-	AU
$(\frac{wd}{h})_{120}$	0.18 (0.06)	0.17 (0.07)	0.20 (0.06)	0.10	-	-	-	AU
$(\frac{wd}{h})_{240}$	0.19 (0.07)	0.16 (0.06)	0.20 (0.08)	0.003	0.26	0.002	0.26	AU

Table A.1.: Average of extracted features across the given data sets at baseline, at the end of the guided breathing and after the cooling phase. The data is expressed as mean (standard deviation). The column Friedman represents the p-value of the Friedman-Test, whereas the numbered corrected p-value columns contain the results of the post-hoc test, where the numbers indicates which time frames were compared.
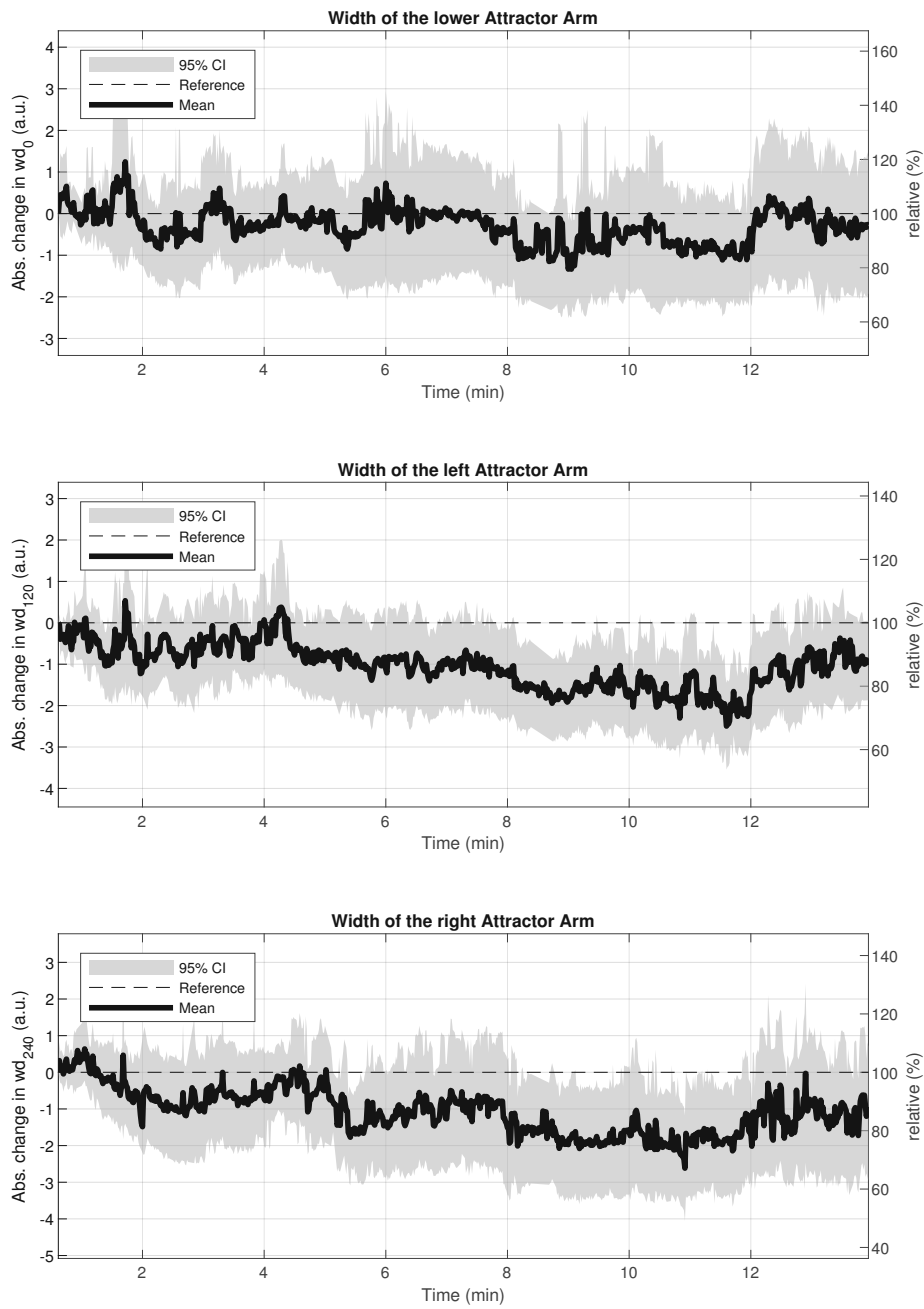
Figure A.1.: Evolution of the widths of the three attractor sides wd_0, wd_{120} and wd_{240}.
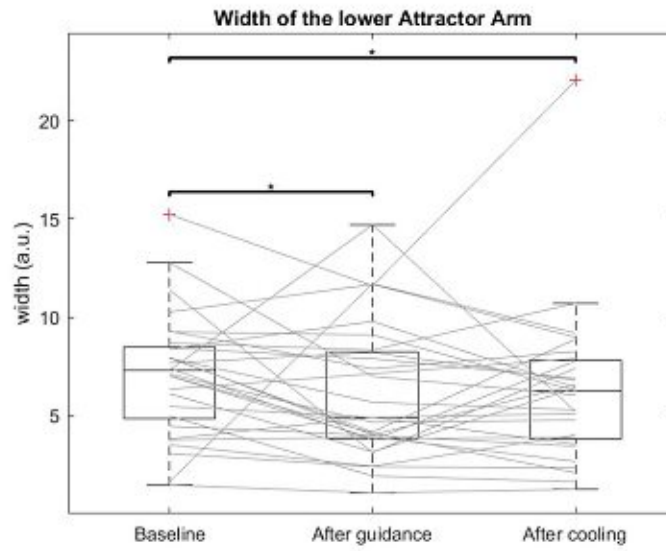
Figure A.2.: Boxplot of the width of the lower attractor arm. The stars indicate the level of significance α, where a single star means $p \leq 0.05$.
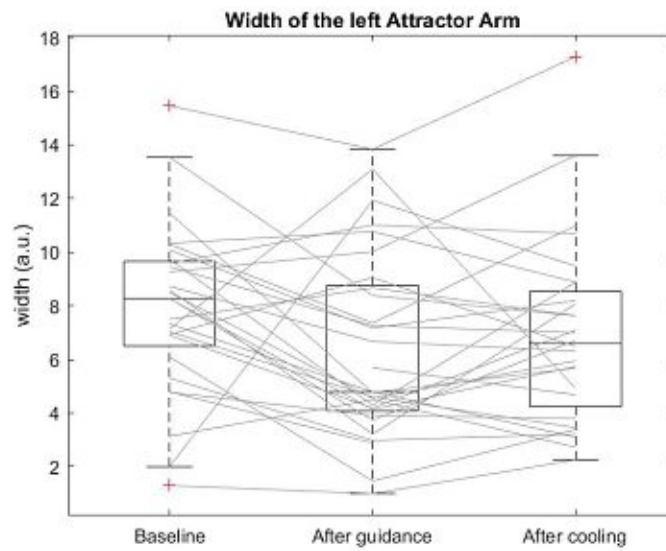

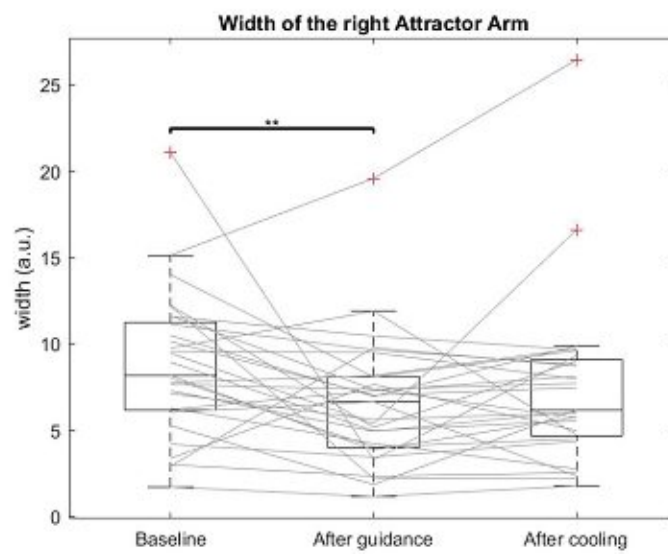Figure A.3.: Boxplot of the width of the left attractor arm.

Figure A.4.: Boxplot of the width of the right attractor arm. The stars indicate the level of significance α, where two stars mean $p \leq 0.01$.
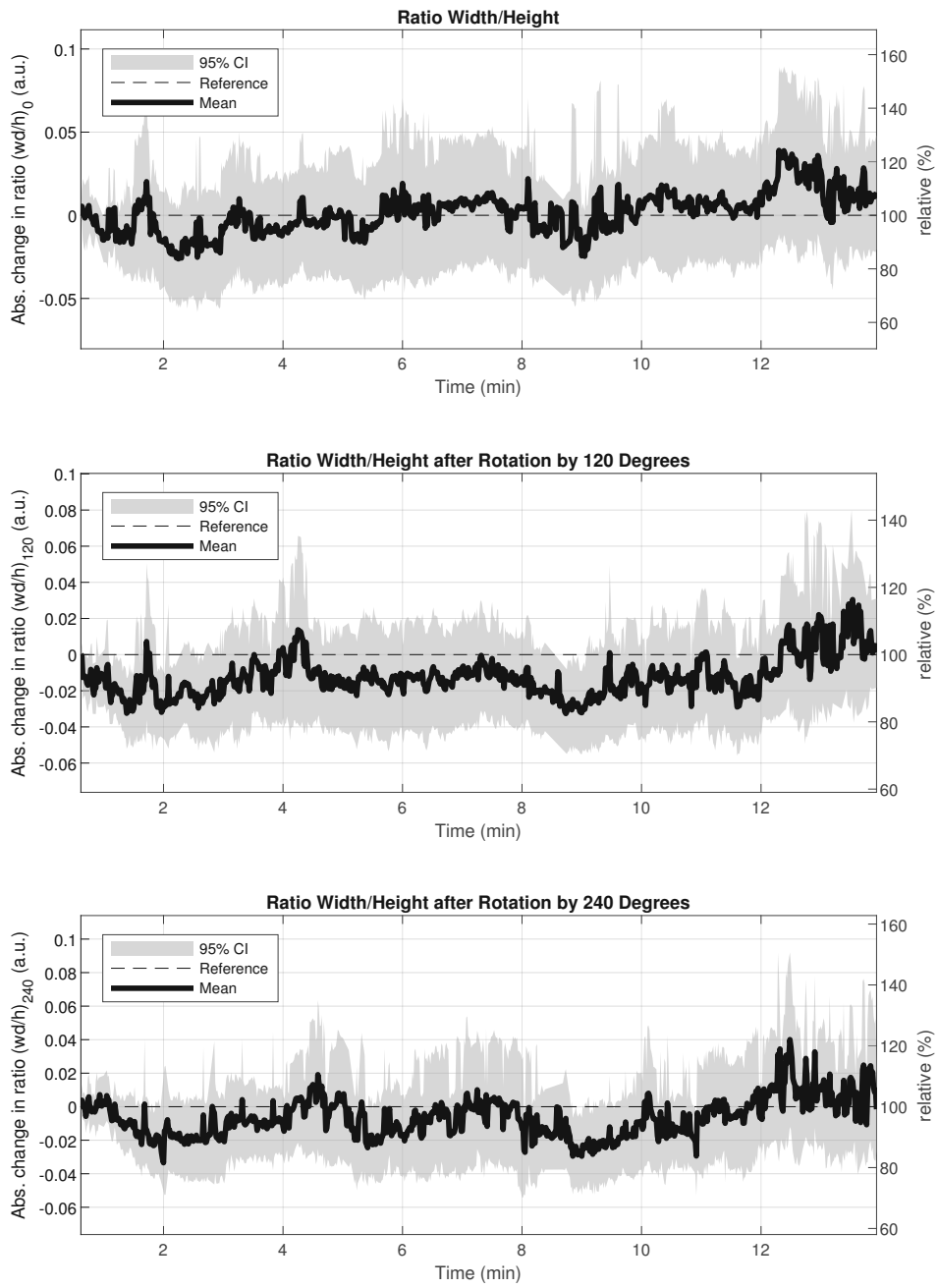
Figure A.5.: Evolution of the ratio $\left(\frac{wd}{h}\right)_0$ and the ratios $\left(\frac{wd}{h}\right)_{120}$, $\left(\frac{wd}{h}\right)_{240}$ after rotating the attractor by 120 and 240 degrees, respectively.
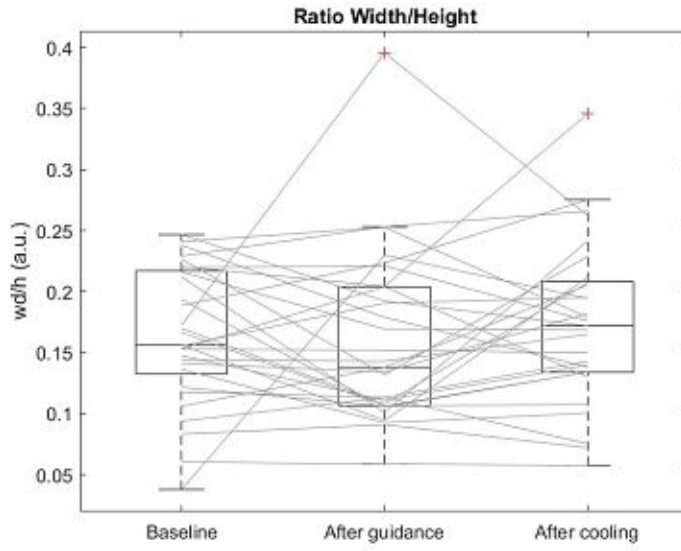
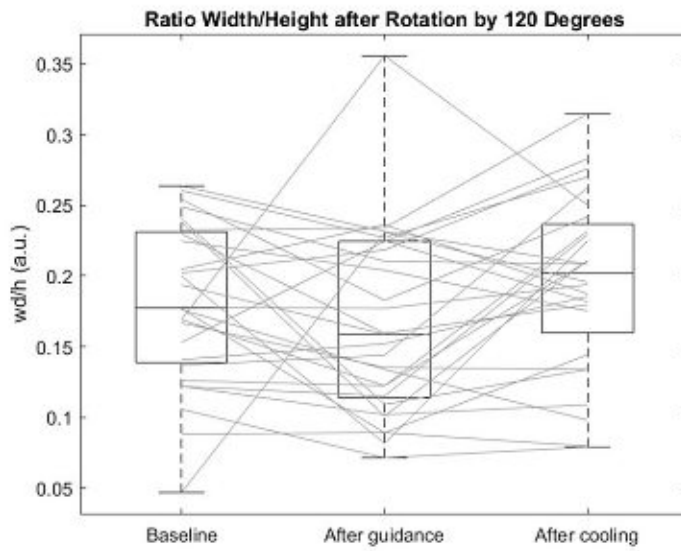Figure A.6.: Boxplot of the ratio $\left(\frac{wd}{h}\right)_0$.

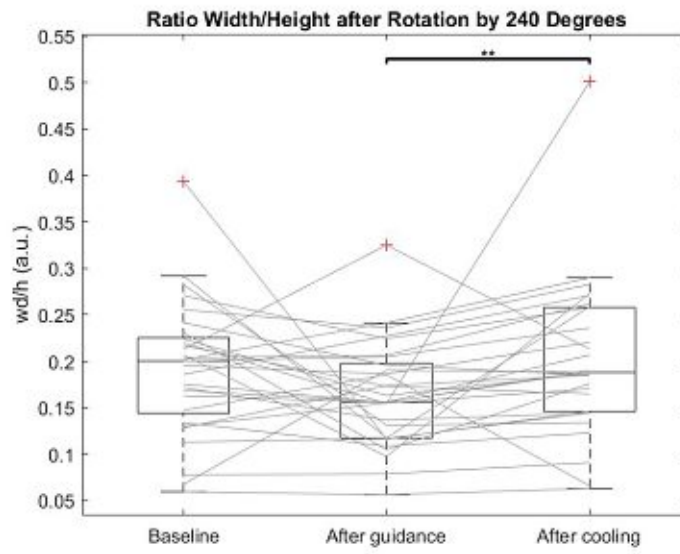Figure A.7.: Boxplot of the ratio $\left(\frac{wd}{h}\right)_{120}$.

Figure A.8.: Boxplot of the ratio $(\frac{wd}{h})_{240}$. The stars indicate the level of significance, where two stars mean $p \leq 0.01$.

Bibliography

[1] AKL T.J. ET AL., 2014: *Quantifying tissue mechanical properties using photoplethysmography.* Biomed Opt Express, 5(7):2362–2375.

[2] ALASTRUEY J., HUNT A.A. AND WEINBERG P.D., 2014: *Novel wave intensity analysis of arterial pulse wave propagation accounting for peripheral reflections.* International journal for numerical methods in biomedical engineering, 30(2):249-279.

[3] ALLEN J., OATES C.P., LEES T.A., MURRAY A., 2005:*Photoplethysmography detection of lower limb peripheral arterial occlusive disease: a comparison of pulse timing, amplitude and shape characteristics.* Physiol Meas. 26(5):811-821.

[4] ALTY S.R. , ANGARITA-JAIMES N., MILLASSEAU S.C. AND CHOWIENCZYK P.J., 2007: *Predicting Arterial Stiffness From the Digital Volume Pulse Waveform.* IEEE Transactions on Biomedical Engineering, 54(12):2268-2275.

[5] ASTON P., CHRISTIE M., HUANG Y. AND NANDI M., 2018: *Beyond HRV: attractor reconstruction using the entire cardiovascular waveform data for novel feature extraction.* Physiol.Meas. 39(2):024001.

[6] BACHLER M., SEHNERT W., MIKISEK I., WASSERTHEURER S. AND MENGDEN T., 2020: *Non-invasive quantification of the effect of device-guided slow breathing with direct feedback to the patient to reduce blood pressure.* Physiol. Meas. in press https://doi.org/10.1088/1361-6579/abb320.

[7] BROOK R.D. ET AL., 2013: *Beyond medications and diet: alternative approaches to lowering blood pressure: a scientific statement from the American heart association.* Hypertension, 61(6):1360-1383.

[8] BUBY C., ELFNER L.F., MAY J.G., 1990: *Relaxation pretraining, pulse wave velocity and thermal biofeedback in the treatment of essential hypertension.* International Journal of Psychophysiology, 9(3):225-230.

[9] CHACKO N. J. ET AL., 2005: *Slow breathing improves arterial baroreflex sensitivity and decreases blood pressure in essential hypertension.* Hypertension, 46(4):714-718.

[10] ELLIOTT W.J., IZZO J.L. JR, 2006: *Device-guided breathing to lower blood pressure: case report and clinical overview.* MedGenMed : Medscape general medicine 8(3):23.

[11] ELSALAMONY H.A., 2015: *Detecting distorted and benign blood cells using the Hough transform based on neural networks and decision trees.* Emerging Trends in Image Processing, Computer Vision and Pattern Recognition, Morgan Kaufmann, pp 457-473.

[12] FAN Z., ZHANG G. AND LIAO S., 2011: *Pulse Wave Analysis*, In: Gaetano Gargiulo (Eds.), Advanced Biomedical Engineering, pp 21-40.

[13] FEDOTOV A.A. AND AKULOVA A.S.: *Adaptive filter for eliminating baseline wander of pulse wave signals* World Congress on Medical Physics and Biomedical Engineering, June 7-12, 2015, Toronto, Canada, pp. 1018-1021.

[14] FU T.H., LIU S.H., TANG K.T., 2008: *Heart Rate Extraction from Photoplethysmogram Waveform Using Wavelet Multi-resolution Analysis.* Journal of Medical and Biological Engineering, 28:229-232.

[15] FUCHS F.D., WHELTON P.K, 2020: *High Blood Pressure and Cardiovascular Disease.* Hypertension, 75(2):285–292.

[16] GUYTON A.C. AND HALL J.E. , 2006: *Textbook of medical physiology.* 11th edition. Elsevier Saunders, Philadelphia.

[17] HAGMAIR S., 2015: *Determination and Evaluation of Heart Rate Variability Parameters with Focus on Nonlinear Methods.* Master's thesis, Technischen Universität Wien.

[18] IMANAGA I., HARA H., KOYANAGI S., TANAKA K., 1998: *Correlation between wave components of the second derivative of plethysmogram and arterial distensibility.* Jpn Heart J, 39:775-784.

[19] M.J. IRVINE, D.W. JOHNSTON, D.A. JENNER, AND G.V. MARIE, 1986: *Relaxation and stress management in the treatment of essential hypertension.* Journal of Psychosomatic Research, 30(4):437-450.

[20] M. GABRIEL KHAN, 2006: *Blood Pressure.* Encyclopedia of Heart Diseases, Academic Press, pp 175-181.

[21] LAURENT S., COCKCROFT J., VAN BORTEL L., BOUTOUYRIE P., GIANNATTASIO C., HAYOZ D., PANNIER B., VLACHOPOULOS C., WILKINSON I., STRUIJKER-BOUDIER H., 2006: *Expert consensus document on arterial stiffness: methodological issues and clinical applications.* Eur. Heart J., 27(21):2588-605.

[22] LÓPEZ-SILVA S. ET AL., 2012: *Heuristic algorithm for photoplethysmographic heart rate tracking during maximal exercise test.* Journal of Medical and Biological Engineering. 32:181-188.

[23] MathWorks, 2020: *Image Processing Toolbox User's Guide (R2020a)*. Retrieved from `https://de.mathworks.com/help/pdf_doc/images/images_ug.pdf`,[visited on 06/15/2020].

[24] Millasseau S., Kelly R., Ritter J., Chowienczyk P., 2002: *Determination of age-related increases in large artery stiffness by digital pulse contour analysis*. Clinical Science, 103:371-377.

[25] On the Analysis of Fingertip Photoplethysmogram Signals: *Mohamed E., 2012*. Current Cardiology Reviews, 8(1):14-25.

[26] Moxham I.M., 2003: *Understanding Arterial Pressure Waveforms*. Southern African Journal of Anaesthesia and Analgesia, 9(1):40-42.

[27] Murray W.B. and Foster P.A., 1996:*The peripheral pulse wave: Information overlooked*. Journal of Clinical Monitoring, 12:365-377.

[28] Nirmalan M. and Dark P., 2014: *Broader applications of arterial pressure wave form analysis*. Contin. Educ. Anaesthesia Crit. Care Pain, 14:285–290.

[29] Nandi M., Venton J. and Aston P., 2018: *A novel method to quantify arterial pulse waveform morphology: attractor reconstruction for physiologists and clinicians*. Physiol.Meas., 39(10):104008.

[30] Nichols W.W., Denardo S.J., Wilkinson I.B., McEniery C.M., Cockcroft J., O'Rourke M.F., 2008: *Effects of arterial stiffness, pulse wave velocity, and wave reflections on the central aortic pressure waveform*. J Clin Hypertens, 10(4):295-303.

[31] Nichols W.W.,O'Rourke M.F., Vlachopoulos C., Hoeks A.P., Reneman R.S., 2011: *McDonald's Blood Flow in Arteries Theoretical, Experimental and Clinical Principles*. 6th edition. Hodder Arnold, London, pp. 195-223.

[32] Pape HC., Kurtz A. and Silbernagel S., 2019: *Physiologie*. 9. Auflage. Georg Thieme Verlag, Stuttgart.

[33] Charlton P.H. et al., 2019: *Pulse Wave Database (PWDB): A database of arterial pulse waves representative of healthy adults*. Retrieved from `https://peterhcharlton.github.io/pwdb/pwdb.html`,[visited on 10/15/2020].

[34] Paranjape R.B., 2009: *Chapter 1 - fundamental enhancement techniques*. I.N. Bankman (Ed.), Handbook of Medical Image Processing and Analysis (2nd), Academic Press, Burlington, MA, USA, pp 3-18.

[35] Rau H., Bührer M., Weitkunat R., 2003: *Biofeedback of R-Wave-to-Pulse Interval Normalizes Blood Pressure*. Applied Psychophysiology and Biofeedback 28(1):37–46.

[36] SHARMA N., 2012: *Linear Hough Transform Using Python.* Retrieved from https://nabinsharma.wordpress.com/2012/12/26/linear-hough-transform-using-python/,[visited on 06/24/2020].

[37] TAKAZAWA K. FM., KIYOSHI Y., SAKAI T., KOBAYASHI T., MAEDA K., YAMASHITA Y., HASE M., IBUKIYAMA C., 1993: *Clinical usefulness of the second derivative of a plethysmogram (acceralation plethysmogram).* Cardiology, 23:207-217.

[38] TAKAZAWA K.TN., FUJITA M., MATSUOKA O., SAIKI T., AIKAWA M., TAMURA S., IBUKIYAMA C., 1998: *Assessment of vasocative agents and vascular aging by the second derivative of photoplethysmogram waveform.* Hypertension, 32:365-370.

[39] TAKENS F., 1981: *Detecting strange attractors in turbulence.* In: Rand D., Young LS. (eds) Dynamical Systems and Turbulence, Warwick 1980. Springer, Berlin, Heidelberg, vol 898, pp 366-381.

[40] TANAKA H., 2017: *Various Indices of Arterial Stiffness: Are They Closely Related or Distinctly Different?.* Pulse, 5:1-6.

[41] TASK FORCE OF THE ESC AND NASPE, 1996: *Guidelines Heart rate variability: standards of measurement, physiological interpretation, and clinical use.* European Heart Journal, 17:354–381.

[42] TIMMIS A. ET AL., 2020: *European Society of Cardiology: Cardiovascular Disease Statistics 2019.* European Heart Journal, 41(1):12-85.

[43] WEBER T., EBER B. ET AL., 2008: *Pulswellengeschwindigkeit zentraler Blutdruck und Augmentationsindex - "neue" Parameter zur Beschreibung eines Endorganschadens der arteriellen Strombahn bei Hypertonie. Pathophysiologie, Methodik prognostische Bedeutung Empfehlungen.* Austrian Journal of Hypertension, 12(1):7-13.

[44] WEBER T. AND SEGERS P., 2015: *Changes in Central Hemodynamics, Wave Reflection, and Heart–Vessel Coupling with Normal and Accelerated Aging.* Early Vascular Aging (EVA), pp. 83-95.

[45] WESTERHOF N., STERGIOPULOS N, NOBLE M., 2005: *Snapshots of Hemodynamics: An Aid for Clinical Research and Graduate Education.* Springer, pp. 105-112.

[46] XU L., MENG M., QI X., WANG K., 2010: *Morphology Variability Analysis of Wrist Pulse Waveform for Assessment of Arteriosclerosis Status.* Journal of medical systems. 34:331-9.